Appendix A

Three-Dimensional Hydrodynamic Modeling for the Scour Hole Initial Options Technical Memorandum

THREE-DIMENSIONAL HYDRODYNAMIC MODELING FOR THE SCOUR HOLE INITIAL OPTIONS TECHNICAL MEMORANDUM

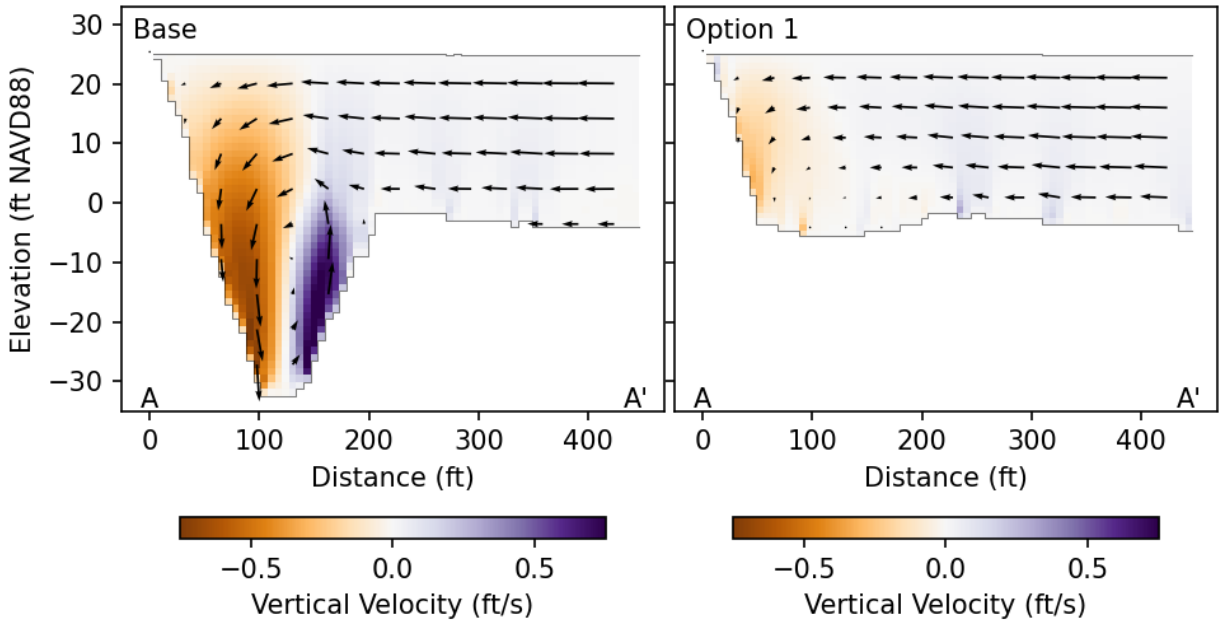

April 2023

Prepared For:
U.S. Department of the Interior
Bureau of Reclamation
California Great Basin Region
Sacramento, CA
Contact:

Prepared By:

Resource Management Associates
1756 Picasso Avenue, Suite G
Davis, CA 95618
Contact:
Edward Gross, PhD
ed@rmanet.com
(530) 231-5323

TABLE OF CONTENTS

LIST OF FIGURES

LIST OF TABLES

INTRODUCTION

This appendix documents the three-dimensional hydrodynamic modeling performed for the Initial Options Assessment. The Initial Options included modifications to the alignment (planform) and bathymetry of channels in a portion of the study region. This effort included application of two different models to different aspects of Initial Options evaluation. The depth-averaged RMA2 Delta model was applied for an initial assessment of the effect of each option on water level in the study area during a 100-year flood event. Calibration and application of the depth-averaged model are described in a separate document. The three-dimensional SUNTANS model was applied to a single Initial Option to assess changes in local hydrodynamics and scour potential.

These two models served different purposes in the Initial Options Assessment. The focus of the depth-averaged RMA2 Delta model applications for the Initial Options Assessment was to evaluate effects on water levels. These changes influenced large scale flow patterns such as the net (tidally-averaged) flow into Old River relative to flow in the San Joaquin River ('flow split').

In contrast, the three-dimensional model was applied to study hydrodynamic effects of Initial Options at a local scale in the vicinity of the project. These effects included changes to bed shear stress, vertical velocity, and secondary circulation and may influence scour potential and predation risk. A three-dimensional model was required because the hydrodynamics near the scour hole are complex due to the sharp curvature of the bend and steep bathymetry. The curvature introduces strong secondary circulation while both the curvature and steep bathymetry contribute to unusually strong vertical velocities. The accurate prediction of vertical velocities required application of a nonhydrostatic hydrodynamic model. We applied the SUNTANS (Fringer et al. 2006) hydrodynamic model in nonhydrostatic mode for this purpose.

Prior to application to alternatives assessment each model was calibrated against hydrodynamic data. This appendix documents the calibration of the three-dimensional model, and its initial application to Option 1 (filling in the scour hole).

THREE-DIMENSIONAL HYDRODYNAMIC MODEL CALIBRATION

The three-dimensional SUNTANS model will be used to evaluate alternatives for the 'Scour Hole' project during and after the Initial Options Assessment phase. Among the potential alternatives, there will likely be modifications to the alignment (planform), the bathymetry, and/or bed materials in a portion of the region. These changes may influence large scale flow patterns such as the net (tidally-averaged) flow into Old River relative to flow in the San Joaquin River ('flow split'). These changes will be evaluated with the depth-averaged Delta-scale model, RMA2. Then the depth-averaged model will provide flow boundary conditions for scenarios of

alternatives to the much higher resolution three-dimensional model that is described here. In order to simulate the effect of management actions, calibration of the three-dimensional model is required.

This document outlines the calibration effort for two periods: a high flow period in 2019 and a lower flow period in 2022. The 2019 hydrodynamic observations were collected as part of a UC Davis study (Holleman et al. 2022), while the 2022 data were collected for this study. 2019 was classified as a wet year in the San Joaquin Valley while 2022 was classified as a critical year. The average flow at the upstream boundary (near Mossdale) on the day of the 2019 survey was 14,800 cfs, and was 890 cfs on the day of the 2022 survey. The average stage at the Head of Old River was 11.3 ft NAVD on the day of the 2019 survey, and was 4.4 ft NAVD on the day of the 2022 survey. For reference, a 10-year flow event is 22,000 cfs at Mossdale (FEMA 2009).

The remainder of this section introduces and provides some background information and context for the three-dimensional model calibration. The following sections detail the modeling framework used to investigate the hydrodynamics of the study region. The model grid, bathymetry and boundary conditions are presented. Model performance metrics are defined which quantify the ability of the hydrodynamic model to reproduce hydrodynamic features, including secondary circulation. The final sections of the calibration documentation present the results of the hydrodynamic model simulations and comparisons to ADCP data and a brief discussion.

OVERVIEW

The model presented here is related to the hydrodynamic model applied by Holleman et al. (2022) and used for particle-tracking simulations in Gross et al. (2021). However, Holleman et al. (2022) only calibrated the model during moderate flow conditions in 2018, classified as a 'below normal' year in the San Joaquin Valley. The goals of the UC Davis project were related to understanding and quantifying Chinook salmon smolt behavior and did not focus on the hydrodynamics of the scour hole. For that reason, the SUNTANS model was run in hydrostatic mode by Holleman et al. (2022).

In contrast the three-dimensional modeling effort for this project is strongly focused on the scour hole. Because of the steepness of the scour hole and the interplay between scour and nonhydrostatic processes, we ran the model in nonhydrostatic mode. We also have extended the model domain substantially, farther upstream and downstream of the scour hole and laterally to the levee crests. The hydrodynamic model grid was regenerated to provide fairly uniform and high resolution over the scour hole.

The calibration utilized velocity transects at a series of cross-sections for each simulation period. These data quantify the lateral and vertical distribution of three-dimensional velocity

vectors (horizontal and vertical velocities) throughout each cross-section. These velocity observations allowed us to evaluate the ability of the model not only to predict depth-averaged currents but also the distribution of streamwise, secondary (laterally directed), and vertical velocities at each point (horizontally and vertically) in the cross section.

THREE-DIMENSIONAL MODEL FORMULATION

The computational framework necessary for hydrodynamic modeling of the study region includes several components: a hydrodynamic model engine, a model grid, model parameters, and boundary conditions.

The SUNTANS model (Fringer et al. 2006) was chosen as the modeling engine for this work. SUNTANS uses the semi-implicit method to numerically solve the 3-D Reynolds-averaged Navier-Stokes equations for conservation of fluid volume and momentum to predict water velocities and water surface elevations:

$$\frac{\partial u}{\partial x} + \frac{\partial v}{\partial y} + \frac{\partial w}{\partial z} = 0 \tag{1}$$

$$\frac{\partial u}{\partial t} + u\,\frac{\partial u}{\partial x} + v\,\frac{\partial u}{\partial y} + w\,\frac{\partial u}{\partial z} - fv = -\frac{\partial p}{\partial x} + \nu_h\left(\frac{\partial^2 u}{\partial x^2} + \frac{\partial^2 u}{\partial y^2}\right) + \frac{\partial}{\partial z}\left(\nu_v\frac{\partial u}{\partial z}\right) \tag{2}$$

$$\frac{\partial v}{\partial t} + u\,\frac{\partial v}{\partial x} + v\,\frac{\partial v}{\partial y} + w\,\frac{\partial v}{\partial z} + fu = -\frac{\partial p}{\partial y} + \nu_h\left(\frac{\partial^2 v}{\partial x^2} + \frac{\partial^2 v}{\partial y^2}\right) + \frac{\partial}{\partial z}\left(\nu_v\frac{\partial v}{\partial z}\right) \tag{3}$$

$$\frac{\partial w}{\partial t} + u\,\frac{\partial w}{\partial x} + v\,\frac{\partial w}{\partial y} + w\,\frac{\partial w}{\partial z} = -\frac{\partial p}{\partial z} + \nu_h\left(\frac{\partial^2 w}{\partial x^2} + \frac{\partial^2 w}{\partial y^2}\right) + \frac{\partial}{\partial z}\left(\nu_v\frac{\partial v}{\partial z}\right) - \frac{\rho}{\rho_0}g \tag{4}$$

where *u*, *v*, and *w* are the velocities in the *x*, *y*, and *z* directions, *t* is time, *f* is the Coriolis frequency, *g* is the acceleration of gravity, p is the normalized pressure defined as the pressure divided by a constant reference density (ρ_0), ν_h is the horizontal eddy viscosity and ν_v is the vertical eddy viscosity.

These equations are subject to the free surface boundary condition:

$$\frac{\partial \eta}{\partial t} + \frac{\partial}{\partial x}\left[\int_{-h}^{\eta} u\,dz\right] + \frac{\partial}{\partial y}\left[\int_{-h}^{\eta} v\,dz\right] = 0 \tag{5}$$

where η is the free surface elevation and *h* is the water depth measured positive downward from a constant vertical datum.

The bottom boundary condition is:

$$\nu^v \frac{\partial u}{\partial z} = \gamma_B u, \qquad \nu^v \frac{\partial v}{\partial z} = \gamma_B v, \qquad \text{at } z = -h \tag{6}$$

where γ_B is the bottom friction coefficient computed as

$$\gamma_B = C_d \sqrt{u^2 + v^2}, \qquad C_d = \kappa^2 \left[\log \frac{\Delta z}{z_0} - 1 + \frac{z_0}{\Delta z} \right]^{-2} \tag{7}$$

where C_d is coefficient of drag, κ is the von Karman constant (0.42), and z_0 is the Nikuradse roughness parameter, specified by the user in the calibration process. Note that the $z_0/\Delta z$ term is often omitted, but can be relevant when the layer spacing is of similar order to roughness scales, a potential concern in the present application where bed material includes riprap.

Key attributes of this numerical method include the use of an unstructured, orthogonal, staggered Arakawa-C grid in the horizontal dimensions, z-layer vertical coordinates, and a semi-implicit finite-difference/finite-volume approach (Fringer et al. 2006). This model resolves the physical processes necessary for modeling three-dimensional nonhydrostatic flow and allows horizontal and vertical wetting and drying of computational cells with water level variation.

The SUNTANS model is Reynolds-averaged, meaning that the equations are averaged over turbulent time scales and apply to mean flow. In order to parameterize the influence of turbulence on the mean flow, a vertical turbulence closure scheme was prescribed using the k-ε version of a Generic Length Scale (GLS) closure (Rodi 1987; Umlauf and Burchard 2003) with stability functions from Canuto (Canuto et al. 2001). No turbulence closure scheme was used in the horizontal and a constant horizontal eddy diffusivity of zero was specified.

MODEL DEVELOPMENT

This section describes the site-specific development of the SUNTANS model used for the scour hole project.

GRID DEVELOPMENT

The model domain extends from Mossdale Landing Community Park, roughly 2 km upstream of the junction of the San Joaquin River and the head of Old River to approximately 200 meters downstream of the junction on both Old River and the San Joaquin River (Figure 1). The lateral extent of the domain is from levee crest to levee crest along its full extent.

An unstructured orthogonal grid was created using 13,195 quadrilaterals and 267 triangles (Figure 2). The resolution is highest over the scour hole with typical edge lengths of 1m. The largest cells are near the upstream and downstream boundaries with edge lengths ranging from 5m to 10m. The quadrilaterals are typically aligned with the primary flow direction.

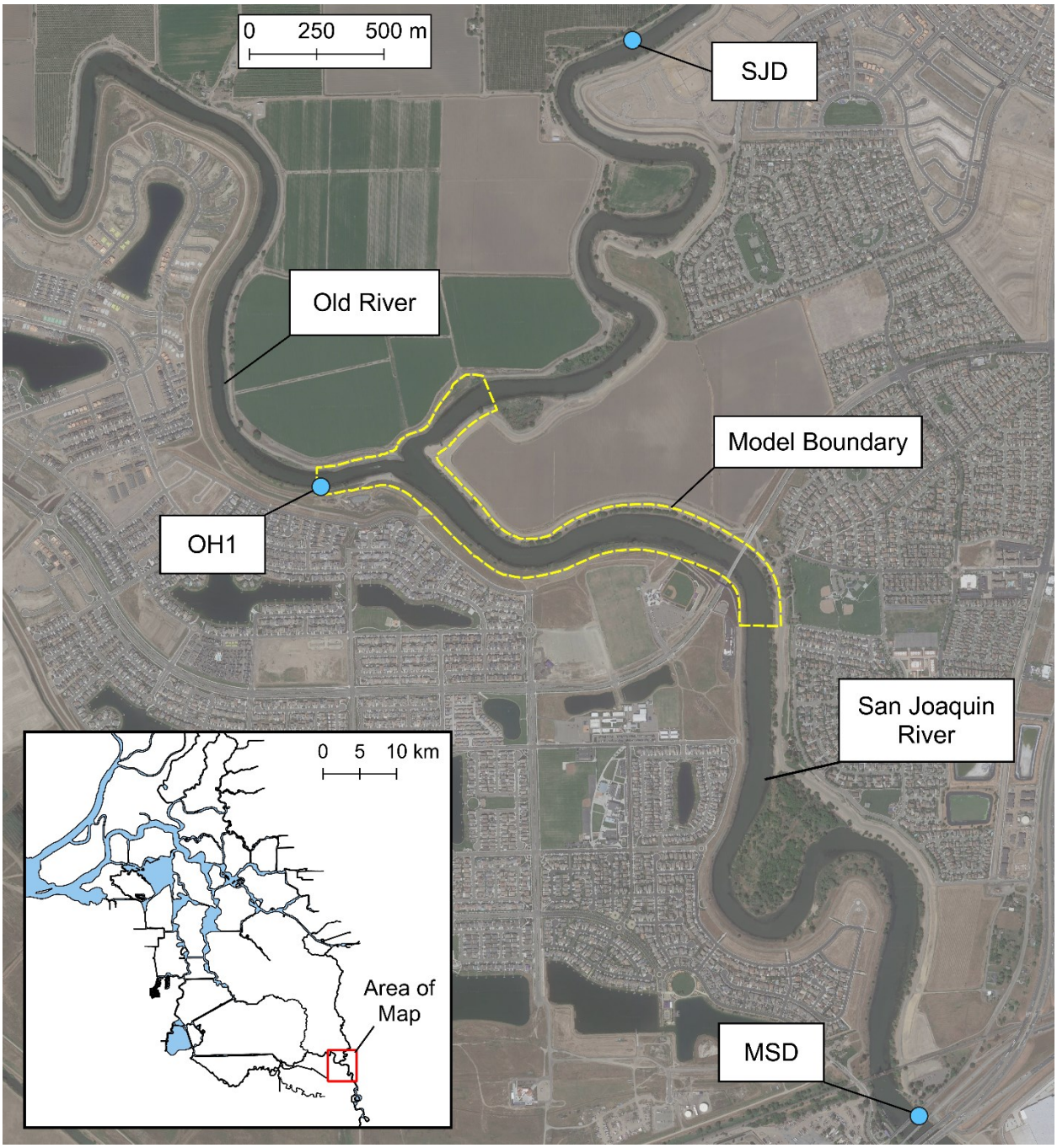

Figure 1 Model domain and surrounding region.

Figure 1 shows the study area along the San Joaquin River and Old River, including model boundary limits and monitoring locations used in the analysis. An inset map identifies the regional location of the model domain within the Sacramento–San Joaquin Delta.

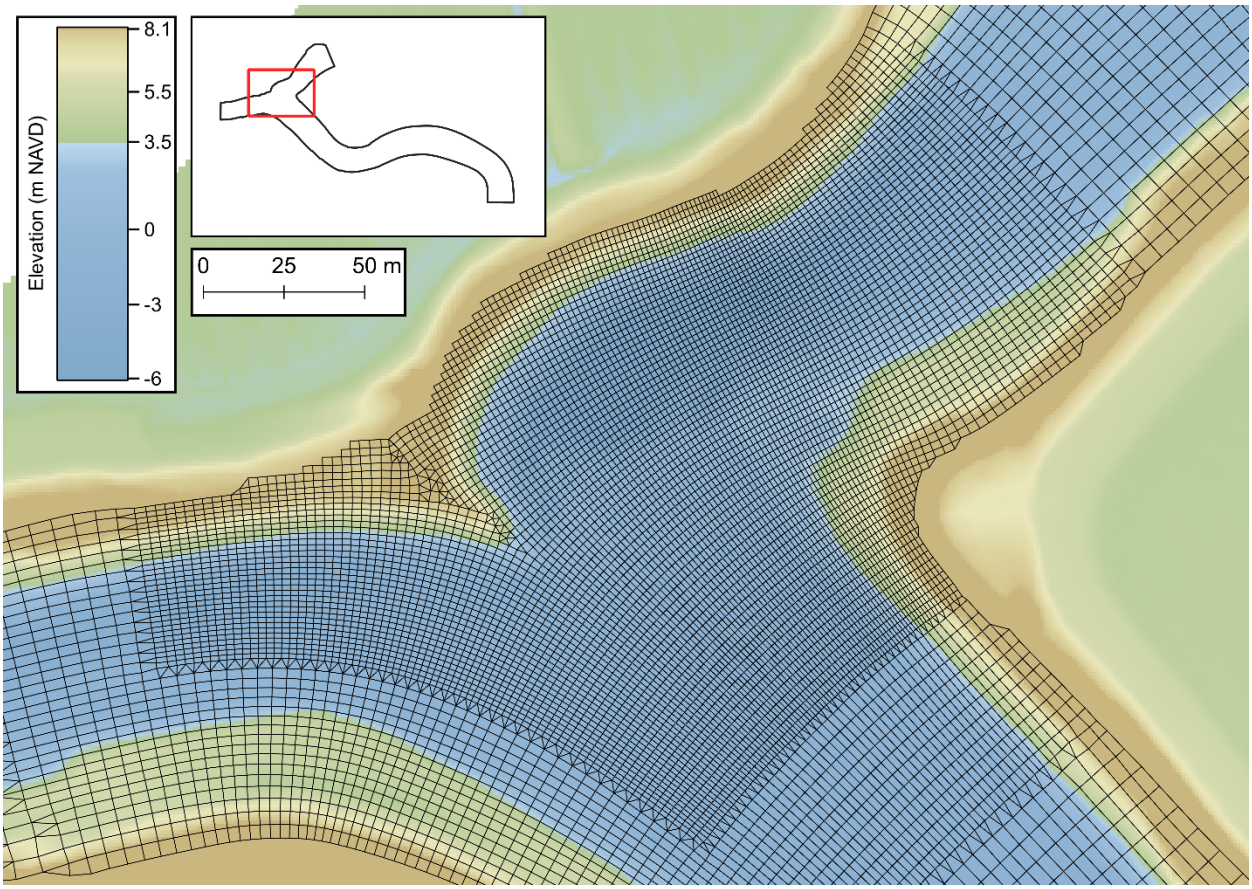

Figure 2 High resolution portion of model grid near the scour hole.

Figure 2 shows a detailed view of the refined model grid in the vicinity of the scour hole, illustrating local bathymetry and increased mesh resolution within this portion of the model domain.

Bed elevations for the model differed between the 2019 and 2022 configurations. For both configurations the larger scale bathymetry was set based on a DWR 2m resolution digital elevation model (DEM) covering a portion of the South Delta (available at the CNRA data modeling website). This DEM is largely based on data collected in 2020 and includes both bathymetry and levee topography. Bathymetry around the scour hole was taken from two additional multibeam datasets from DWR: a March 26, 2019 survey was used for 2019 calibration simulations and a May 13, 2021 survey was used for 2022 calibration simulations. Both fine-scale datasets were gridded at 1ft resolution (as provided by DWR).

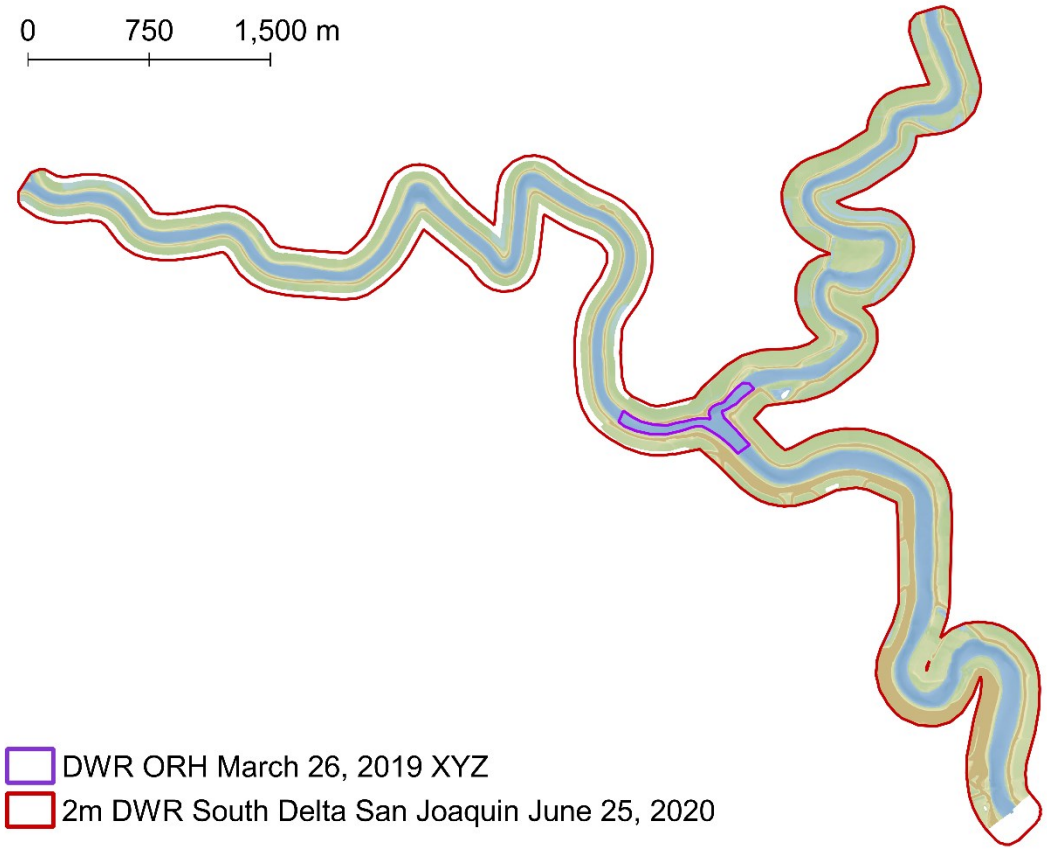

Figure 3 Spatial extent of bathymetry data sources used in defining model bathymetry for the 2019 calibration.

Figure 3 shows the spatial coverage of bathymetry datasets used to define model bathymetry for the 2019 calibration, including the DWR ORH March 26, 2019 dataset and the 2 m DWR South Delta San Joaquin June 25, 2020 dataset.

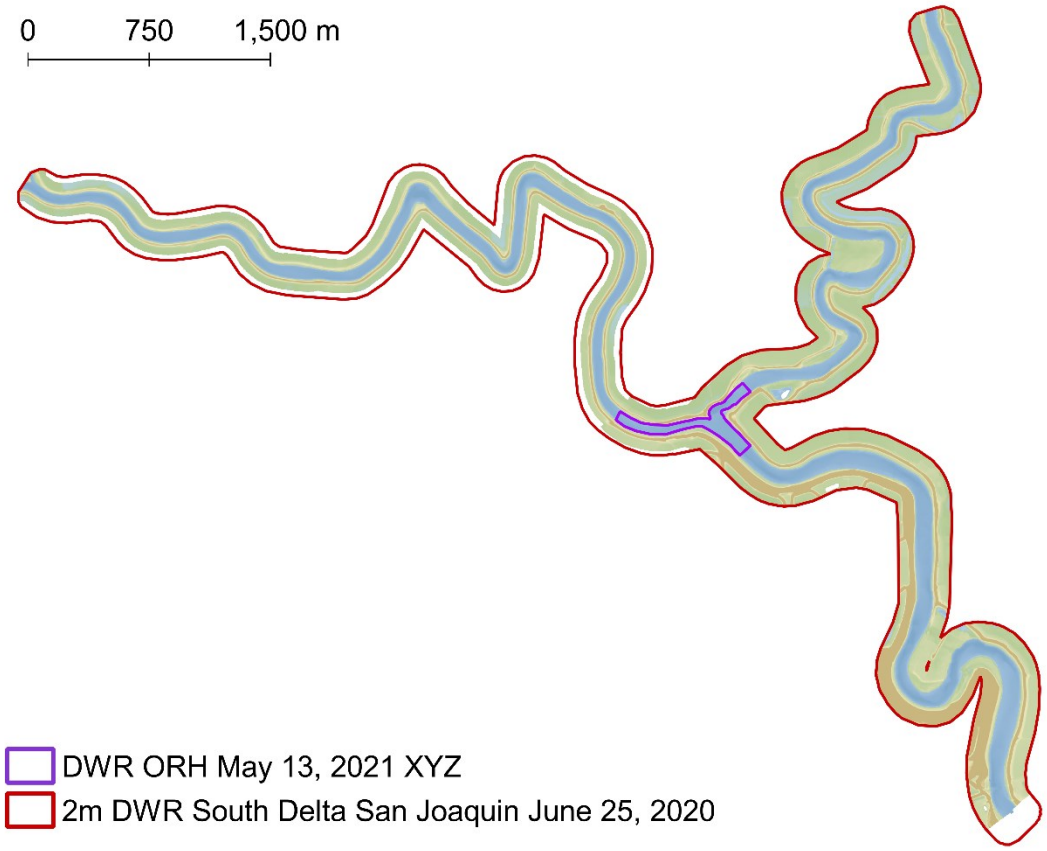

Figure 4 Spatial extent of bathymetry data sources used in defining model bathymetry for the 2022 calibration.

Figure 4 shows the spatial coverage of bathymetry datasets used to define model bathymetry for the 2022 calibration, including the DWR ORH May 13, 2021 dataset and the 2 m DWR South Delta San Joaquin June 25, 2020 dataset.

A total of 50 vertical layers with vertical spacing of 0.319 m were used to resolve the vertical dimension. The resulting grid consisted of 13,462 horizontal cells (water columns). The number of wet water columns and number of active (wet) vertical layers vary through the simulation as stage varies leading to changes in horizontal and vertical extent of inundation and ranges to over 157,000 active prisms.

MODEL BOUNDARY CONDITIONS

Three stations near the junction of the San Joaquin River and Old River (at head) contain flow data at a 15-minute interval. The DWR San Joaquin River at Mossdale station (MSD) is located upstream of the junction, the DWR San Joaquin River above Dos Reis Park (SJD) is located downstream of the junction and the DWR Old River @ Head station (OH1) is located on Old River downstream of the junction (Figure 1). Because there were no significant inflows or outflows in the reaches bounded by these stations, the consistency of net (tidally-averaged)

flow reported at the stations was evaluated by a “flow balance” approach. This analysis suggested that the balance was imperfect, and furthermore differed year-to-year. For this reason, a combination of RMA2 Delta model results and observed data were used to specify boundary conditions for the three-dimensional model. For both calibration periods flow boundary conditions were imposed on the southern (upstream) and northern (downstream) San Joaquin boundaries, and a water level boundary condition was imposed on the Old River boundary (Figure 1).

For 2019, the San Joaquin flow at the downstream boundary was specified using RMA2 Delta model results, accounting for a 30 minute lag observed in the RMA2 calibration for this period. The upstream flow boundary condition was calculated as the sum of measured flow at OH1 and the RMA2-based San Joaquin downstream boundary condition. The Old River water level boundary condition was specified from observed water level at OH1 (boundary flow was not specified on Old River, and water level was not specified on either San Joaquin boundary). A one-hour low pass filter (convolution with a 1-hour Hanning window) was applied to both the observed flow and water level data to remove high frequency oscillations in the observations. Time series of these boundary flows and water level are shown for 2019 in Figure 5.

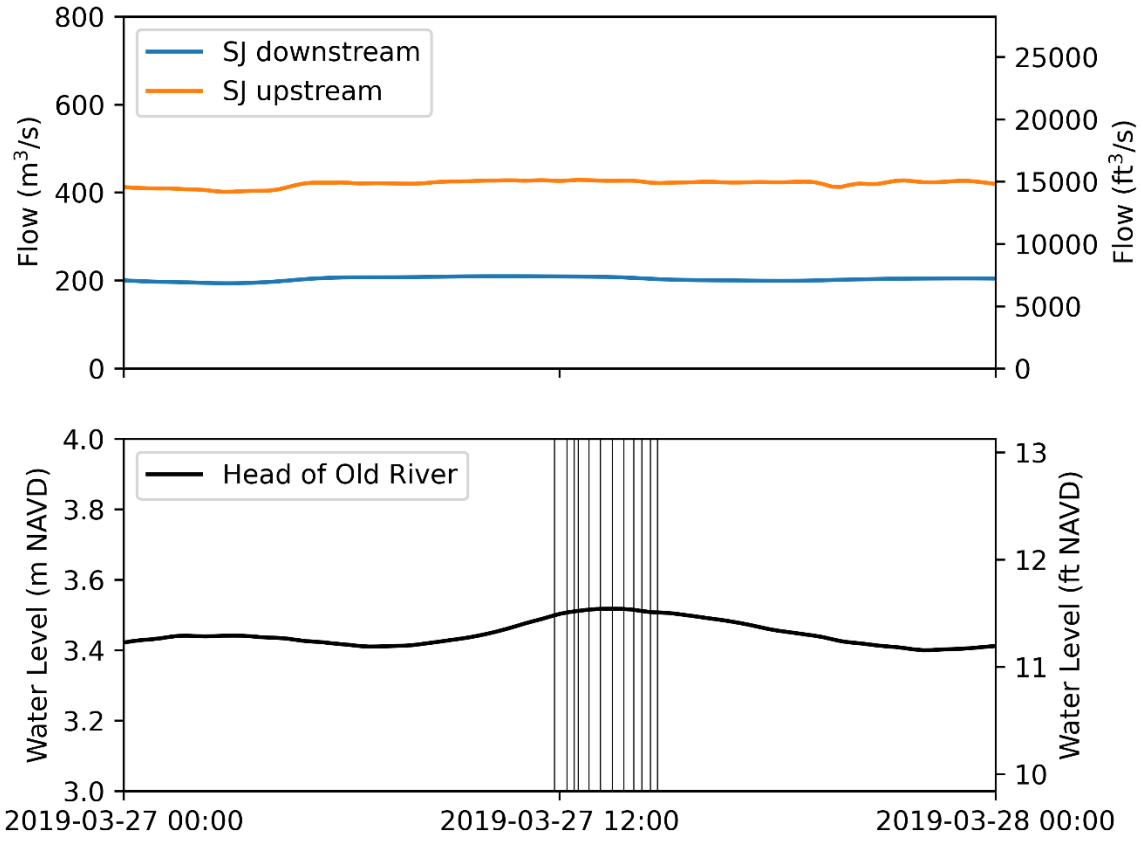

Figure 5 Flow and stage boundary conditions for 2019 hydrodynamic simulation. The vertical lines indicate times of the ADCP transects in 2019.

Figure 5 shows time series of upstream and downstream San Joaquin River flow and water level at the Head of Old River used as boundary conditions for the 2019 hydrodynamic simulation.

Conditions in 2022 had much greater tidal influence and different flow imbalances, requiring an alternative handling of boundary conditions. For 2022 simulations the upstream flow boundary condition was specified from observed flows at MSD, with a 0.5-hour Butterworth lowpass filter and 10 minute phase advance to account for tidal propagation and improve comparisons to observations. Downstream flow was specified from observed flow at SJD, adjusted with a scaling factor of 0.903, phase advance of 208 s, and 0.5 hour lowpass filter. These adjustments were inferred from RMA2 simulations of tidal propagation between the SJD gage and the model boundary. Water level on Old River was specified from water level observations at OH1, with a 0.5-hour Butterworth lowpass filter. Resulting boundary condition data for 2022 are shown in

Figure 6.

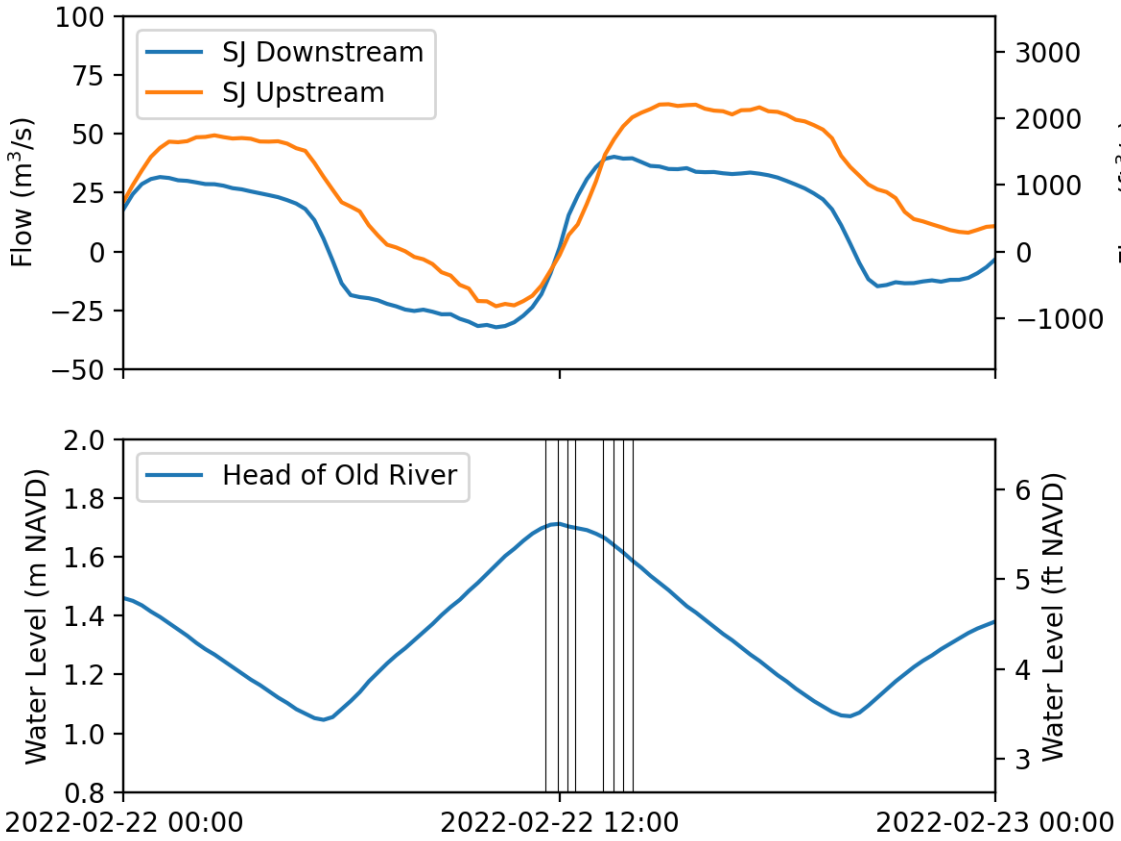

Figure 6 Flow and stage boundary conditions for day of 2022 ADCP transects. The vertical lines indicate times of the ADCP transects for each cross-section in 2022.

Figure 6 shows time series of upstream and downstream San Joaquin River flow and water level at the Head of Old River used as boundary conditions for the day of the 2022 ADCP transects.

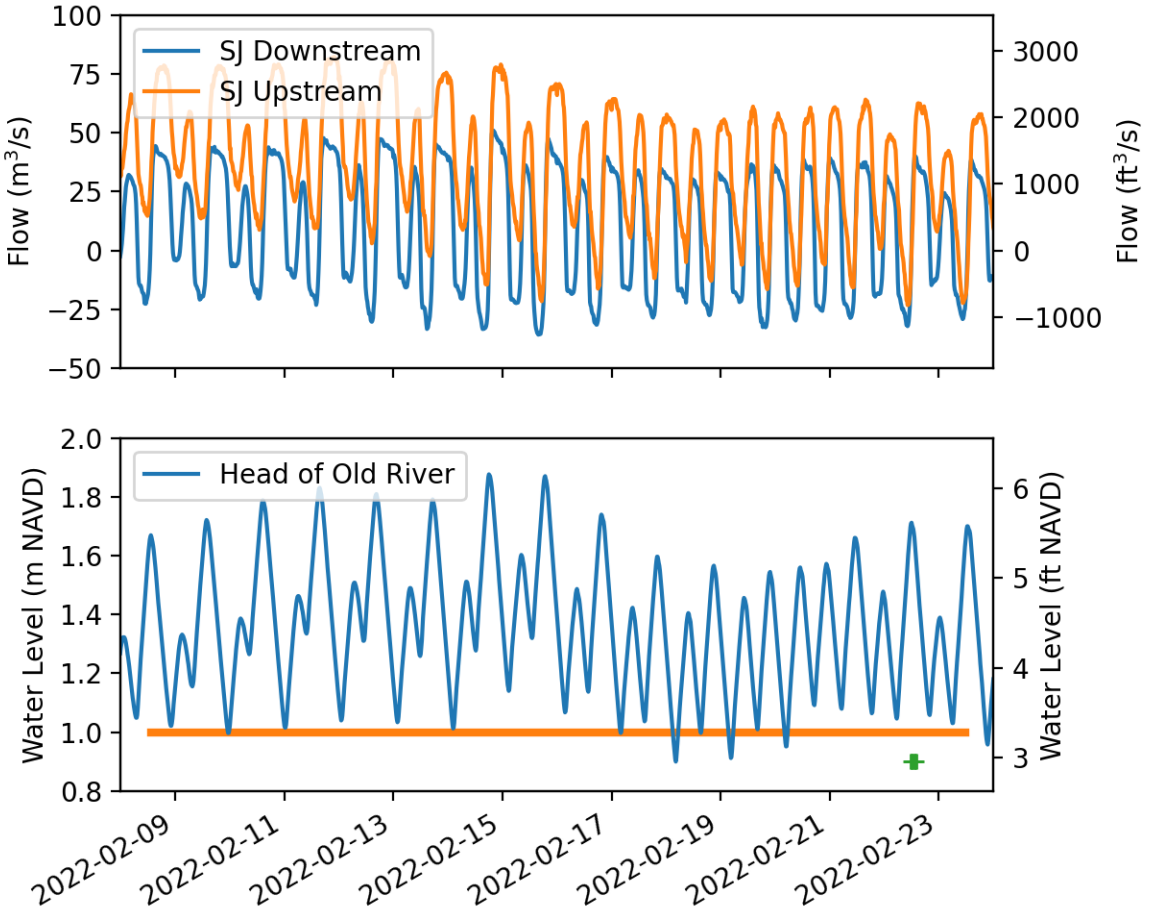

Figure 7 Flow and stage boundary conditions for day of 2022 ADCP mooring (orange line in bottom panel). The green + signs show times of ADCP transect data collection.

Figure 7 shows time series of upstream and downstream San Joaquin River flow and water level at the Head of Old River used as boundary conditions for the period of the 2022 ADCP mooring.

BED ROUGHNESS

The bed roughness height (z_0) was spatially-variable in several discrete zones according to bed type and ranged from 2 mm to 8 mm (Figure 8). Bed types were based on 1 ft resolution multibeam data from a 2017 DWR survey. Regions of riprap, dunes, and smooth substrate were visually extracted from the survey and labeled in a GIS layer. Representative physical roughness was extracted from the different types of regions based on the root-mean-square of the elevation variation at scales smaller than the nominal cell size.

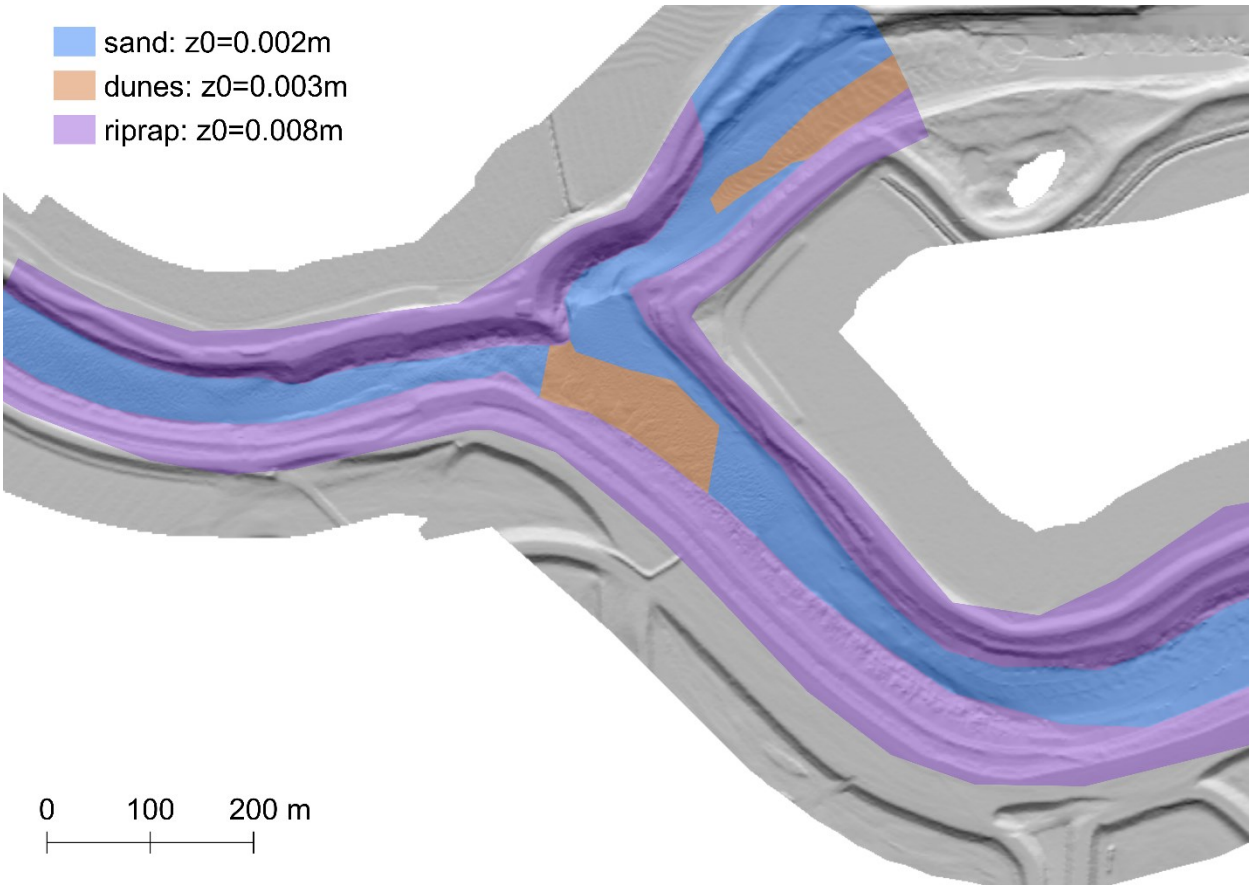

Figure 8 Spatially-variable bed roughness height (z_0) in SUNTANS simulations.

Figure 8 shows the distribution of bed roughness height values (z_o) assigned in the SUNTANS simulations, including areas classified as sand (0.002 m), dunes (0.003 m), and riprap (0.008 m).

CALIBRATION SIMULATIONS

Conditions during a high flow period in 2019 and a lower flow period in 2022 were simulated. The 2019 simulation period was March 26th through late March 27th. The average flow on March 27th was 14,800 cfs (Figure 5), compared with a 10-year return interval flow of 22,000 cfs at Mossdale (FEMA 2009). The 2022 simulation period spanned the 2022 field campaign, including the ADCP transects that were collected on February 22nd. Flow during the ADCP transecting averaged 890 cfs near Mossdale (Figure 6).

In both years, the initial water level was set to a uniform value equal to the observed water level at the Head of Old River station (OH1) at the starting time of the simulation. Initial velocities were zero.

Model calibration was carried out by refining the computational grid, adjusting bed roughness heights (z_0), and adjusting parameters of the treatment of turbulent mixing.

CALIBRATION DATA

The calibration for this study used ADCP data collected by UCD (as part of CDFW-funded grant P1796017) and cbec (as part of this study). The UCD data were collected at 12 cross-section locations (Figure 9). At each of those locations, 6 velocity transects were performed. These individual transects were averaged together and then smoothed spatially. These steps minimized the influence of turbulent velocities and instrument noise. The final processed ADCP data consisted of one processed velocity transect along each cross-section on each survey day. Data collection by cbec followed a similar process, with cross-section locations shown in Figure 10. The 2022 data collection also included an upward-looking ADCP deployed near the bed (Figure 10).

The ADCP observations extend approximately as close to the bank as was accessible. The data did not extend to the surface due to the "blanking distance" associated with ADCP data, which was approximately 0.2 meter (Holleman et al. 2022). Similarly, near-bed velocities were omitted from the boat-mounted ADCP due to sidelobe contamination (approximately the deepest 10% of ADCP bins).

The Rozovskii method (Rozovskii 1957) was used to decompose the horizontal velocity components into primary (streamwise) and secondary velocity. For the purposes of this analysis, we use "secondary" to refer specifically to the horizontal velocity component perpendicular to the streamwise direction and exclusive of vertical velocities which are analyzed separately. The Rozovskii method was applied to the processed ADCP data (i.e., after averaging repeated transects). The angle of rotation is defined as the direction of the depth-integrated discharge vector. In other words, the net (depth-integrated) flow is in the primary direction and the secondary circulation (perpendicular to the primary direction) consists only of exchange flow (no net flow). Because each lateral position (water column) in the cross-section is processed individually the rotation angle used can vary across the cross-section (Bever and MacWilliams 2015) and does not necessarily correspond to the angle associated with the transect data. The Rozovskii method was reported by Bever and MacWilliams (2015) to be more reliable for distinguishing primary and secondary circulation relative to approaches which use the same rotation angle for all water columns in a transect.

Table 1 Average stage at OH1 and flow at the upstream boundary (near Mossdale) during survey days

Date	**Stage NAVD88 (ft)**	**Discharge (ft3 s^{-1})**
March 27, 2019	11.3	14,800
Feb 22, 2022	4.4	890

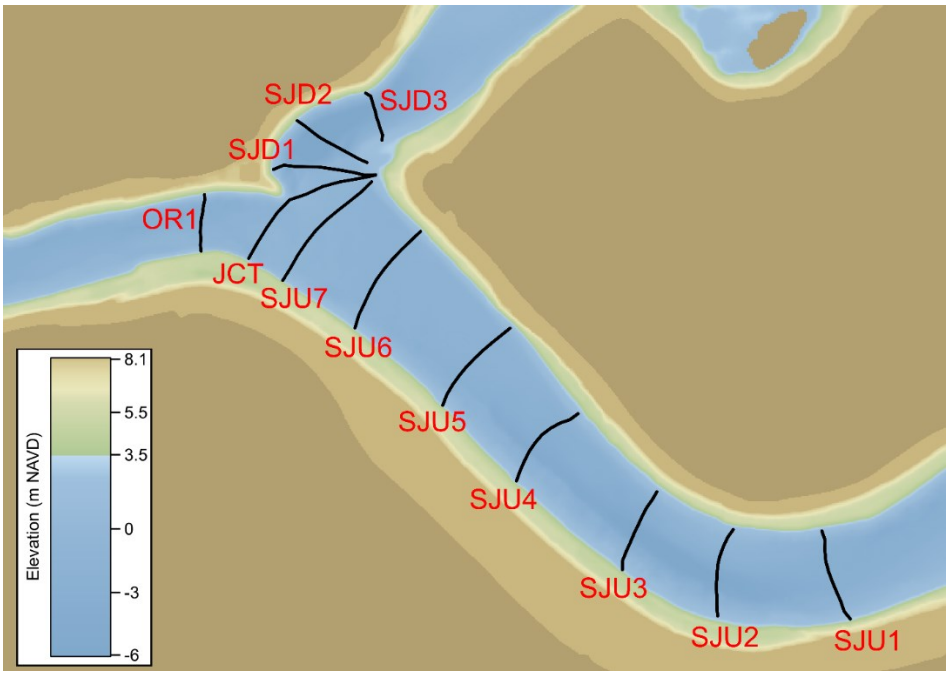

Figure 9 ADCP cross-section locations for the 2019 UCD study.

Figure 9 shows the locations of ADCP cross-sections used in the 2019 UCD study (OR1, JCT, SJD1–SJD3, and SJU1–SJU7) overlaid on an elevation map (m NAVD).

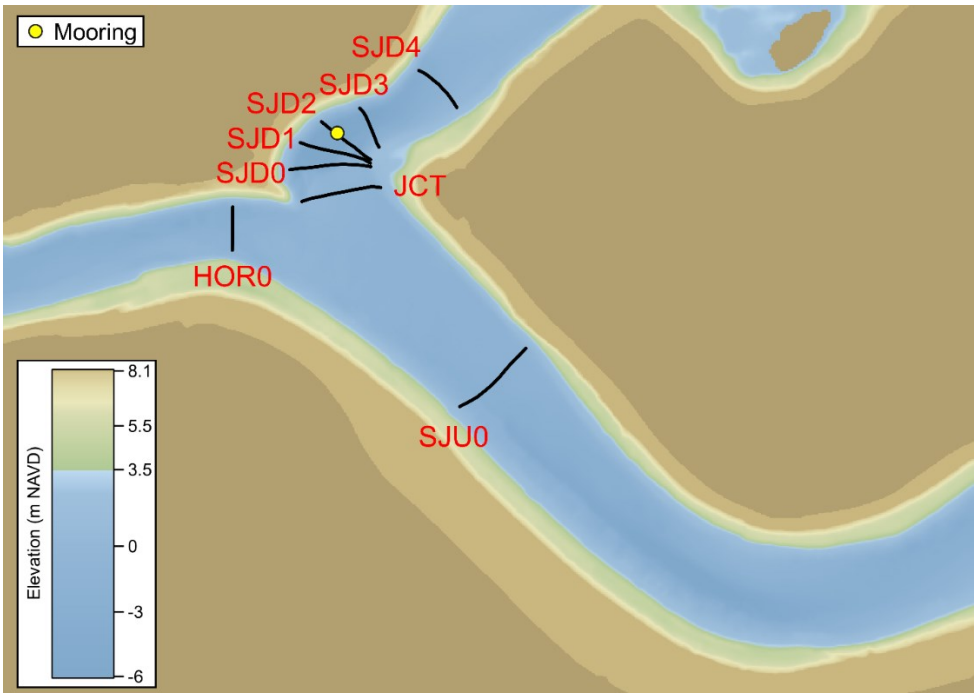

Figure 10 ADCP mooring and cross-section locations for the 2022 cbec study.

Figure 10 shows the locations of the ADCP mooring and cross-sections used in the 2022 cbec study (HOR0, SJD0–SJD4, JCT, and SJU0) overlaid on an elevation map (m NAVD).

MODEL EVALUATION METHODS AND METRICS

The model evaluation included both qualitative visual comparisons and quantitative metrics. Though the predicted velocity extended over the full cross-section, predicted and observed velocity information were compared for matching spatial extents, which was limited by the extent of the observations.

Visual comparisons included comparisons of depth-averaged velocity vectors on each survey day and comparisons of both primary and secondary circulation for each cross-section on each survey day.

Several quantitative metrics for primary and secondary velocity components were used for model evaluation. The predicted and observed strength of secondary circulation was calculated as the depth-averaged absolute value of the horizontal component of secondary velocity. Vertical velocity was also examined in the calibration.

Standard performance metrics utilized include bias and root-mean-square difference (RMSD), also referred to as root-mean-square error (RMSE). We use the term RMSD to emphasize that the ADCP data is also an approximation of the actual velocity and has associated instrument error and other sources of error. The bias is simply the difference between the predicted and observed means

$$bias = \frac{1}{N}\sum_{i=1}^{N} X_{Pi} - \frac{1}{N}\sum_{i=1}^{N} X_{Oi} \tag{8}$$

where X_{Oi} is an observed data point, such as a single primary velocity at a specific x,y,z location and X_{Pi} is the corresponding predicted data point, and *N* is the total number of predictions compared with observations. A positive bias indicates that the model overpredicts the observations on average.

The RMSD is

$$RMSD = \left(\frac{1}{N}\sum_{i=1}^{N}(X_{Pi} - X_{Oi})^2\right)^{0.5} \tag{9}$$

A model skill metric (Willmott 1981) which ranges from 0 (no skill) to 1 (high skill) was applied

$$Skill = 1 - \frac{\sum_{i=1}^{N}|X_{Pi} - X_{Oi}|^2}{\sum_{i=1}^{N}\left(\left|X_{Pi} - \overline{X_O}\right| + \left|X_{Oi} - \overline{X_O}\right|\right)^2} \tag{10}$$

This skill metric was evaluated both for primary and secondary velocity components for each transect.

RESULTS

2019

Velocity data were collected at 12 cross-sections in the 2019 UCD study (Figure 9). At each location in the cross-section where velocity was estimated from ADCP data, the predicted depth-averaged speed was compared to observed depth-averaged speed (Figure 11). The observed depth-averaged speed was predicted accurately by the model with a small negative bias (underestimated speed) and an average skill of 0.834 and a maximum RMSD of 0.228 m/s (Table 2).

Figure 11 Depth-Averaged Velocities

Figure 11 shows observed (black) and predicted (green) depth-averaged velocity vectors at each cross-section on March 27, 2019.

Table 2 Difference metrics for depth-averaged speed for the March 27, 2019 survey

Transect	Observed (m/s)	Predicted (m/s)	Bias (m/s)	RMSD (m/s)	Skill
JCT	0.781	0.717	-0.064	0.145	0.831
OR1	0.985	0.850	-0.135	0.228	0.780
SJD1	0.583	0.497	-0.086	0.202	0.734
SJD2	0.383	0.380	-0.003	0.164	0.412
SJD3	0.757	0.722	-0.035	0.111	0.872
SJU01	0.961	0.902	-0.060	0.144	0.931
SJU02	0.953	0.864	-0.089	0.135	0.918
SJU03	0.956	0.837	-0.119	0.171	0.893
SJU04	1.003	0.872	-0.131	0.166	0.878
SJU05	0.968	0.903	-0.065	0.126	0.922
SJU06	0.824	0.797	-0.027	0.134	0.935
SJU07	0.840	0.791	-0.049	0.108	0.902

Predicted velocity fields were compared with observations for all cross-sections in the 2019 dataset in Figure 12 through Figure 23. These figures show the location of each cross section (upper left), compare depth-averaged velocities (upper right), observed and predicted streamwise velocity (left panels below top row), observed and predicted secondary velocity (right panels below top row). The observed and predicted streamwise velocities are similar in magnitude and distribution. The observations sometimes show peak velocity concentrated in a narrow portion of the cross-section while the predicted streamwise velocity distribution typically varies more smoothly. The observations do not extend to the bed so it is uncertain whether near bed velocity was predicted accurately. The right columns of Figure 12 through Figure 23 show observed and predicted secondary circulation with the bottom rows showing the depth-averaged magnitude of the lateral velocity component. The predicted structure matched the observations closely but was somewhat more spatially uniform, while the observed secondary circulation was slightly patchy, perhaps due to some remaining turbulence or instrument noise in the processed ADCP observations. The bottom rows of Figure 12 through Figure 23 shows strength of streamwise and secondary circulation for each water column for both observations and predictions. The strength of each was generally predicted well with the pattern of predictions being smoother than the observed velocity distribution.

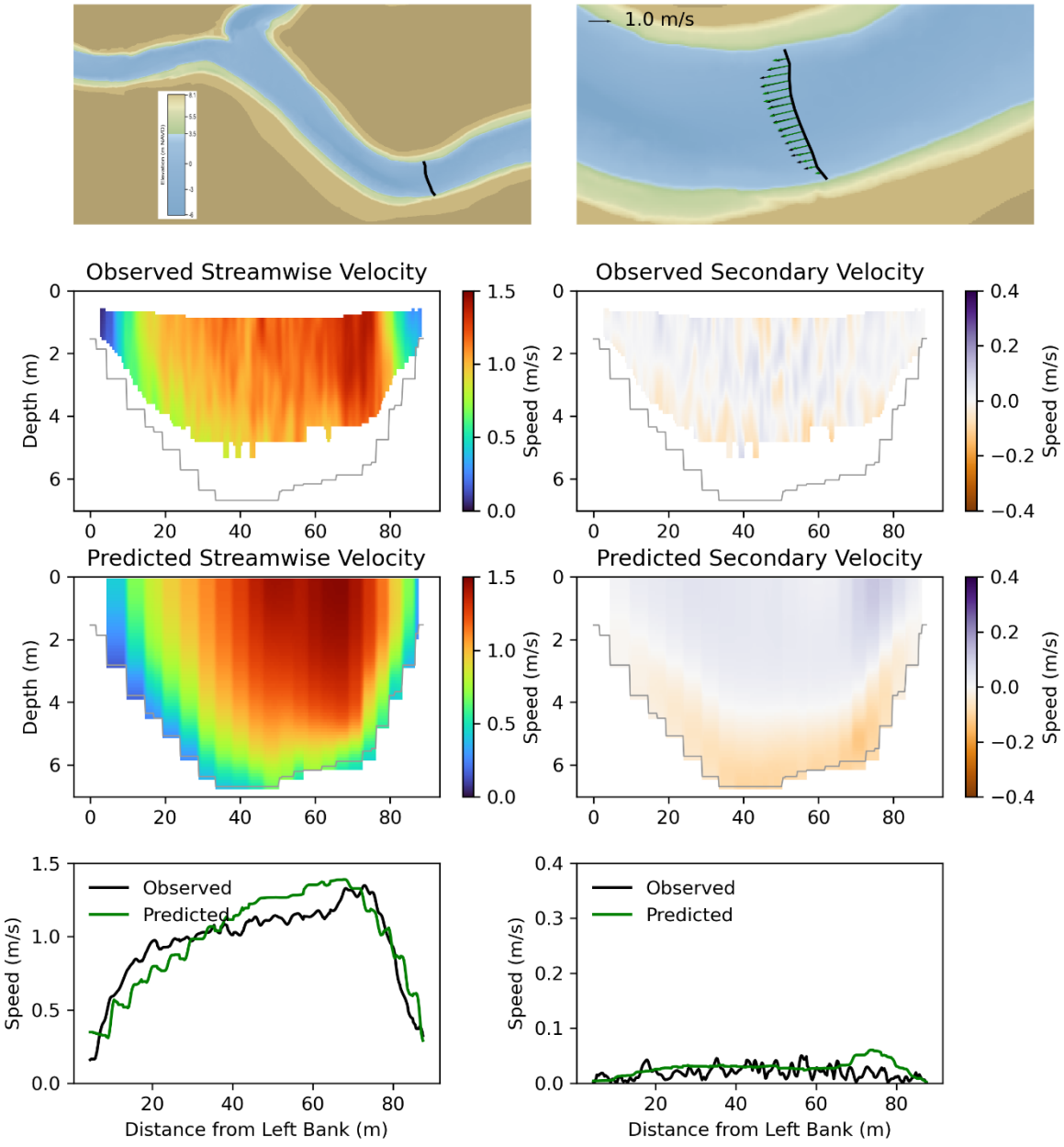

Figure 12 Streamwise and secondary velocity at cross-section SJU01.

Figure 12 depicts three charts. The top row shows the location of the cross section in the study area (left) and the observed and predicted depth-averaged velocity (right). The middle rows compare observed and predicted streamwise velocity distribution (left) and secondary (lateral) velocity information (right). The bottom row shows the magnitude (absolute value) of depth-averaged streamwise velocity (left) and secondary velocity (right).

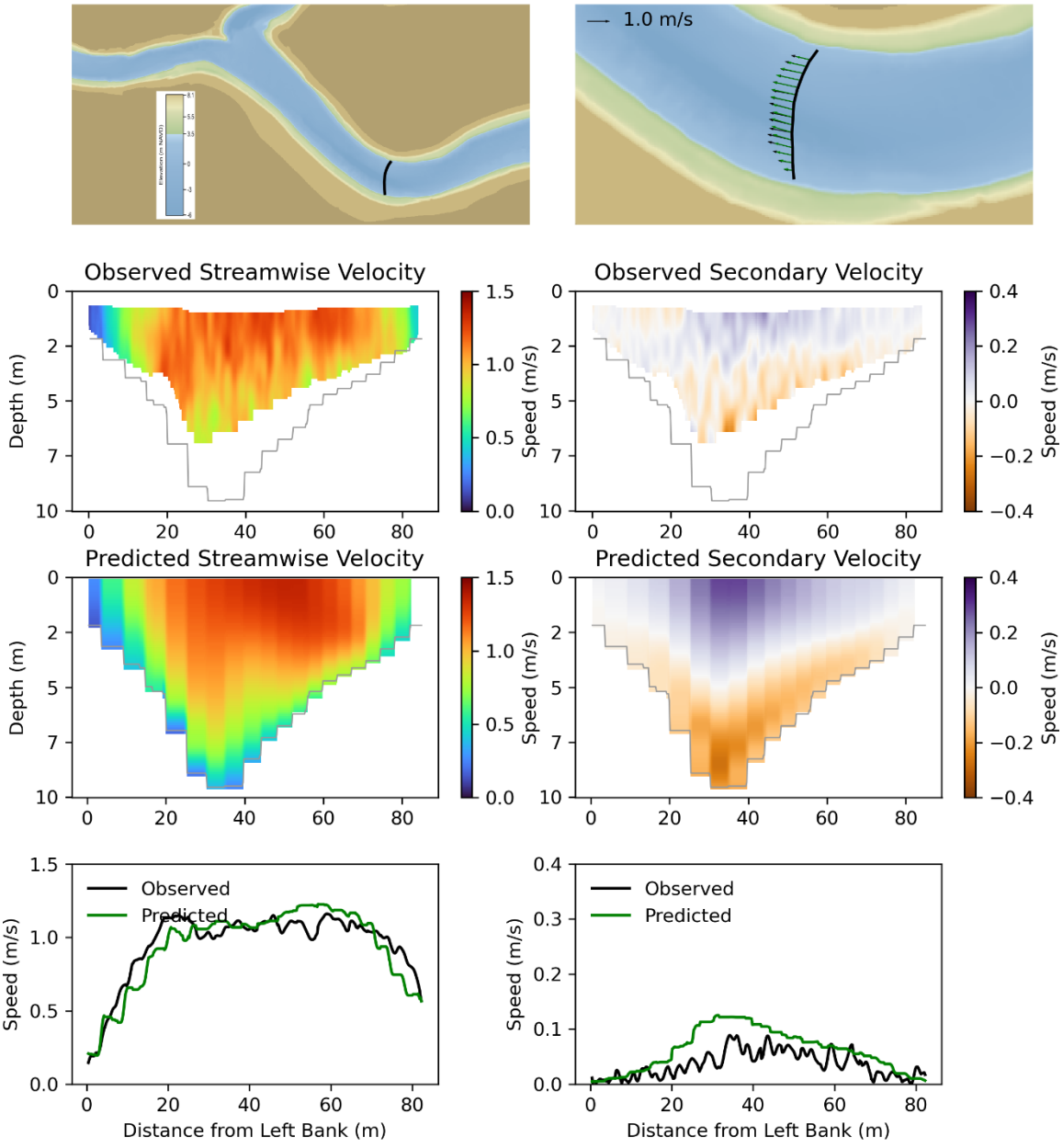

Figure 13 Streamwise and secondary velocity at cross-section SJU02.

Figure 13 depicts three charts. The top row shows the location of the cross section in the study area (left) and the observed and predicted depth-averaged velocity (right). The middle rows compare observed and predicted streamwise velocity distribution (left) and secondary (lateral) velocity information (right). The bottom row shows the magnitude (absolute value) of depth-averaged streamwise velocity (left) and secondary velocity (right).

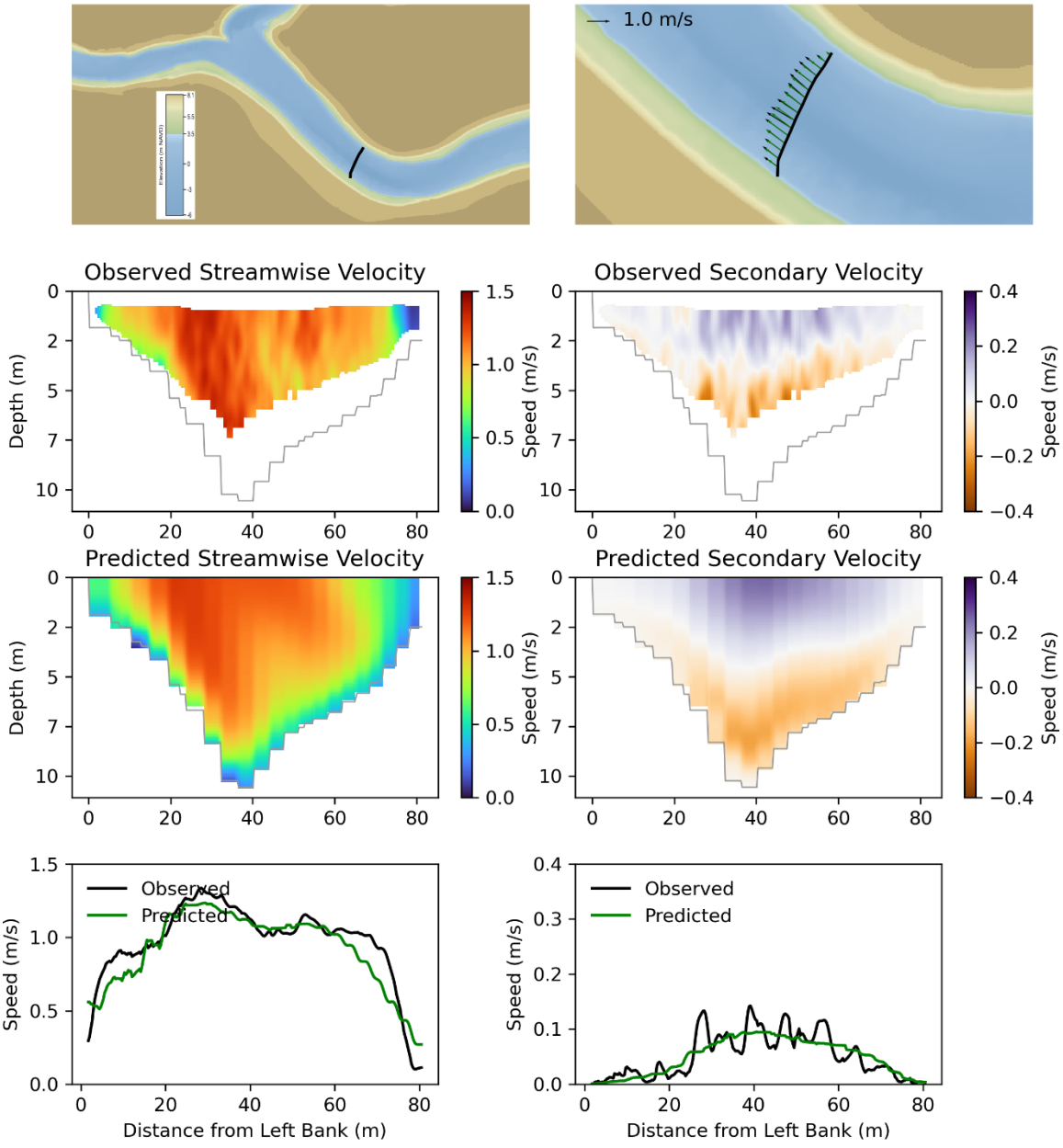

Figure 14 Streamwise and secondary velocity at cross-section SJU03.

Figure 14 depicts three charts. The top row shows the location of the cross section in the study area (left) and the observed and predicted depth-averaged velocity (right). The middle rows compare observed and predicted streamwise velocity distribution (left) and secondary (lateral) velocity information (right). The bottom row shows the magnitude (absolute value) of depth-averaged streamwise velocity (left) and secondary velocity (right).

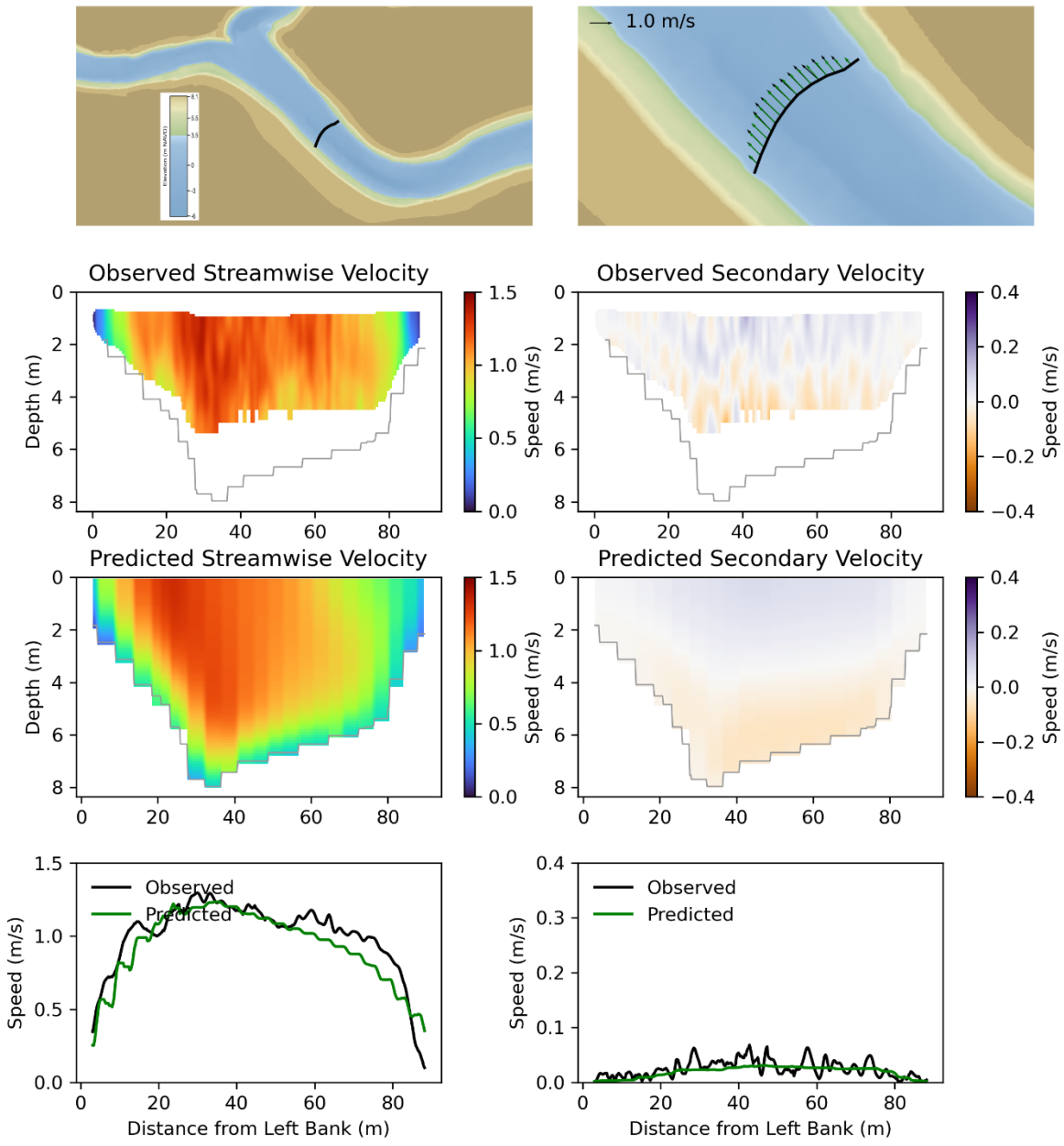

Figure 15 Streamwise and secondary velocity at cross-section SJU04.

Figure 15 depicts three charts. The top row shows the location of the cross section in the study area (left) and the observed and predicted depth-averaged velocity (right). The middle rows compare observed and predicted streamwise velocity distribution (left) and secondary (lateral) velocity information (right). The bottom row shows the magnitude (absolute value) of depth-averaged streamwise velocity (left) and secondary velocity (right).

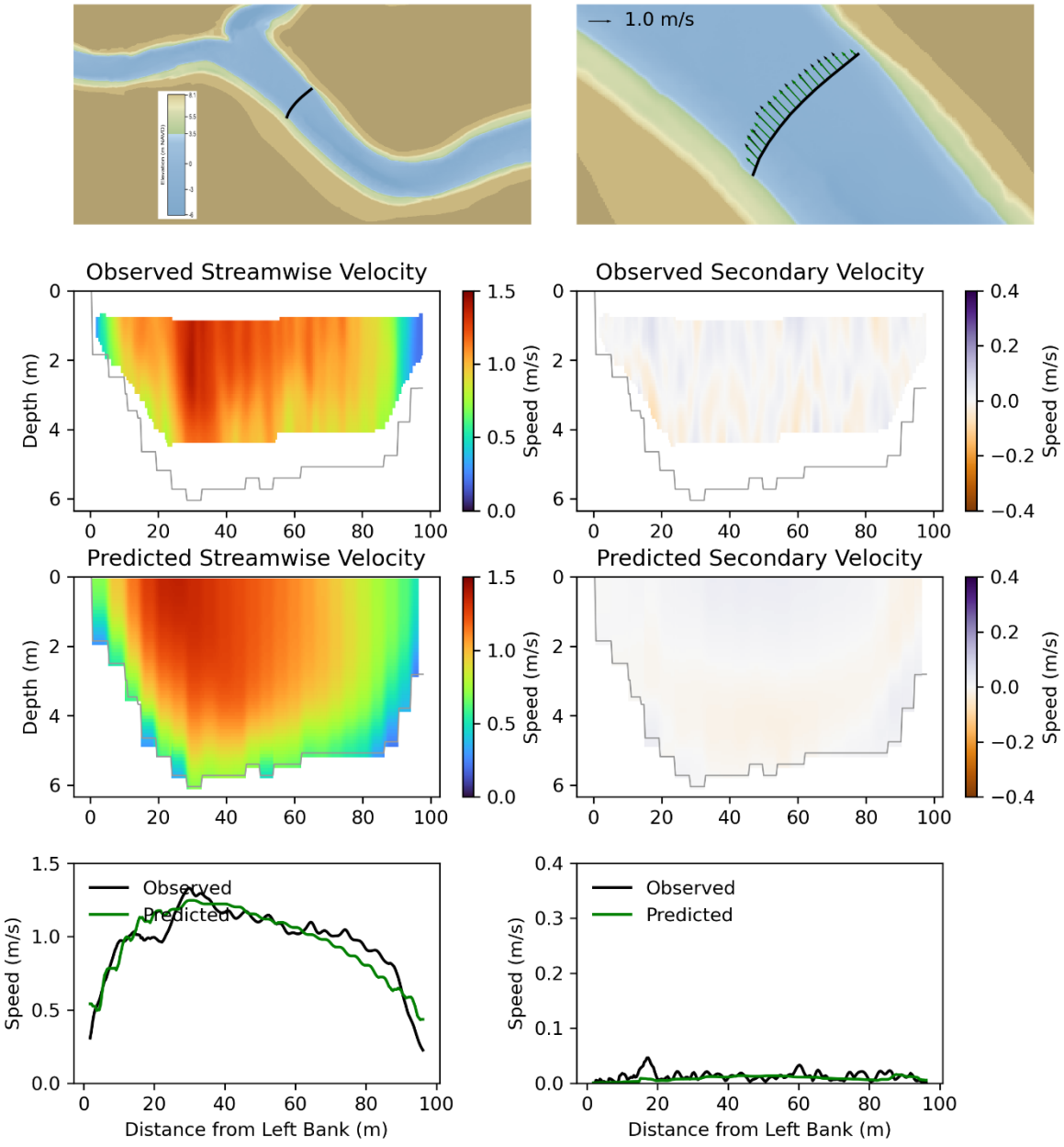

Figure 16 Streamwise and secondary velocity at cross-section SJU05.

Figure 16 depicts three charts. The top row shows the location of the cross section in the study area (left) and the observed and predicted depth-averaged velocity (right). The middle rows compare observed and predicted streamwise velocity distribution (left) and secondary (lateral) velocity information (right). The bottom row shows the magnitude (absolute value) of depth-averaged streamwise velocity (left) and secondary velocity (right).

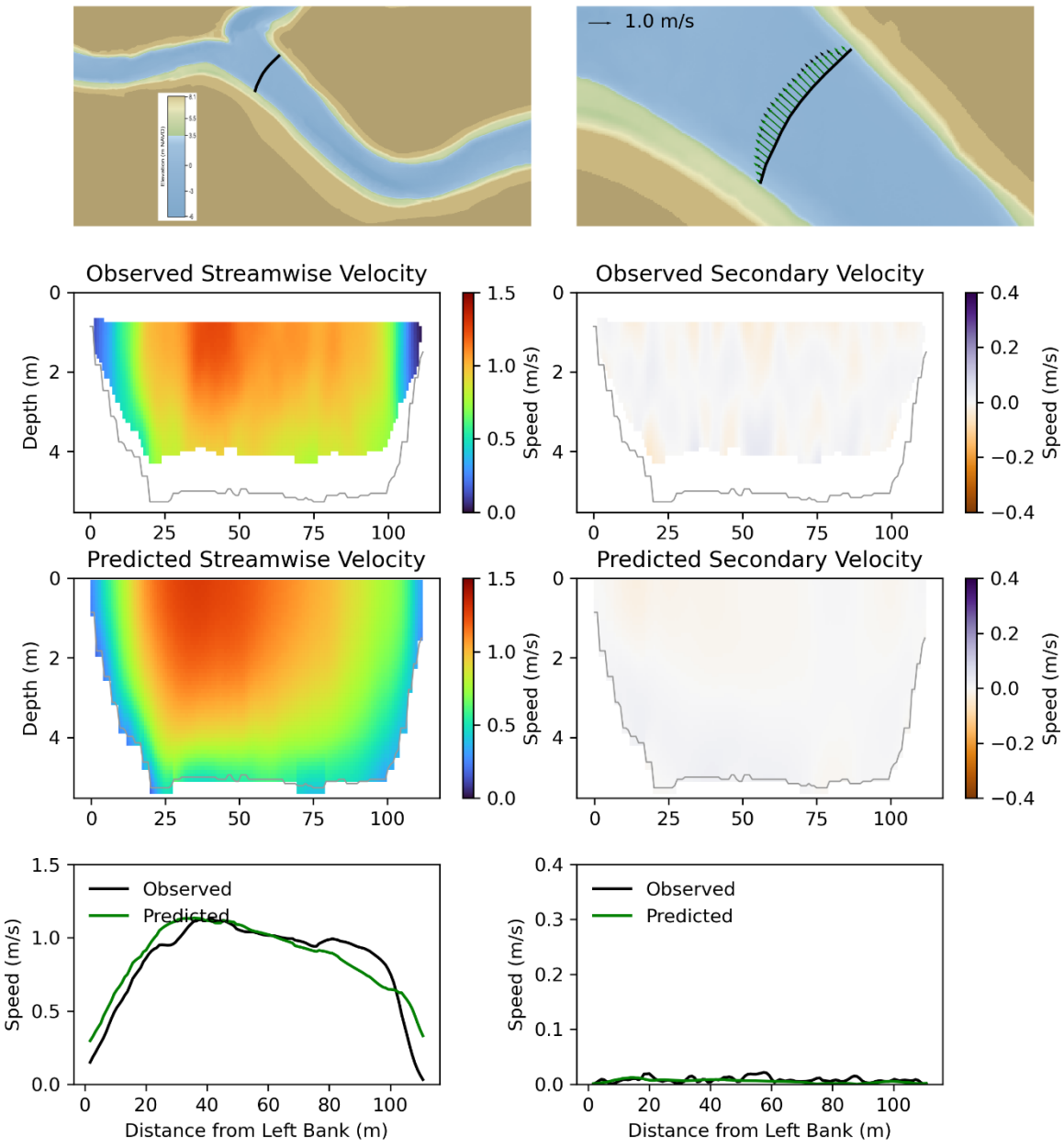

Figure 17 Streamwise and secondary velocity at cross-section SJU06.

Figure 17 depicts three charts. The top row shows the location of the cross section in the study area (left) and the observed and predicted depth-averaged velocity (right). The middle rows compare observed and predicted streamwise velocity distribution (left) and secondary (lateral) velocity information (right). The bottom row shows the magnitude (absolute value) of depth-averaged streamwise velocity (left) and secondary velocity (right).

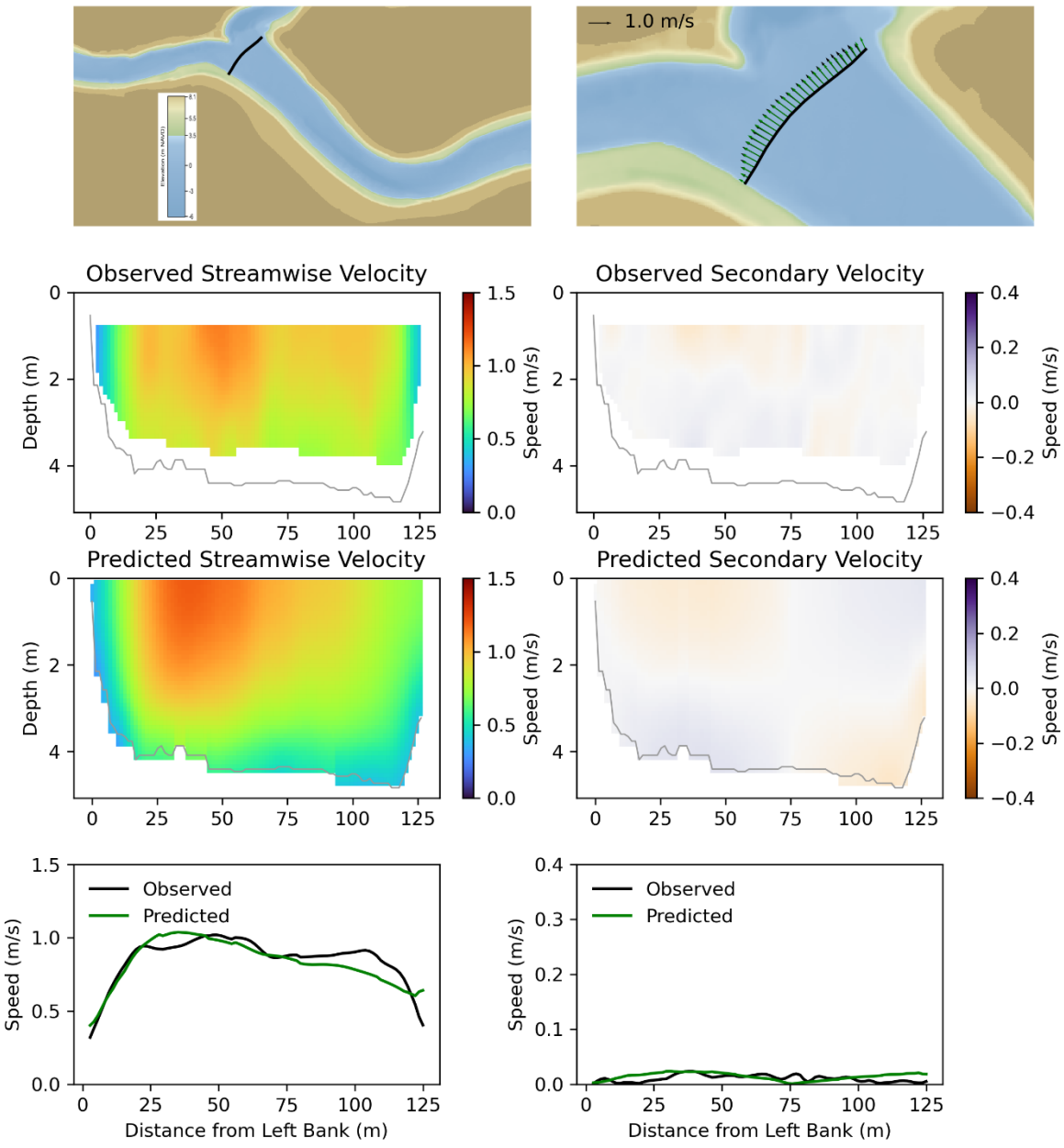

Figure 18 Streamwise and secondary velocity at cross-section SJU07.

Figure 18 depicts three charts. The top row shows the location of the cross section in the study area (left) and the observed and predicted depth-averaged velocity (right). The middle rows compare observed and predicted streamwise velocity distribution (left) and secondary (lateral) velocity information (right). The bottom row shows the magnitude (absolute value) of depth-averaged streamwise velocity (left) and secondary velocity (right).

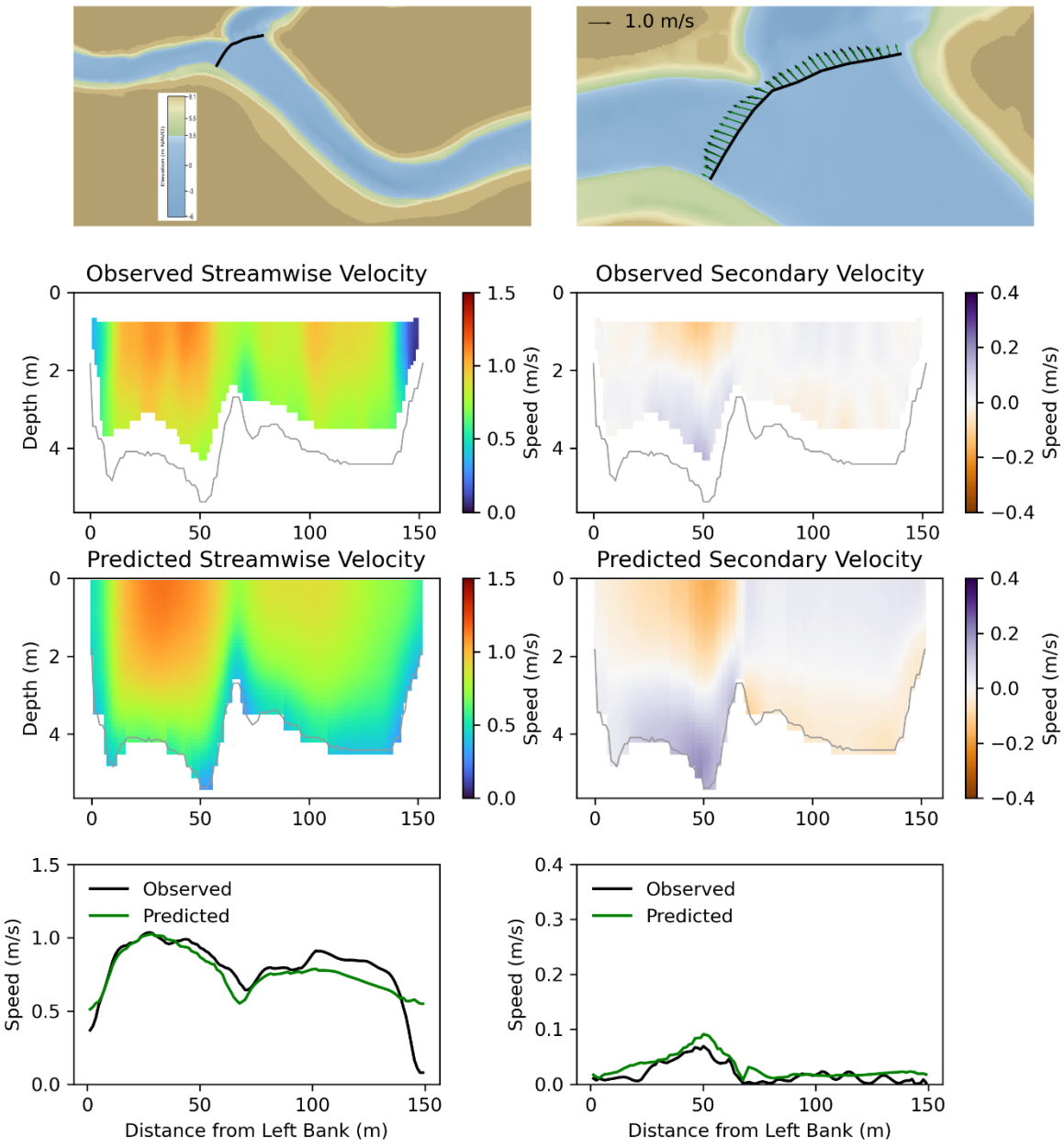

Figure 19 Streamwise and secondary velocity at cross-section JCT.

Figure 19 depicts three charts. The top row shows the location of the cross section in the study area (left) and the observed and predicted depth-averaged velocity (right). The middle rows compare observed and predicted streamwise velocity distribution (left) and secondary (lateral) velocity information (right). The bottom row shows the magnitude (absolute value) of depth-averaged streamwise velocity (left) and secondary velocity (right).

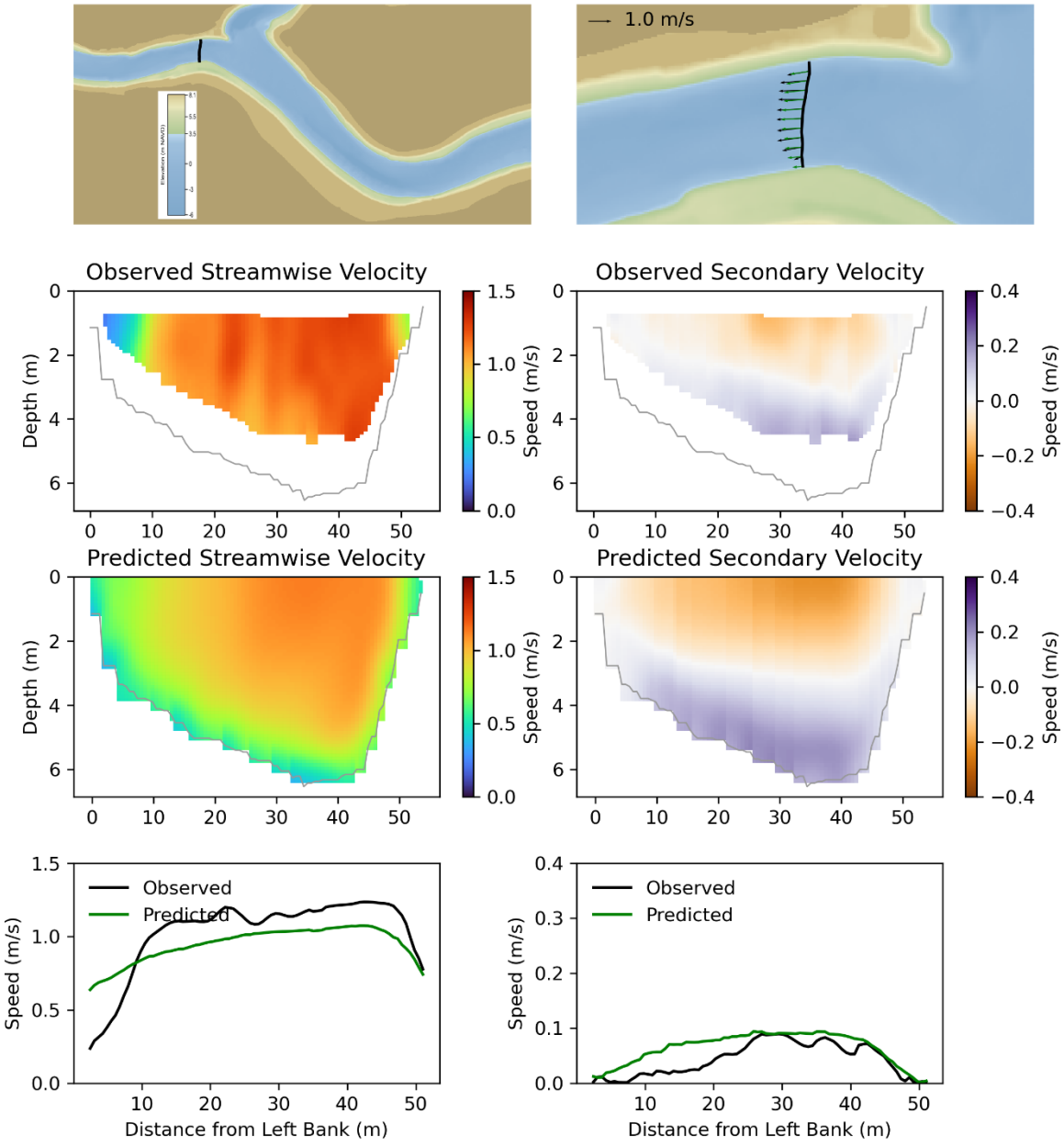

Figure 20 Streamwise and secondary velocity at cross-section OR1.

Figure 20 depicts three charts. The top row shows the location of the cross section in the study area (left) and the observed and predicted depth-averaged velocity (right). The middle rows compare observed and predicted streamwise velocity distribution (left) and secondary (lateral) velocity information (right). The bottom row shows the magnitude (absolute value) of depth-averaged streamwise velocity (left) and secondary velocity (right).

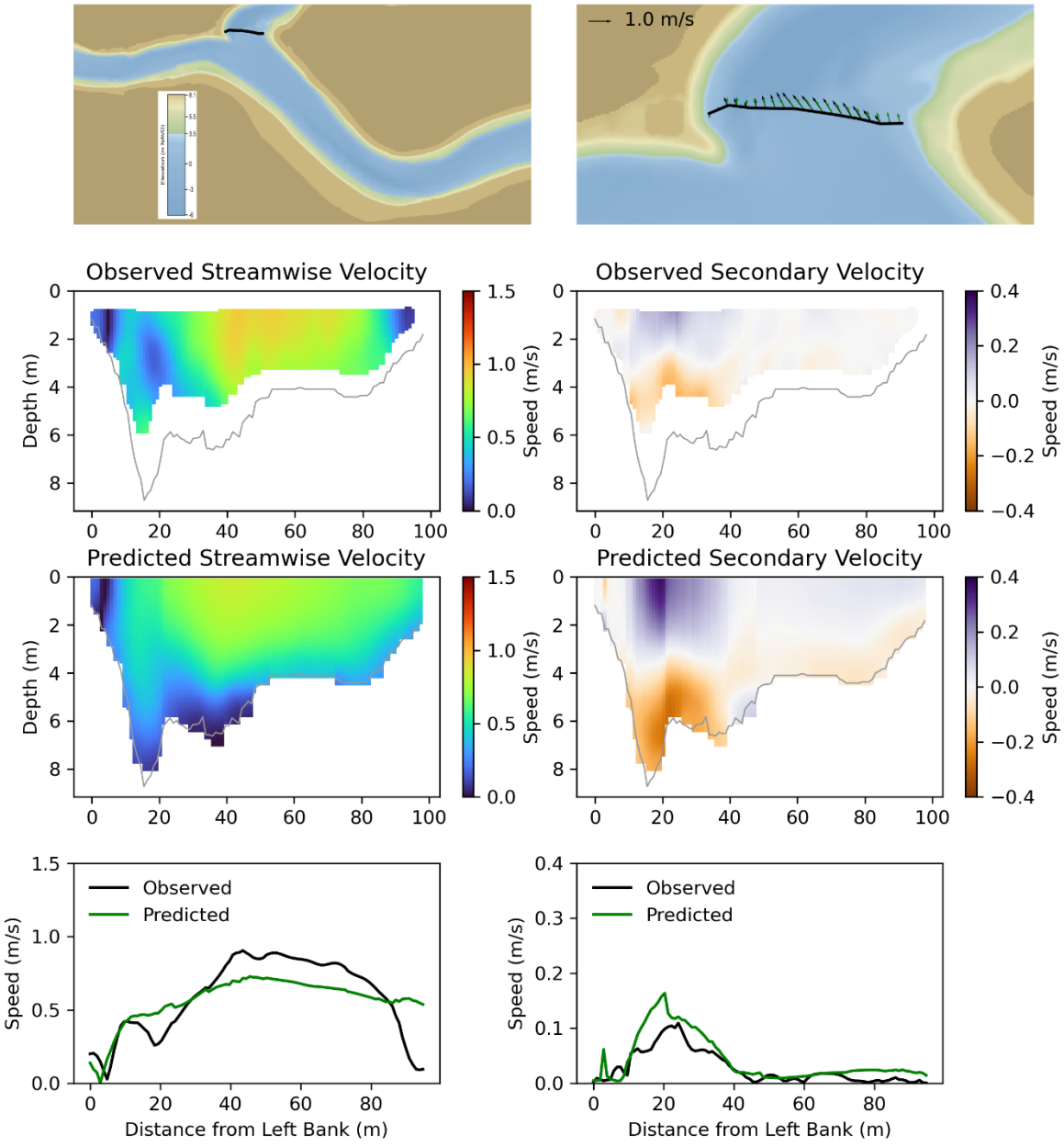

Figure 21 Streamwise and secondary velocity at cross-section SJD1.

Figure 21 depicts three charts. The top row shows the location of the cross section in the study area (left) and the observed and predicted depth-averaged velocity (right). The middle rows compare observed and predicted streamwise velocity distribution (left) and secondary (lateral) velocity information (right). The bottom row shows the magnitude (absolute value) of depth-averaged streamwise velocity (left) and secondary velocity (right).

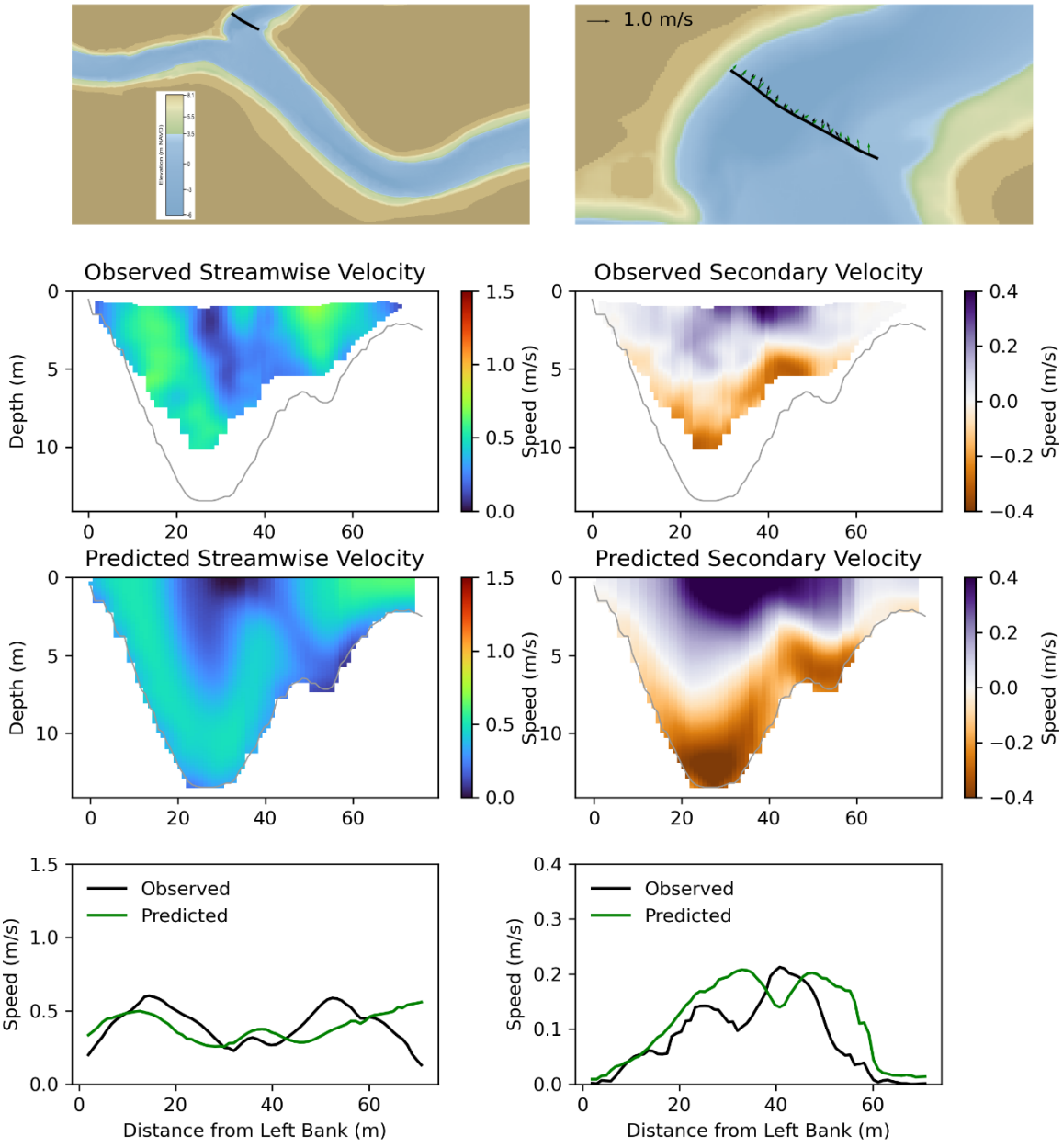

Figure 22 Streamwise and secondary velocity at cross-section SJD2.

Figure 22 depicts three charts. The top row shows the location of the cross section in the study area (left) and the observed and predicted depth-averaged velocity (right). The middle rows compare observed and predicted streamwise velocity distribution (left) and secondary (lateral) velocity information (right). The bottom row shows the magnitude (absolute value) of depth-averaged streamwise velocity (left) and secondary velocity (right).

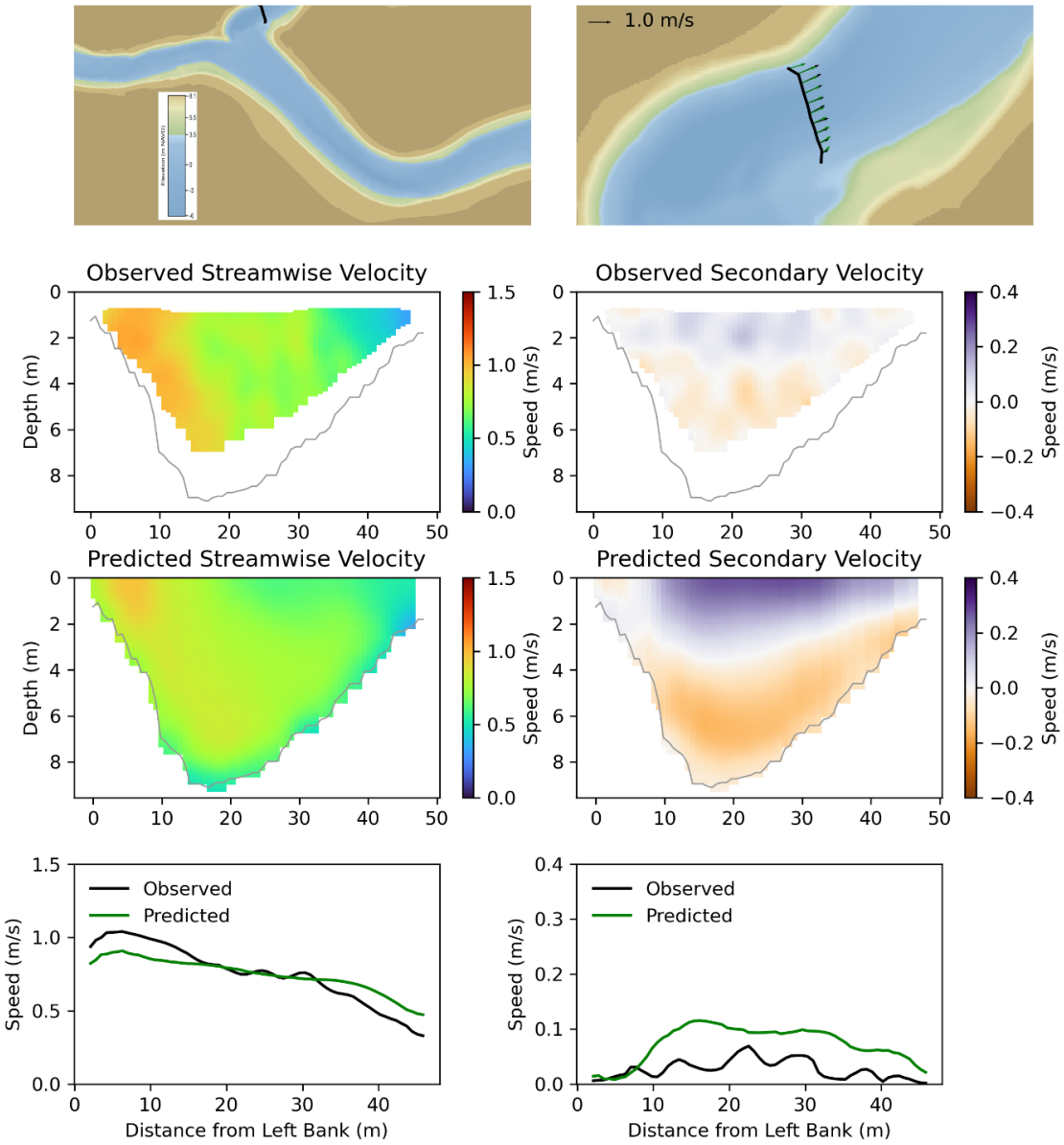

Figure 23 Streamwise and secondary velocity at cross-section SJD3.

Figure 23 depicts three charts. The top row shows the location of the cross section in the study area (left) and the observed and predicted depth-averaged velocity (right). The middle rows compare observed and predicted streamwise velocity distribution (left) and secondary (lateral) velocity information (right). The bottom row shows the magnitude (absolute value) of depth-averaged streamwise velocity (left) and secondary velocity (right).

Both streamwise (primary) and secondary velocities are summarized for all transects for March 28, 2019 in Figure 24 and Figure 25. Some systematic differences can be noted. First the predicted velocity distribution was smoother. Second the strength of secondary circulation was often overestimated by the model.

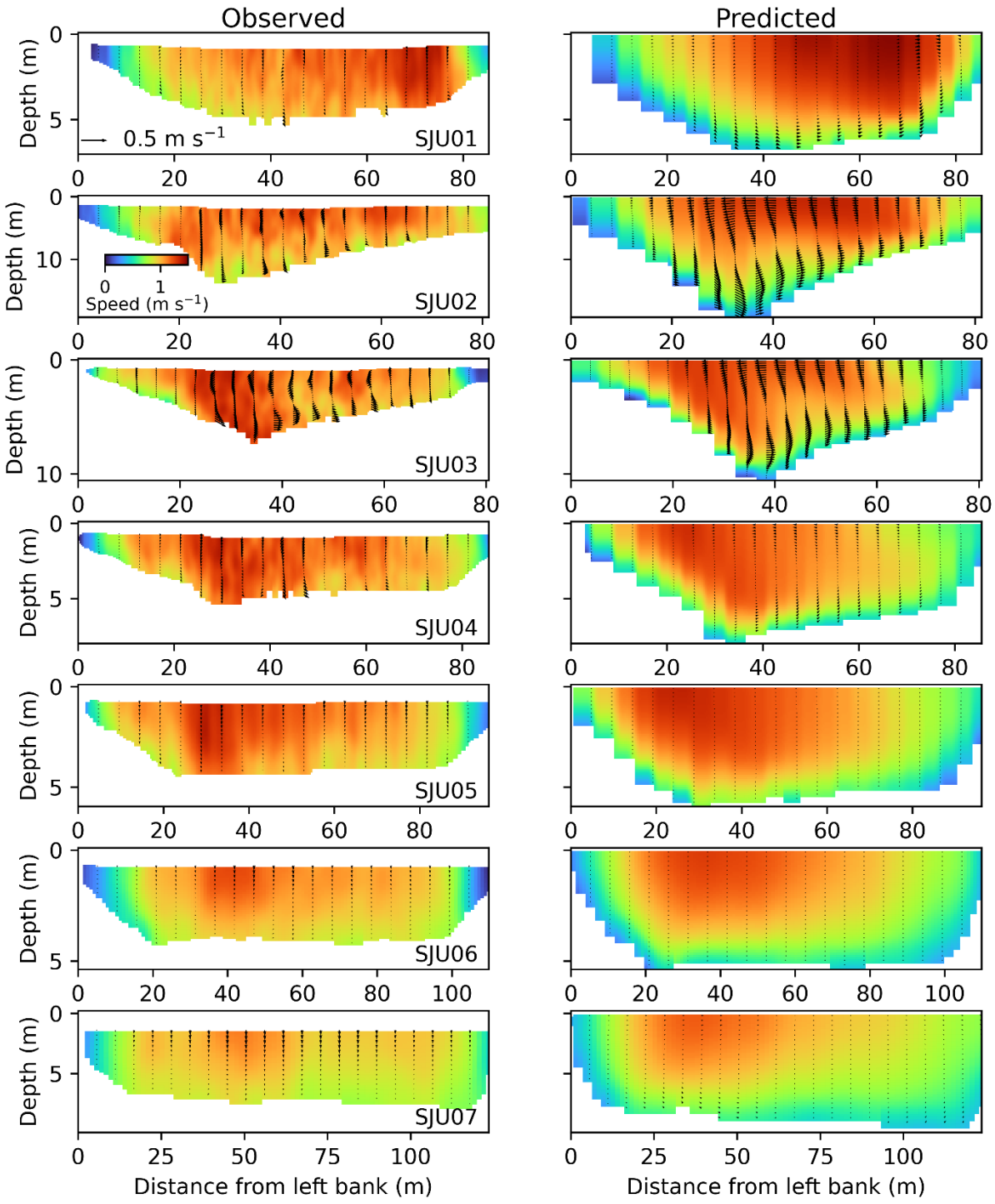

Figure 24 Streamwise and secondary velocity at all cross-sections upstream of the junction on March 27, 2019.

Figure 24 shows observed and predicted streamwise and secondary velocity distributions across cross-sections SJU01–SJU07 upstream of the junction on March 27, 2019, plotted as velocity magnitude and velocity vectors versus depth and distance from the left bank.

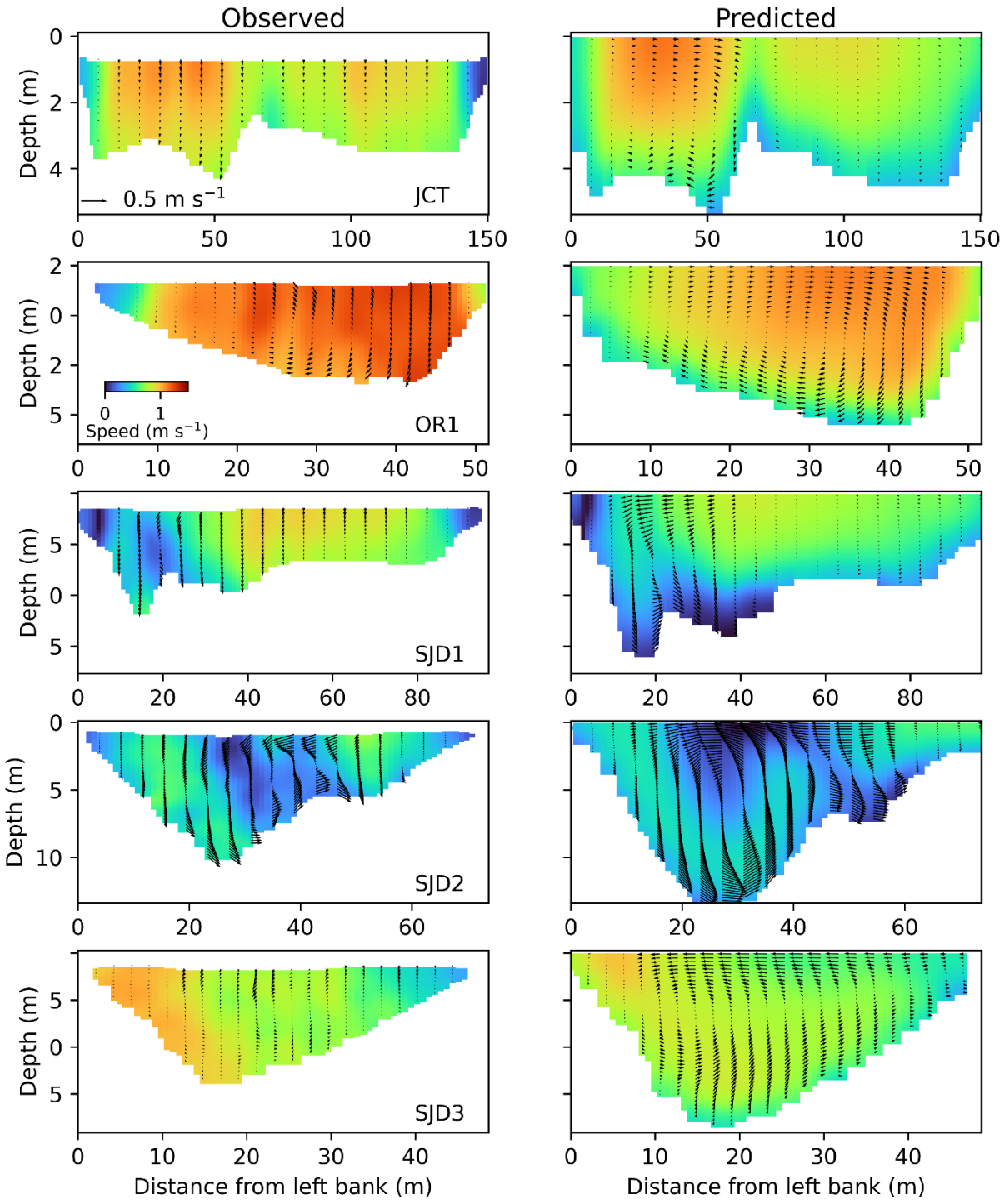

Figure 25 Streamwise and secondary velocity at all cross-sections at and downstream of the junction on March 27, 2019.

Figure 25 shows observed and predicted streamwise and secondary velocity distributions across cross-sections JCT, OR1, and SJD1–SJD3 at and downstream of the junction on March 27, 2019, plotted as velocity magnitude and velocity vectors versus depth and distance from the left bank.

We calculated bias, RMSD and model skill for streamwise (Table 3) and secondary (Table 4) velocities at each transect. To calculate these metrics, we interpolated predicted velocities to the locations of observed velocities. The streamwise velocity was slightly underpredicted by the model and the average RMSD and skill were 0.139 m/s and 0.846, respectively. The depth-averaged observed secondary velocity calculated by the Rozovskii method was zero by definition. Predicted secondary velocities were rotated based on applying the Rozovskii method over the full water column, but the comparison to observations was only over the subset of the water column measured by the ADCP. Due to this difference in spatial extent the average predicted secondary velocity can be nonzero. The secondary velocity was generally predicted well with a RMSD of 0.069 m/s and an average skill of 0.609. Note that the cross-sections with lowest skill scores were the cross-sections SJU04 to SJU07 which were in straight channel regions (Figure 9), as opposed to channel bends, and had negligible secondary velocities (Figure 24).

Table 3 Difference metrics for streamwise velocity for the March 27, 2019 survey.

Transect	Observed (m/s)	Predicted (m/s)	Bias (m/s)	RMSD (m/s)	Skill
JCT	0.819	0.781	-0.038	0.126	0.862
OR1	1.101	0.986	-0.115	0.176	0.731
SJD1	0.612	0.578	-0.034	0.169	0.806
SJD2	0.413	0.363	-0.051	0.173	0.632
SJD3	0.787	0.772	-0.015	0.122	0.772
SJU01	1.024	1.058	0.034	0.161	0.898
SJU02	1.005	1.003	-0.002	0.136	0.903
SJU03	1.058	1.014	-0.044	0.134	0.905
SJU04	1.061	0.997	-0.065	0.133	0.901
SJU05	1.021	1.017	-0.005	0.113	0.926
SJU06	0.901	0.911	0.010	0.124	0.922
SJU07	0.866	0.843	-0.023	0.106	0.894

Table 4 Difference metrics for secondary velocity for the March 27, 2019 survey. Note that observed secondary velocity was zero by construction following the Rozovskii method to calculate velocity components.

Transect	Observed (m/s)	Predicted (m/s)	Bias (m/s)	RMSD (m/s)	Skill
JCT	0.000	-0.003	-0.003	0.050	0.754
OR1	0.000	-0.037	-0.037	0.068	0.840
SJD1	0.000	0.022	0.022	0.072	0.772
SJD2	0.000	0.063	0.063	0.132	0.835
SJD3	0.000	-0.001	-0.001	0.103	0.632
SJU01	0.000	0.018	0.018	0.058	0.509
SJU02	0.000	0.029	0.029	0.086	0.729
SJU03	0.000	0.025	0.025	0.078	0.804
SJU04	0.000	0.009	0.009	0.058	0.527
SJU05	0.000	-0.003	-0.003	0.042	0.300
SJU06	0.000	-0.001	-0.001	0.044	0.193
SJU07	0.000	0.000	0.000	0.044	0.413

The nonhydrostatic simulations also predicted vertical velocity, which may contribute to scour processes in and near the scour hole. Comparisons of vertical velocity are shown for each transect in Figure 26 to Figure 37, and summarized in Table 5. The vertical velocity was typically low in the cross-sections upstream of the junction and strongest over the scour hole at SJD2 (Figure 36). While the spatial patterns of vertical velocities were predicted well, the peak predicted vertical velocities of up to 0.3 m/s were larger than observed values (Figure 36Figure 44). The RMSD was 0.055 m/s and the mean model skill was 0.507.

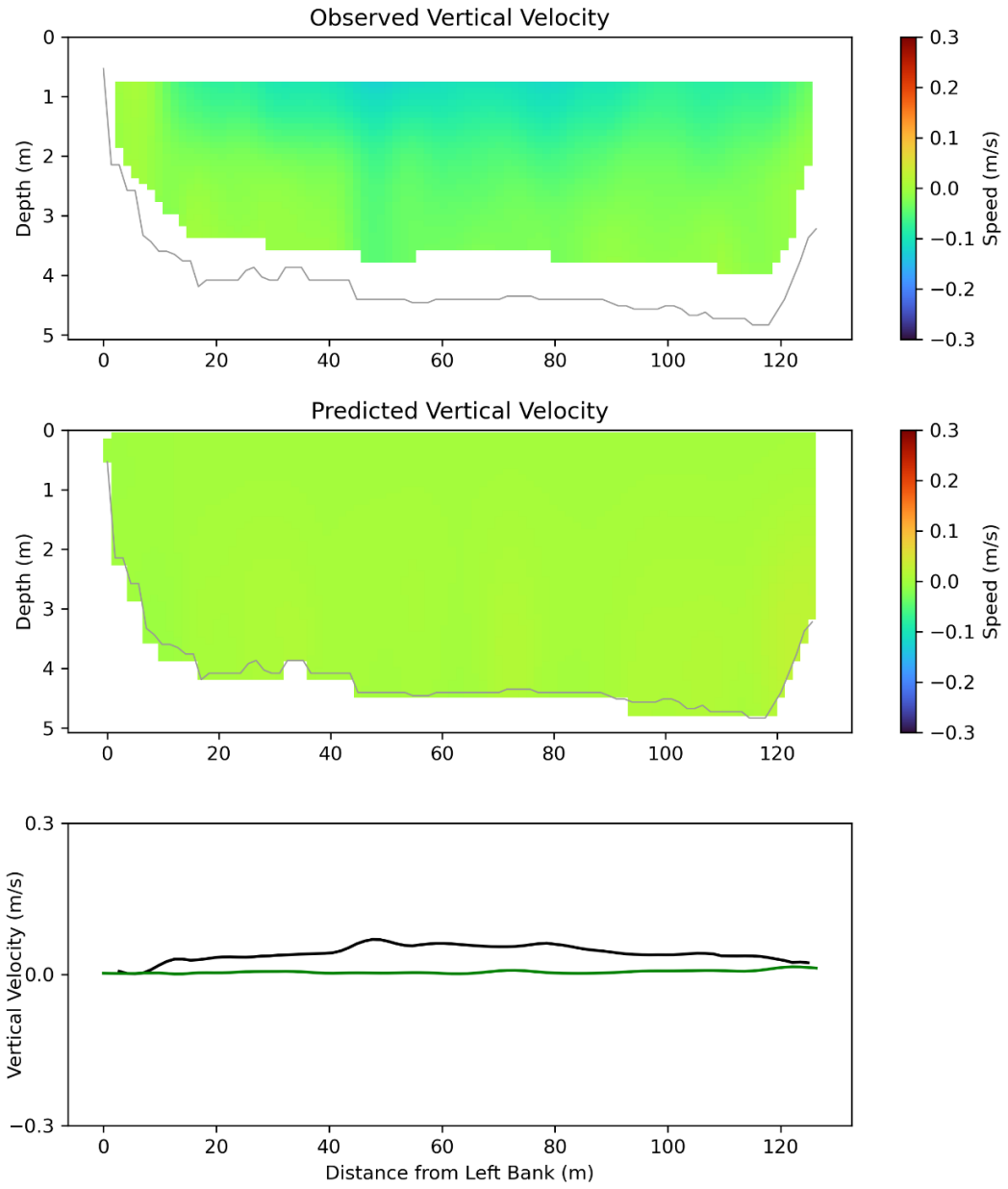

Figure 26 Vertical velocity at cross-section SJ01.

Figure 26 shows observed (top panel) and predicted (middle panel) vertical velocity distributions and depth-averaged vertical velocity (bottom panel) at the identified cross section, plotted versus depth and distance from the left bank.

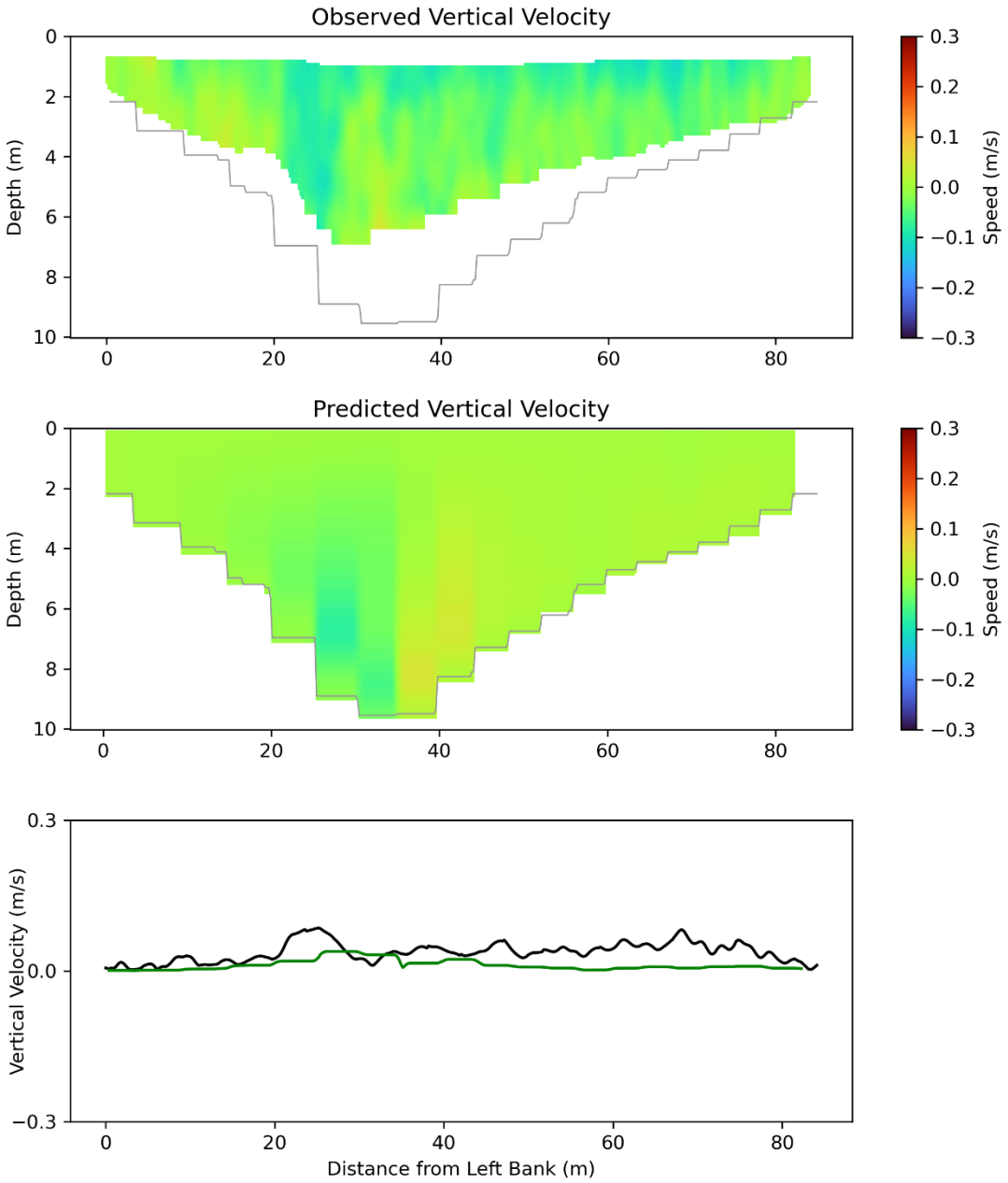

Figure 27 Vertical velocity at cross-section SJ02.

Figure 27 shows observed (top panel) and predicted (middle panel) vertical velocity distributions and depth-averaged vertical velocity (bottom panel) at the identified cross section, plotted versus depth and distance from the left bank.

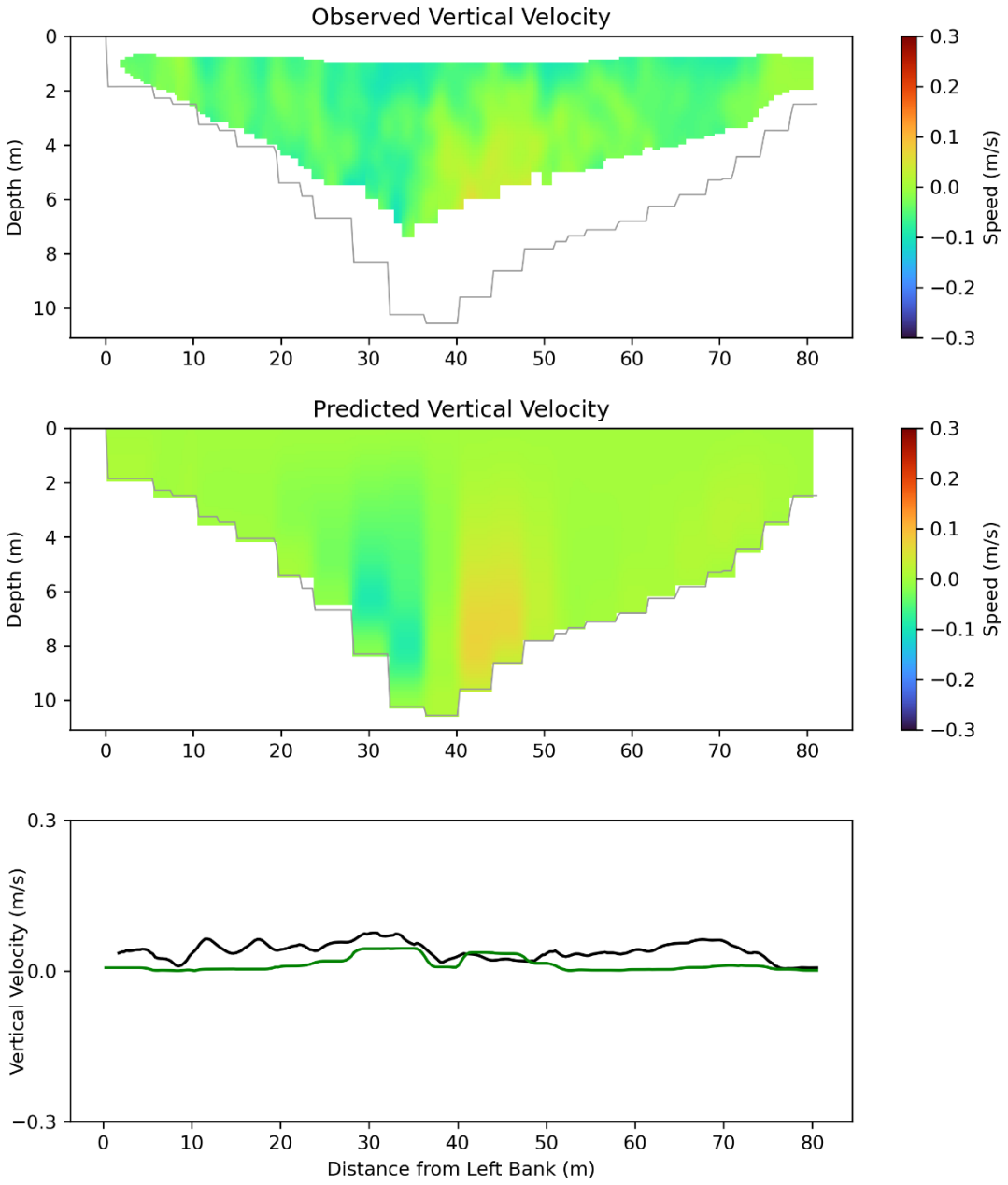

Figure 28 Vertical velocity at cross-section SJ03.

Figure 28 shows observed (top panel) and predicted (middle panel) vertical velocity distributions and depth-averaged vertical velocity (bottom panel) at the identified cross section, plotted versus depth and distance from the left bank.

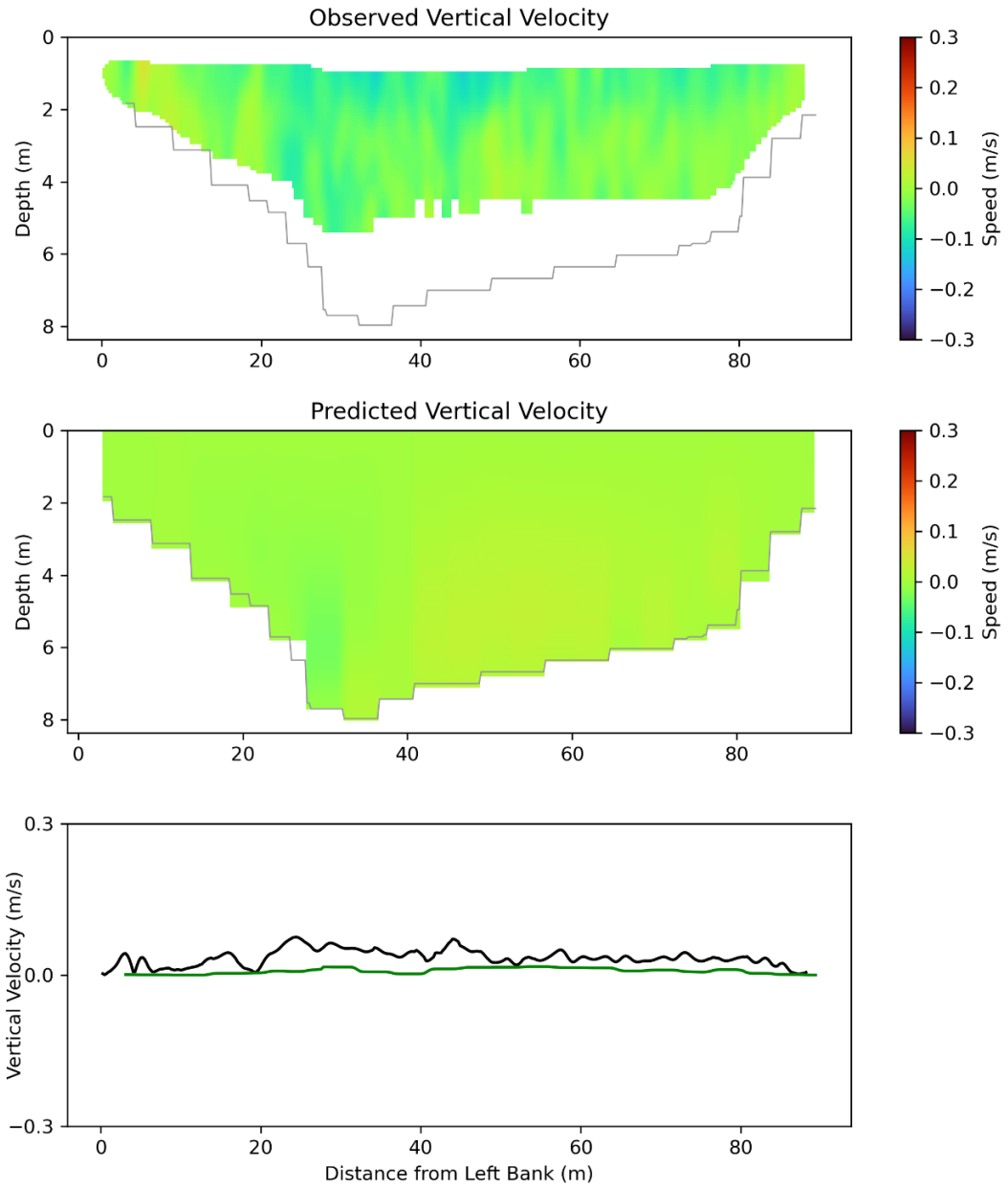

Figure 29 Vertical velocity at cross-section SJ04.

Figure 29 shows observed (top panel) and predicted (middle panel) vertical velocity distributions and depth-averaged vertical velocity (bottom panel) at the identified cross section, plotted versus depth and distance from the left bank.

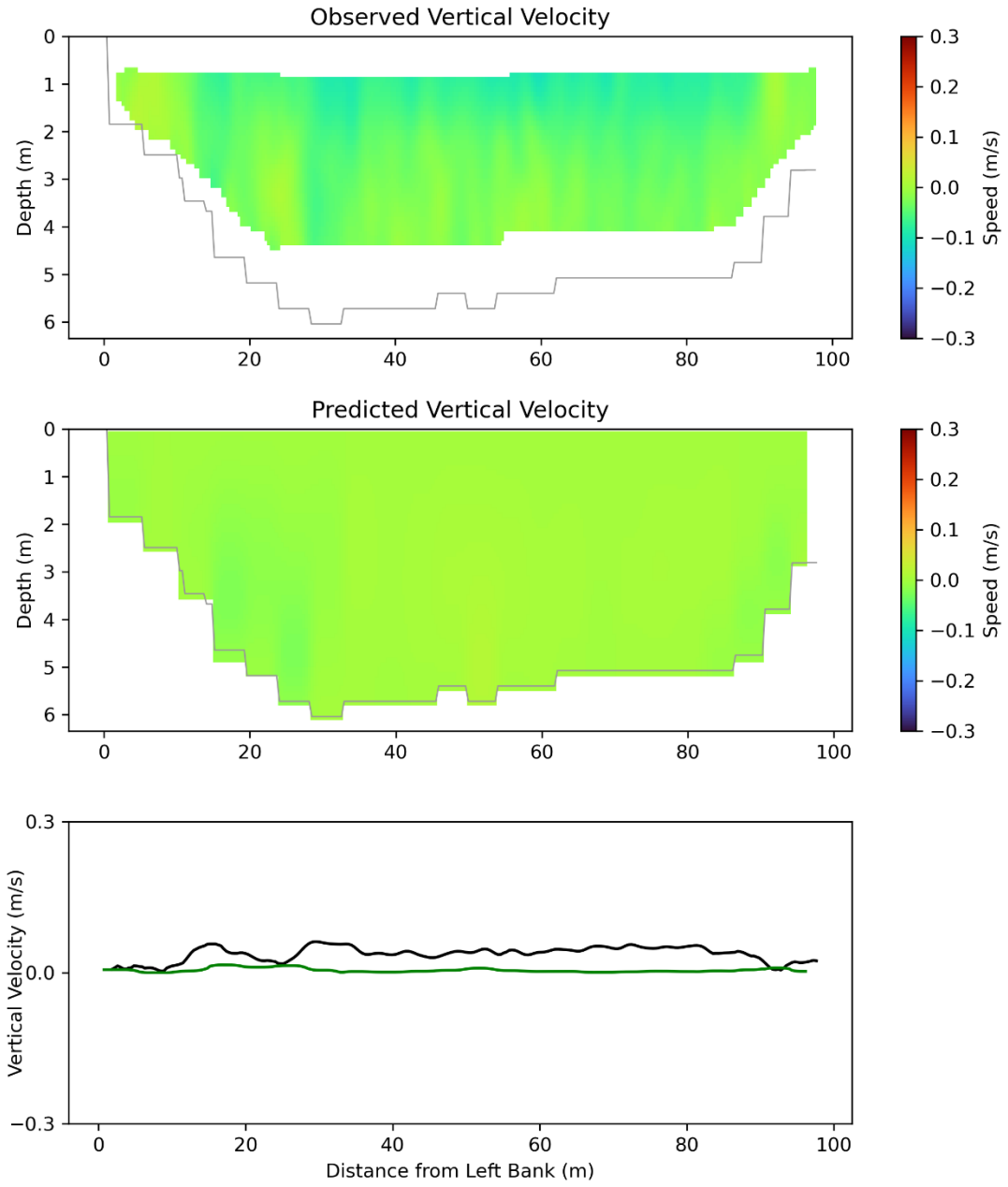

Figure 30 Vertical velocity at cross-section SJ05.

Figure 30 shows observed (top panel) and predicted (middle panel) vertical velocity distributions and depth-averaged vertical velocity (bottom panel) at the identified cross section, plotted versus depth and distance from the left bank.

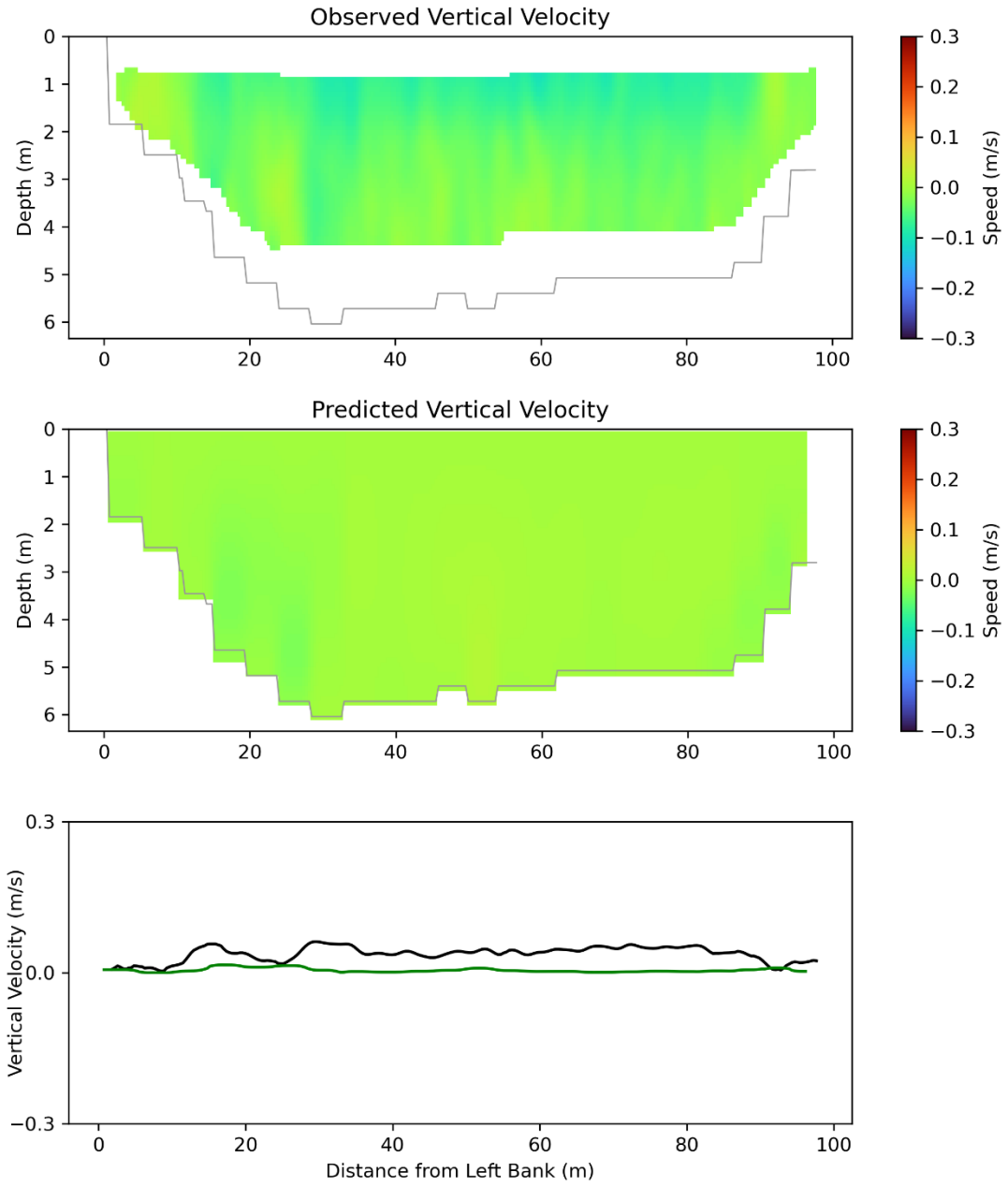

Figure 31 Vertical velocity at cross-section SJ06.

Figure 31 shows observed (top panel) and predicted (middle panel) vertical velocity distributions and depth-averaged vertical velocity (bottom panel) at the identified cross section, plotted versus depth and distance from the left bank.

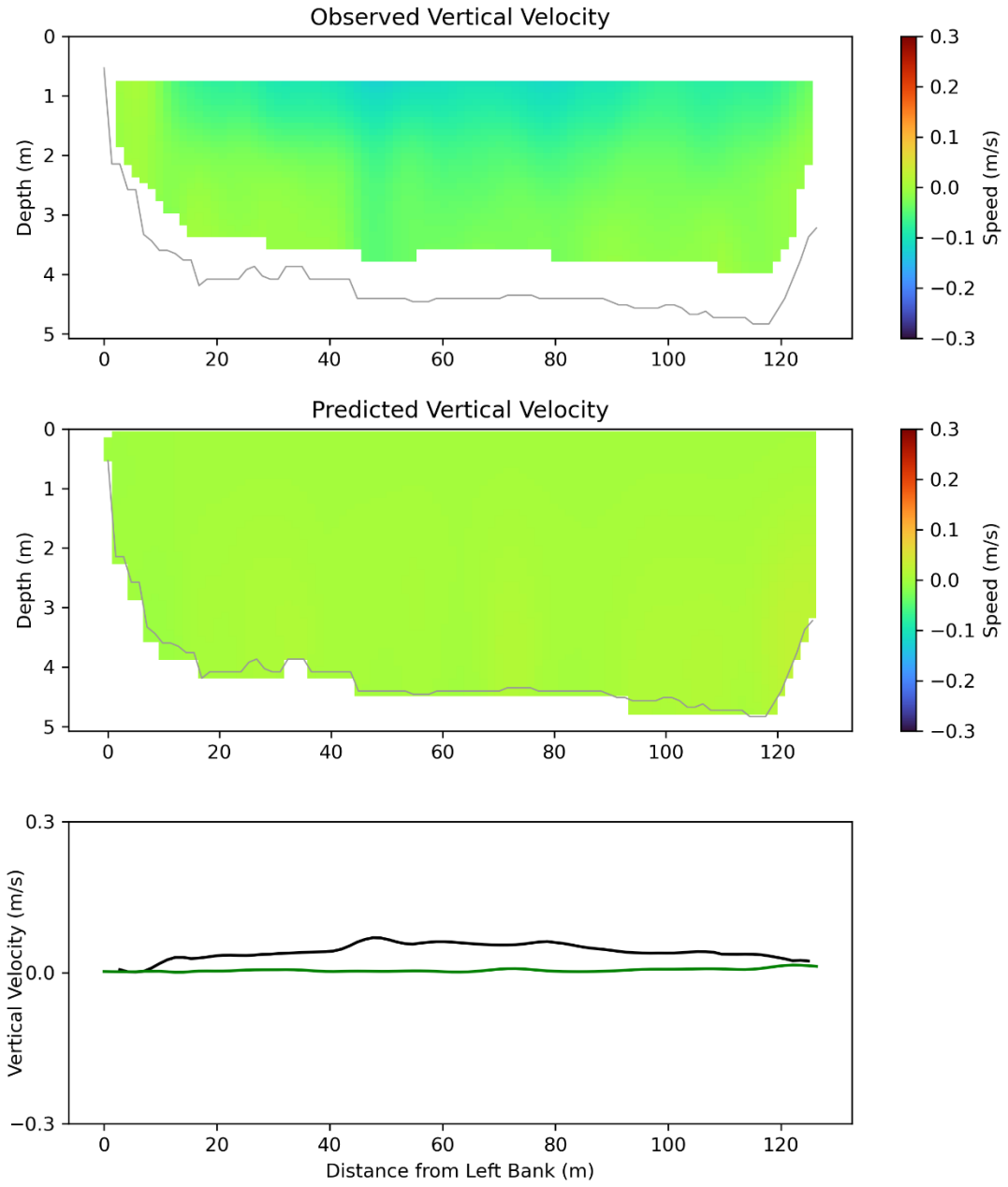

Figure 32 Vertical velocity at cross-section SJ07.

Figure 32 shows observed (top panel) and predicted (middle panel) vertical velocity distributions and depth-averaged vertical velocity (bottom panel) at the identified cross section, plotted versus depth and distance from the left bank.

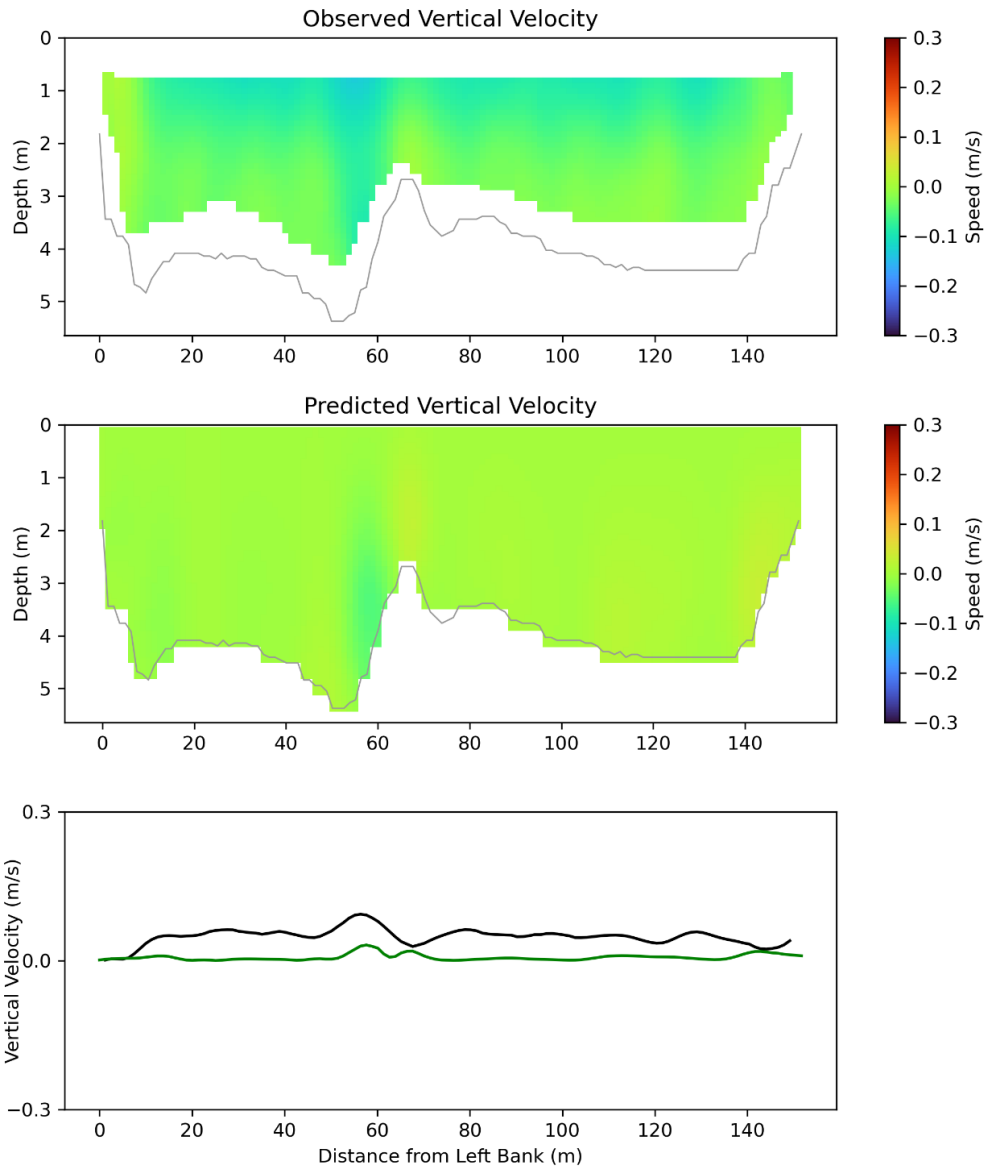

Figure 33 Vertical velocity at cross-section JCT.

Figure 33 shows observed (top panel) and predicted (middle panel) vertical velocity distributions and depth-averaged vertical velocity (bottom panel) at the identified cross section, plotted versus depth and distance from the left bank.

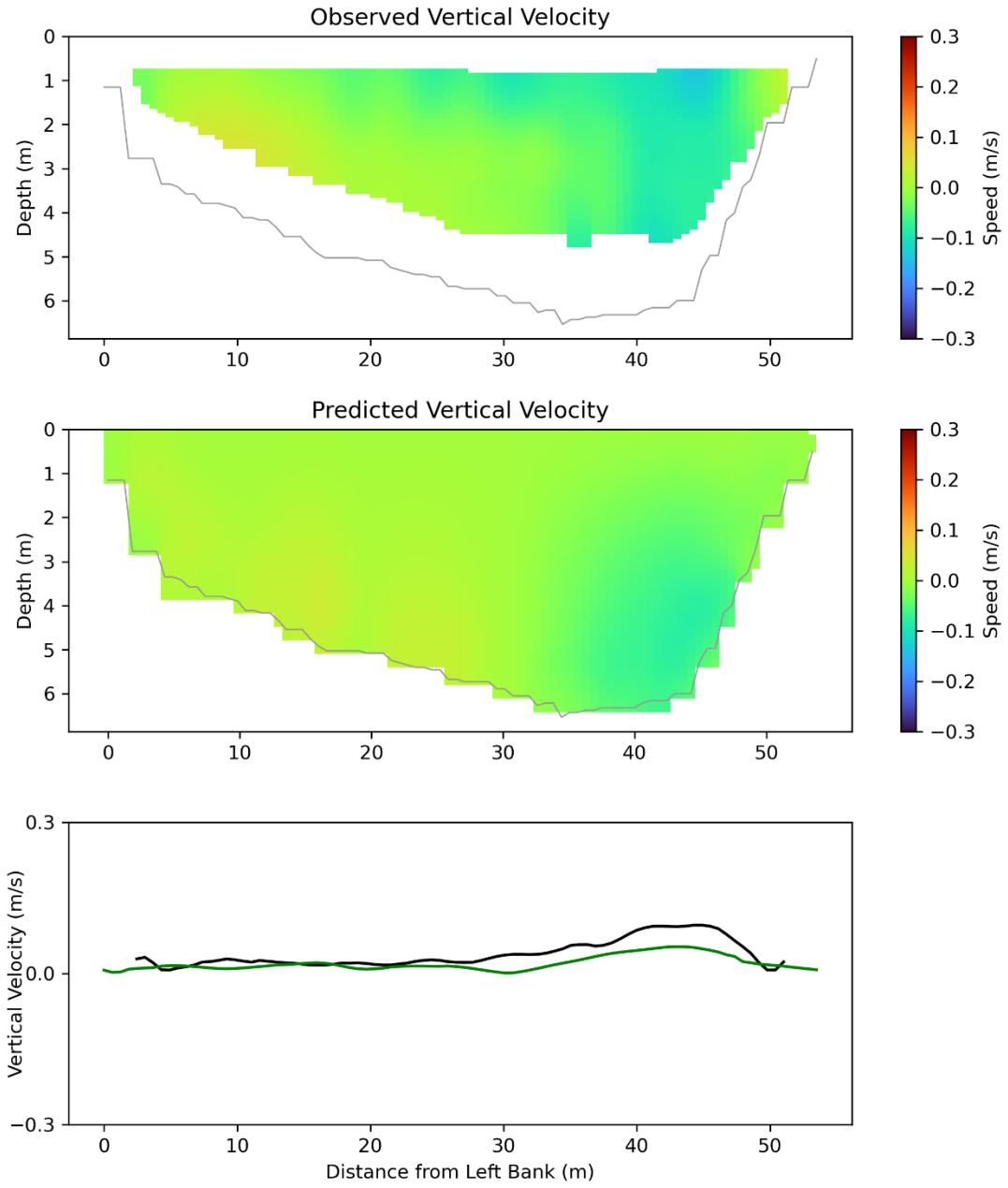

Figure 34 Vertical velocity at cross-section OR1.

Figure 34 shows observed (top panel) and predicted (middle panel) vertical velocity distributions and depth-averaged vertical velocity (bottom panel) at the identified cross section, plotted versus depth and distance from the left bank.

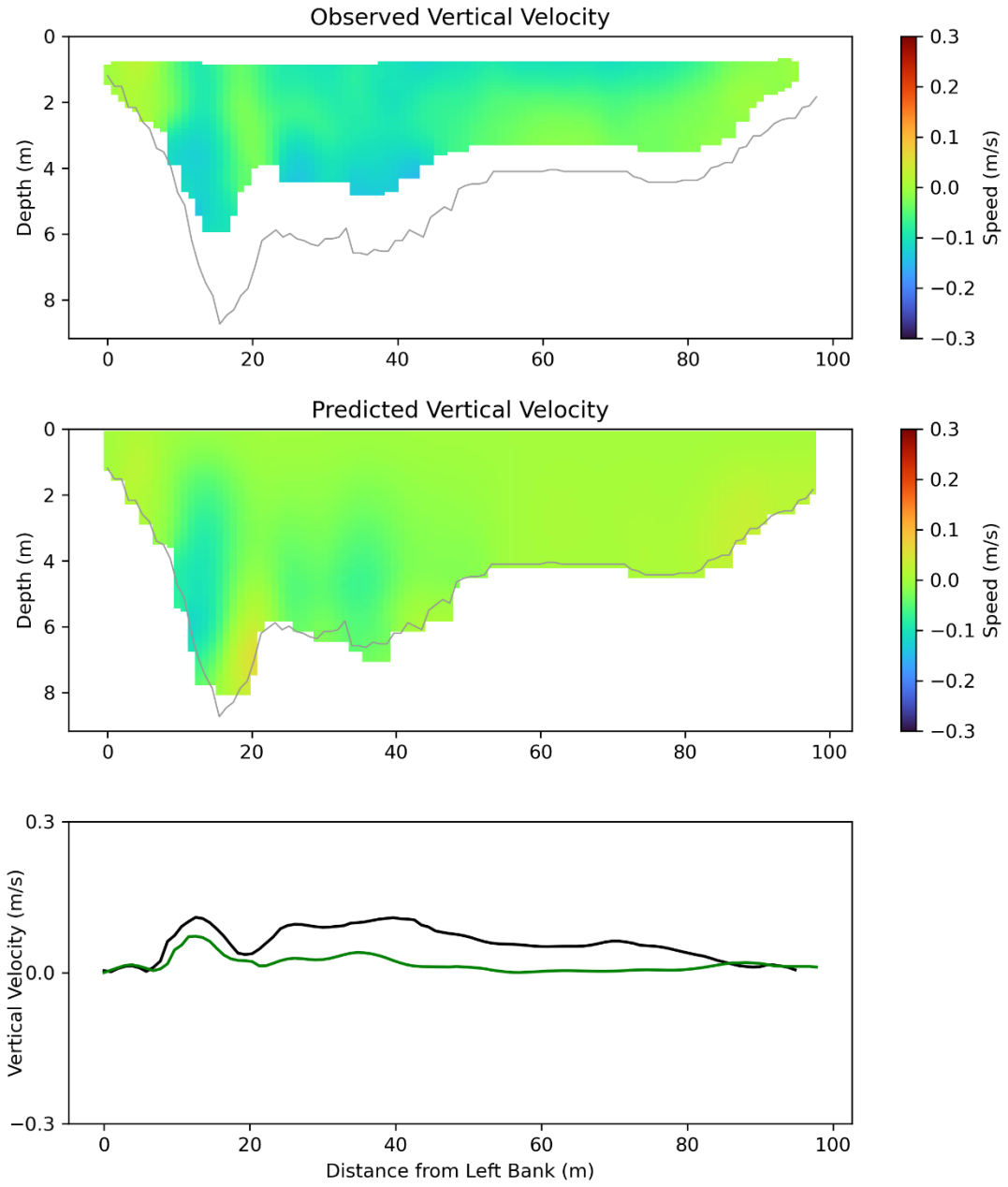

Figure 35 Vertical velocity at cross-section SJD1.

Figure 35 shows observed (top panel) and predicted (middle panel) vertical velocity distributions and depth-averaged vertical velocity (bottom panel) at the identified cross section, plotted versus depth and distance from the left bank.

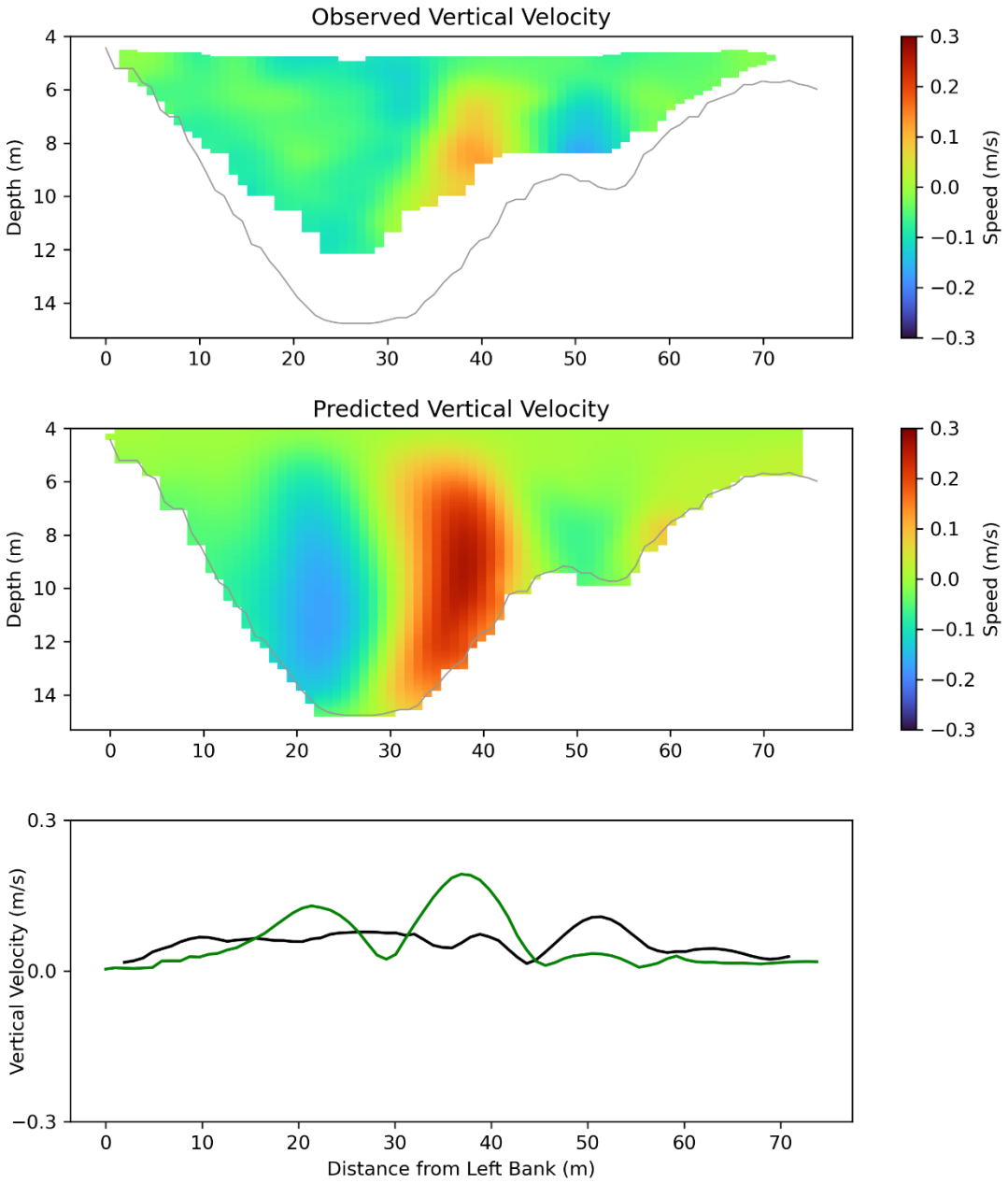

Figure 36 Vertical velocity at cross-section SJD2.

Figure 36 shows observed (top panel) and predicted (middle panel) vertical velocity distributions and depth-averaged vertical velocity (bottom panel) at the identified cross section, plotted versus depth and distance from the left bank.

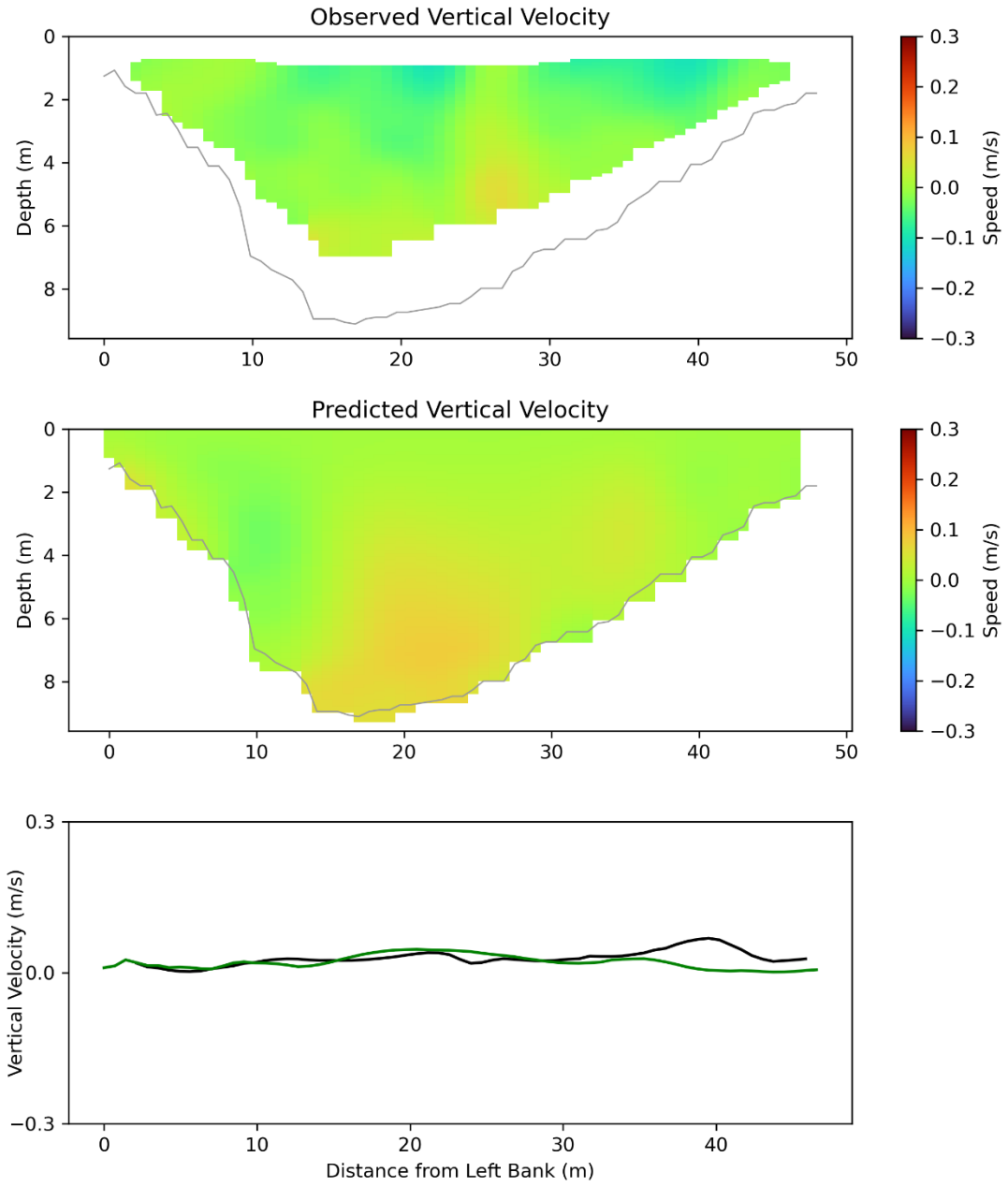

Figure 37 Vertical velocity at cross-section SJD3.

Figure 37 shows observed (top panel) and predicted (middle panel) vertical velocity distributions and depth-averaged vertical velocity (bottom panel) at the identified cross section, plotted versus depth and distance from the left bank.

Table 5 Vertical velocity metrics for the March 27, 2019 survey including coefficient of correlation (R).

Transect	Observed (m/s)	Predicted (m/s)	R	RMSD (m/s)	Skill
JCT	-0.050	0.001	0.303	0.061	0.454
OR1	-0.036	-0.010	0.633	0.044	0.678
SJD1	-0.067	-0.017	0.587	0.062	0.589
SJD2	-0.049	-0.005	0.576	0.097	0.664
SJD3	-0.020	0.018	0.306	0.056	0.518
SJU01	-0.030	-0.001	0.187	0.039	0.469
SJU02	-0.038	-0.005	0.001	0.053	0.398
SJU03	-0.039	-0.006	0.437	0.047	0.576
SJU04	-0.036	0.004	0.265	0.050	0.457
SJU05	-0.040	-0.001	-0.138	0.048	0.400
SJU06	-0.035	0.001	0.162	0.045	0.437
SJU07	-0.043	0.005	0.316	0.059	0.442

2022

Velocity data were collected at 8 cross-sections in the 2022 cbec field study (Figure 10). At each location in the cross-section where velocity was estimated from ADCP data, the predicted depth-averaged speed was compared to observed depth-averaged speed (Figure 38). The observed depth-averaged velocities in the 2022 study were much smaller than the observed depth-averaged velocities in the 2019 study. This was related both to the smaller net flows and the tidal phase of transect data collection in 2022 which spanned slack water (

Figure 6). In the survey, the data at SJU0, upstream of the junction, was collected late in a flood tide, while the transect at the junction (JCT) was collected around slack water and the downstream transects (SJD1 to SJD4) were collected during the following ebb tide. The depth-averaged speed distribution was generally predicted accurately by the model with a small negative bias (underestimated speed), an average skill of 0.690, and a maximum RMSD of 0.051 m/s (Table 6). The cross-sectional distribution of streamwise velocity was predicted accurately with average skill of 0.633 and RMSD of 0.060 m/s (Table 7). The metrics for distribution of secondary velocity were an average skill of 0.344 and RMSD of 0.045 m/s (Table 8).

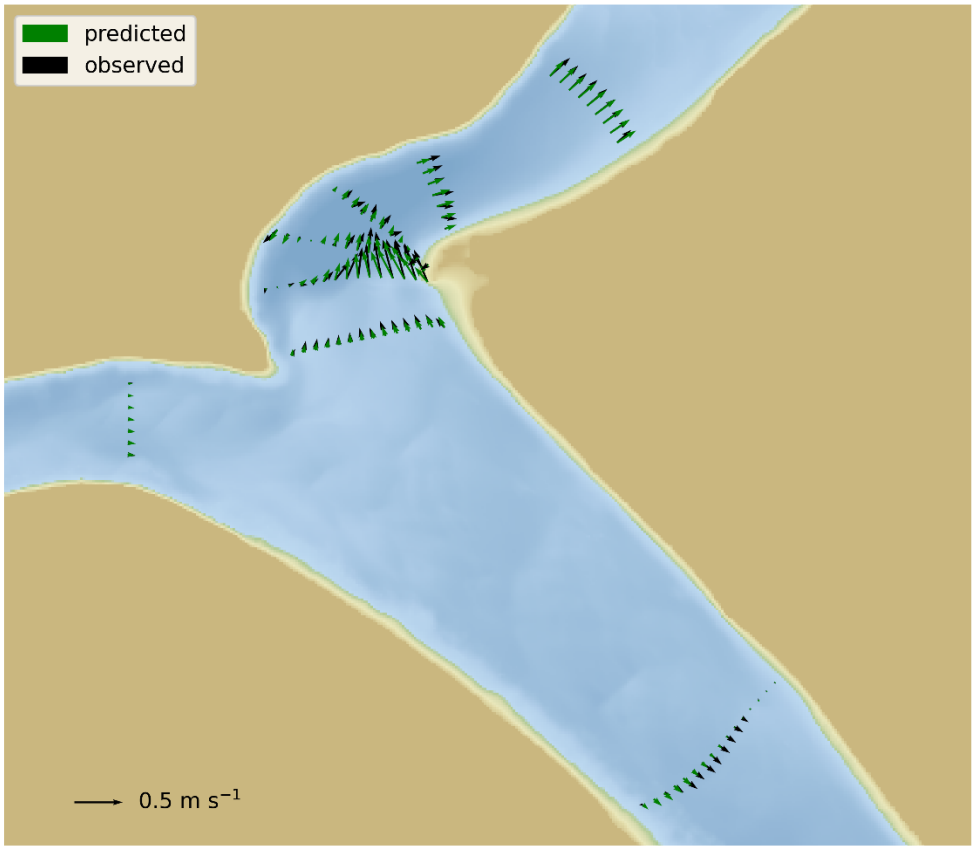

Figure 38 Depth-Averaged Velocities

Figure 38 shows observed (black) and predicted (green) depth-averaged velocity vectors at each cross-section on February 22, 2022.

Table 6 Difference metrics for depth-averaged speed for the February 22, 2022 survey

Transect	Observed (m/s)	Predicted (m/s)	Bias (m/s)	RMSD (m/s)	Skill
HOR0	0.065	0.069	0.004	0.013	0.745
JCT	0.135	0.102	-0.033	0.040	0.583
SJD0	0.239	0.185	-0.054	0.071	0.926
SJD1	0.163	0.142	-0.021	0.071	0.786
SJD2	0.125	0.100	-0.025	0.052	0.651
SJD3	0.178	0.165	-0.014	0.053	0.657
SJD4	0.248	0.234	-0.013	0.046	0.556
SJU0	0.091	0.063	-0.028	0.062	0.613

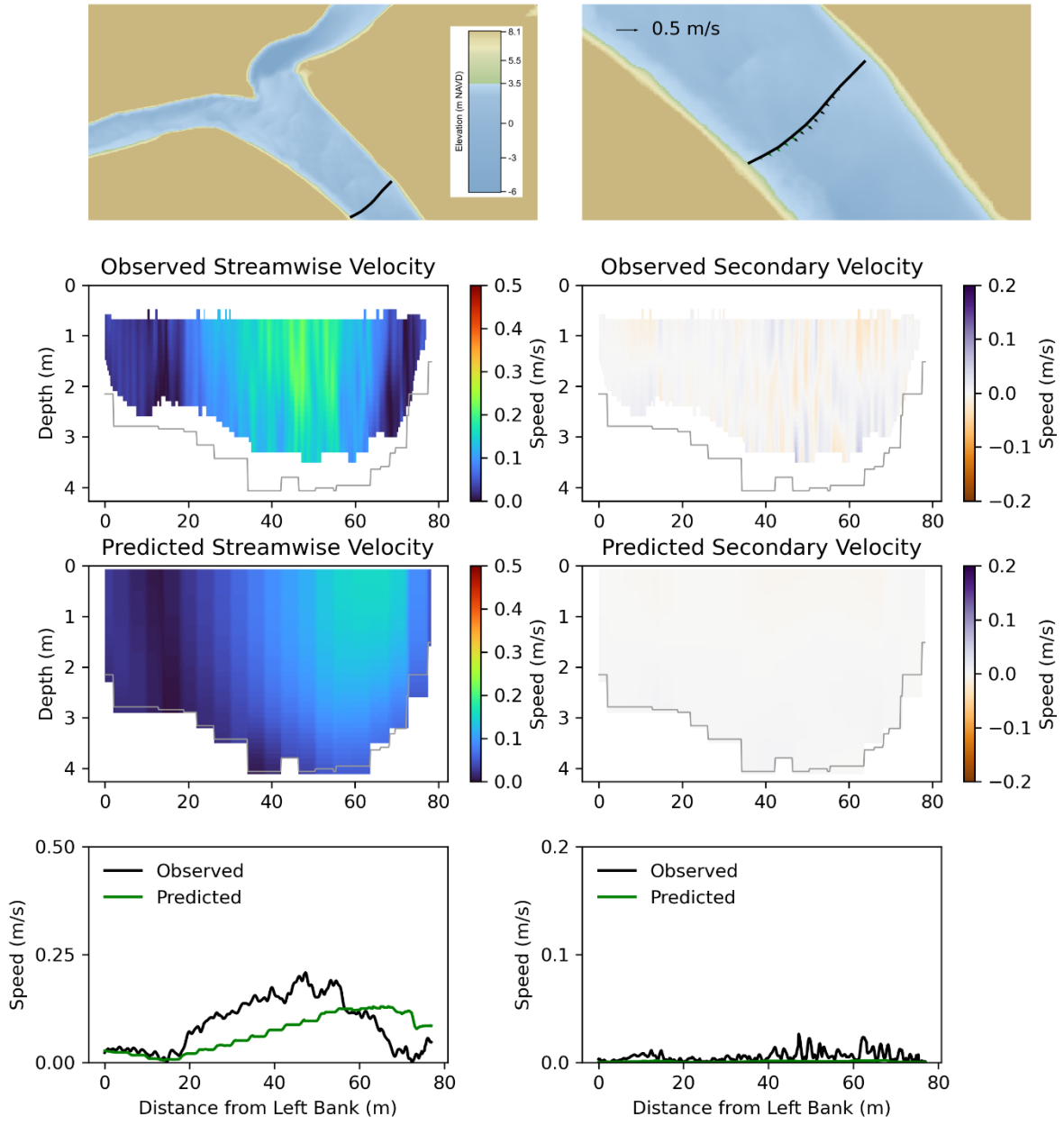

Figure 39 Streamwise and secondary velocity at cross-section SJU0.

Figure 39 depicts three charts. The top row shows the location of the cross section in the study area (left) and the observed and predicted depth-averaged velocity (right). The middle rows compare observed and predicted streamwise velocity distribution (left) and secondary (lateral) velocity information (right). The bottom row shows the magnitude (absolute value) of depth-averaged streamwise velocity (left) and secondary velocity (right).

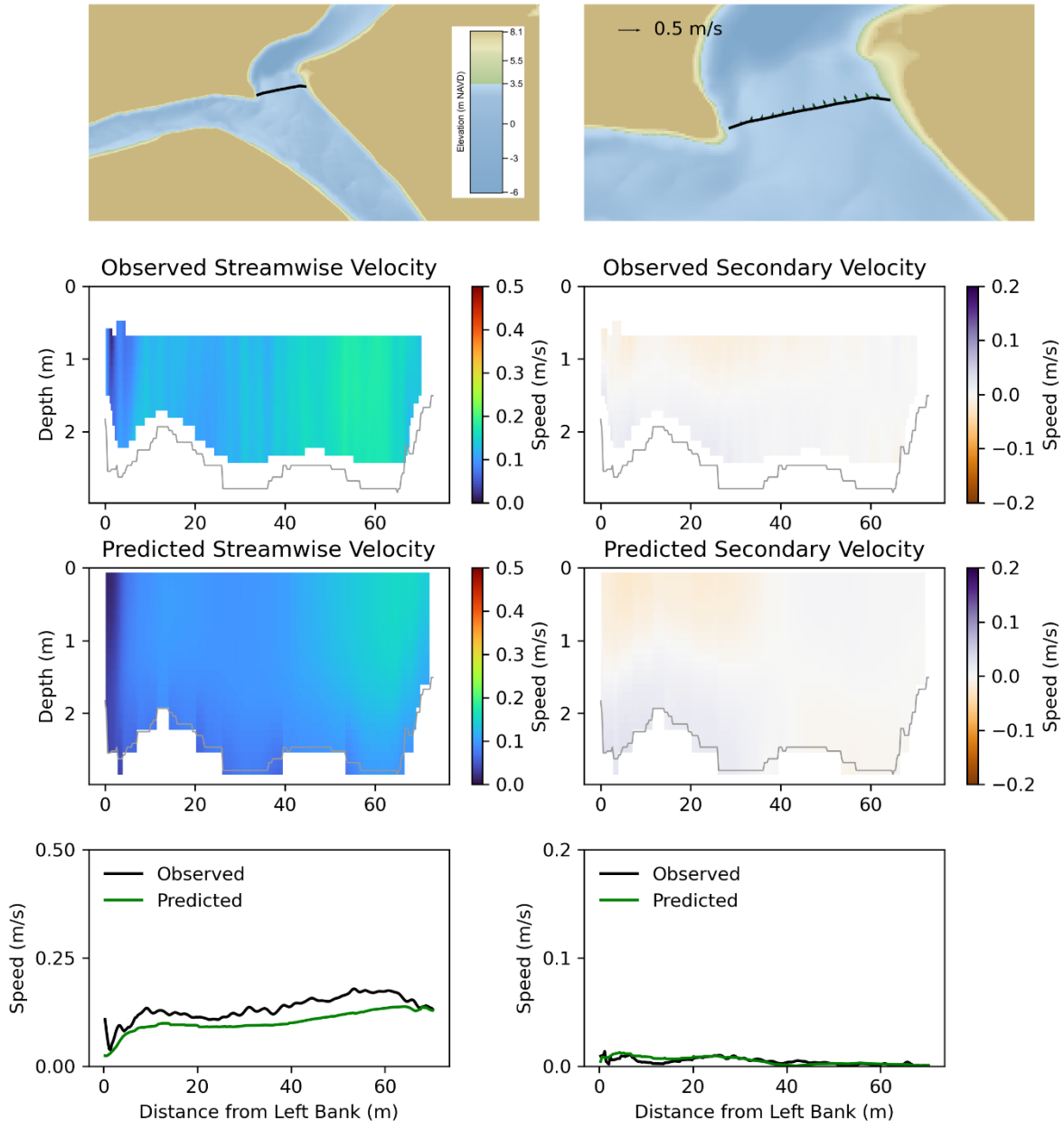

Figure 40 Streamwise and secondary velocity at cross-section JCT.

Figure 40 depicts three charts. The top row shows the location of the cross section in the study area (left) and the observed and predicted depth-averaged velocity (right). The middle rows compare observed and predicted streamwise velocity distribution (left) and secondary (lateral) velocity information (right). The bottom row shows the magnitude (absolute value) of depth-averaged streamwise velocity (left) and secondary velocity (right).

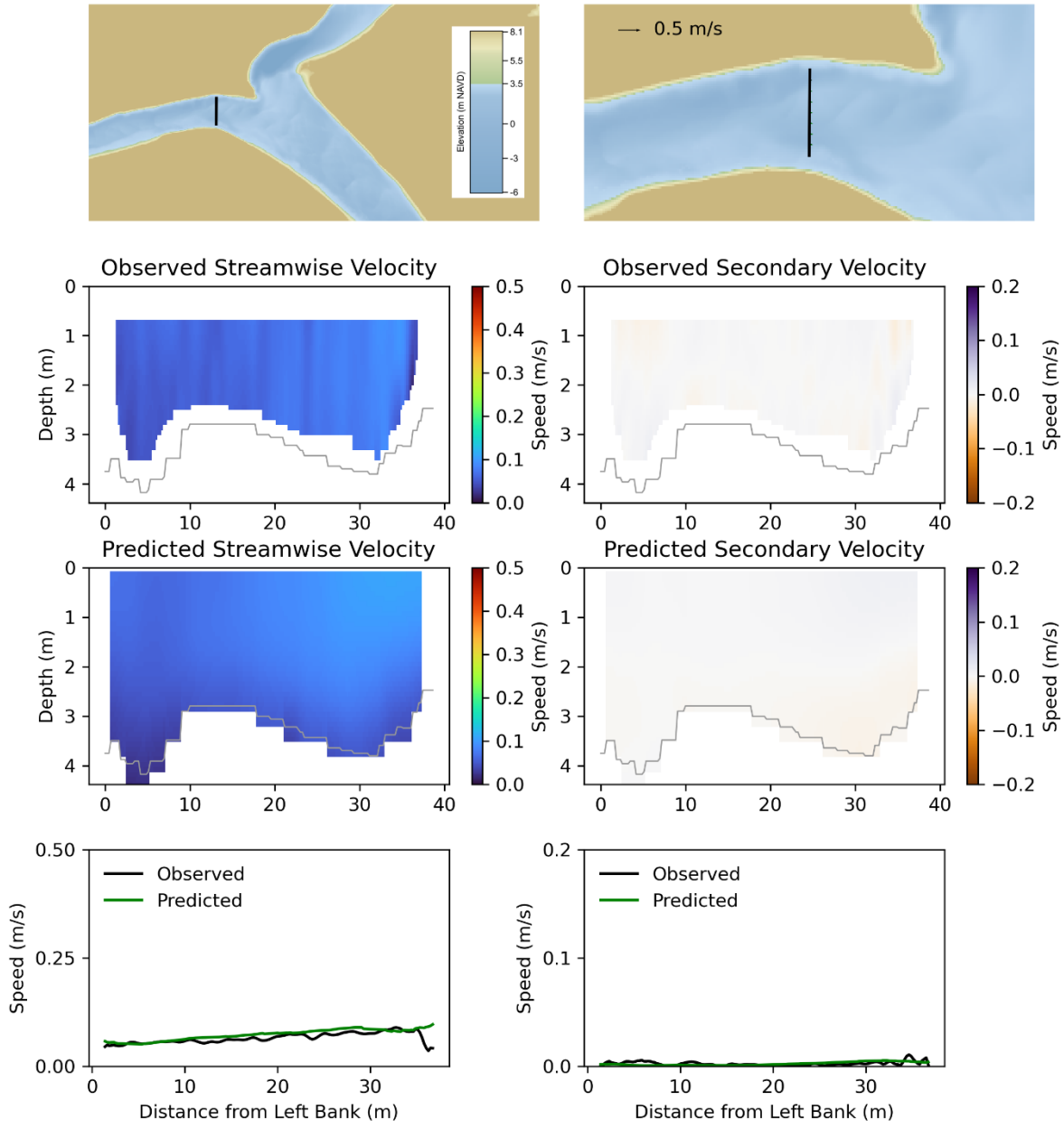

Figure 41 Streamwise and secondary velocity at cross-section HOR.

Figure 41 depicts three charts. The top row shows the location of the cross section in the study area (left) and the observed and predicted depth-averaged velocity (right). The middle rows compare observed and predicted streamwise velocity distribution (left) and secondary (lateral) velocity information (right). The bottom row shows the magnitude (absolute value) of depth-averaged streamwise velocity (left) and secondary velocity (right).

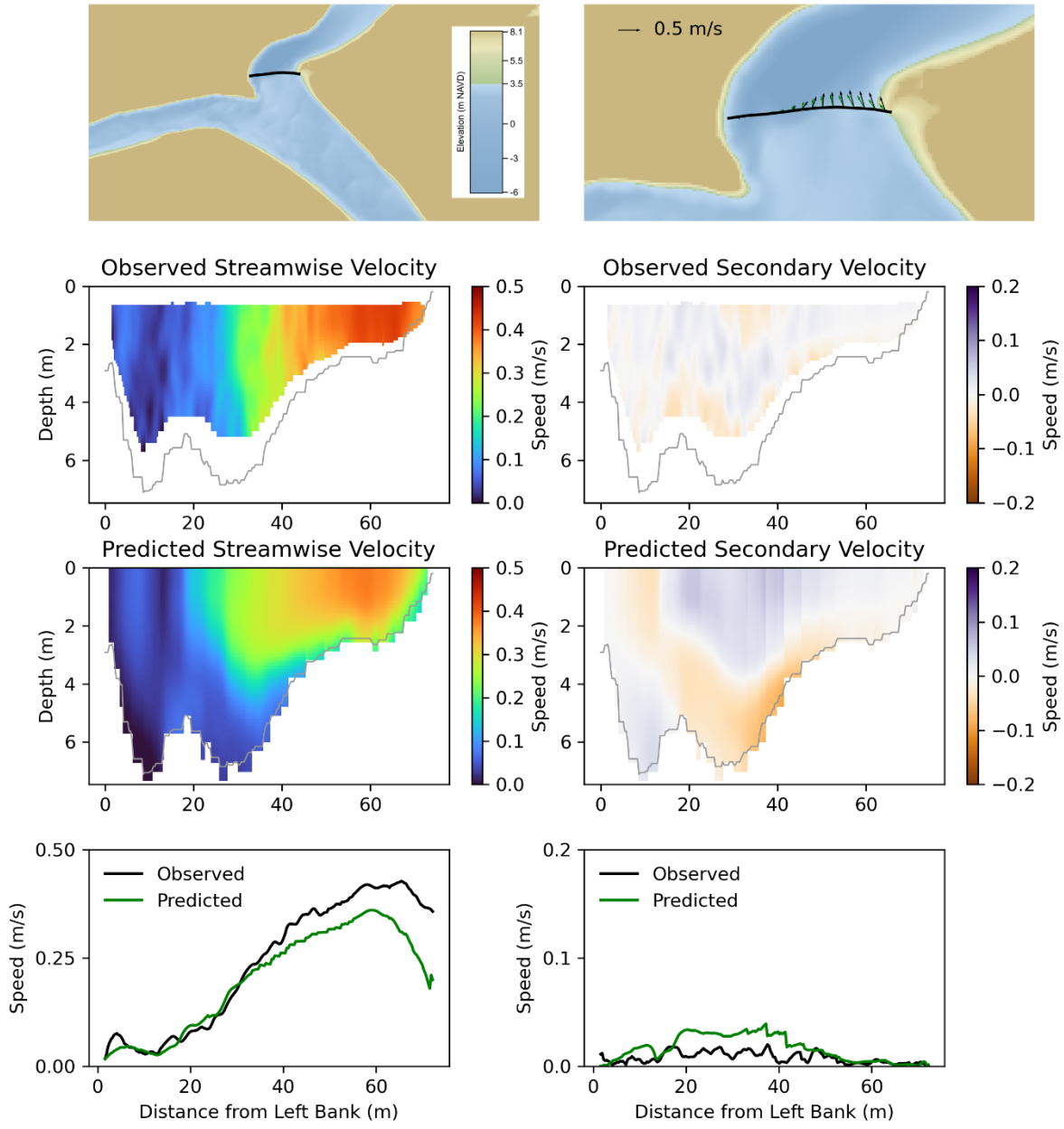

Figure 42 Streamwise and secondary velocity at cross-section SJD0.

Figure 42 depicts three charts. The top row shows the location of the cross section in the study area (left) and the observed and predicted depth-averaged velocity (right). The middle rows compare observed and predicted streamwise velocity distribution (left) and secondary (lateral) velocity information (right). The bottom row shows the magnitude (absolute value) of depth-averaged streamwise velocity (left) and secondary velocity (right).

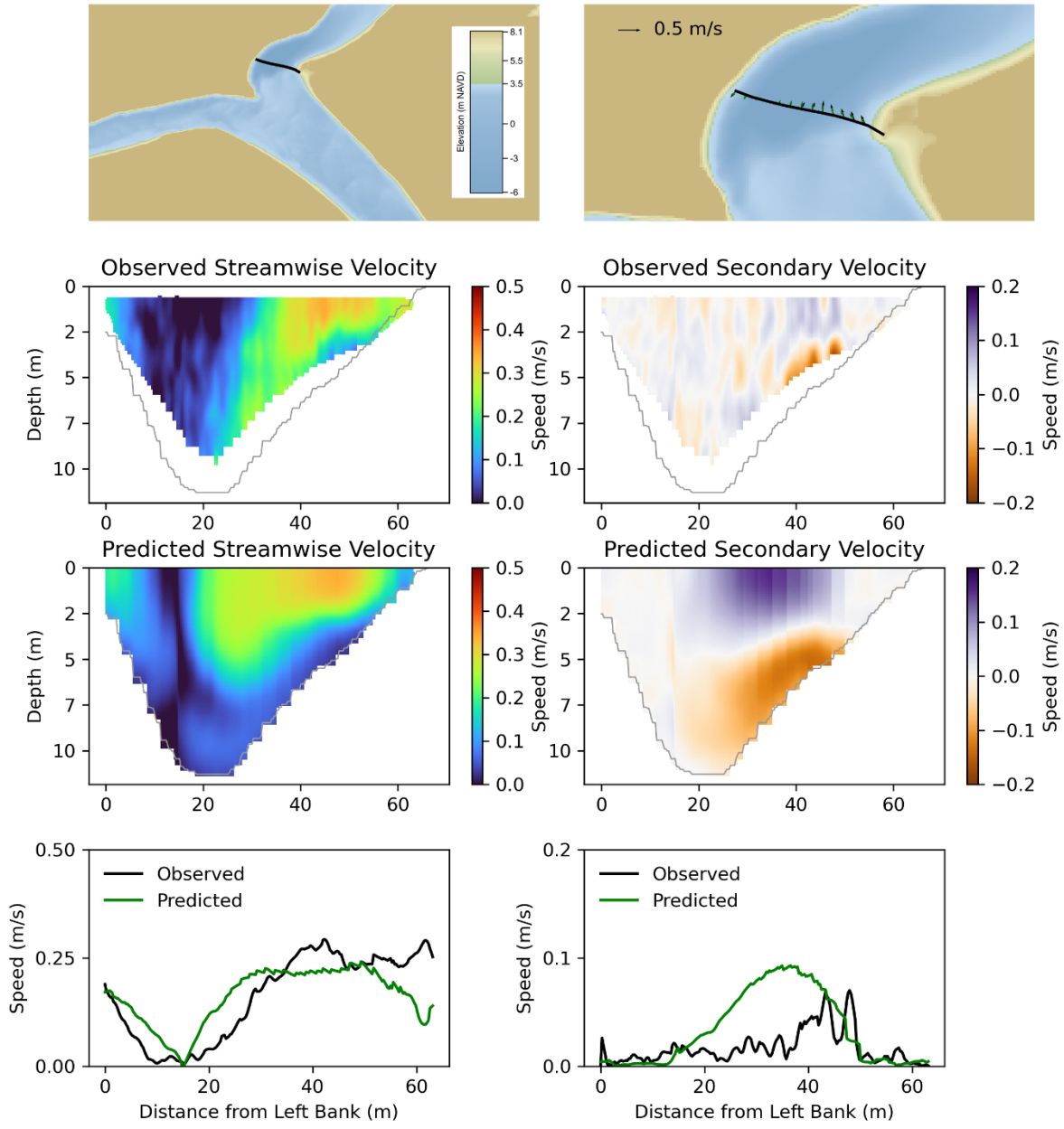

Figure 43 Streamwise and secondary velocity at cross-section SJD1.

Figure 43 depicts three charts. The top row shows the location of the cross section in the study area (left) and the observed and predicted depth-averaged velocity (right). The middle rows compare observed and predicted streamwise velocity distribution (left) and secondary (lateral) velocity information (right). The bottom row shows the magnitude (absolute value) of depth-averaged streamwise velocity (left) and secondary velocity (right).

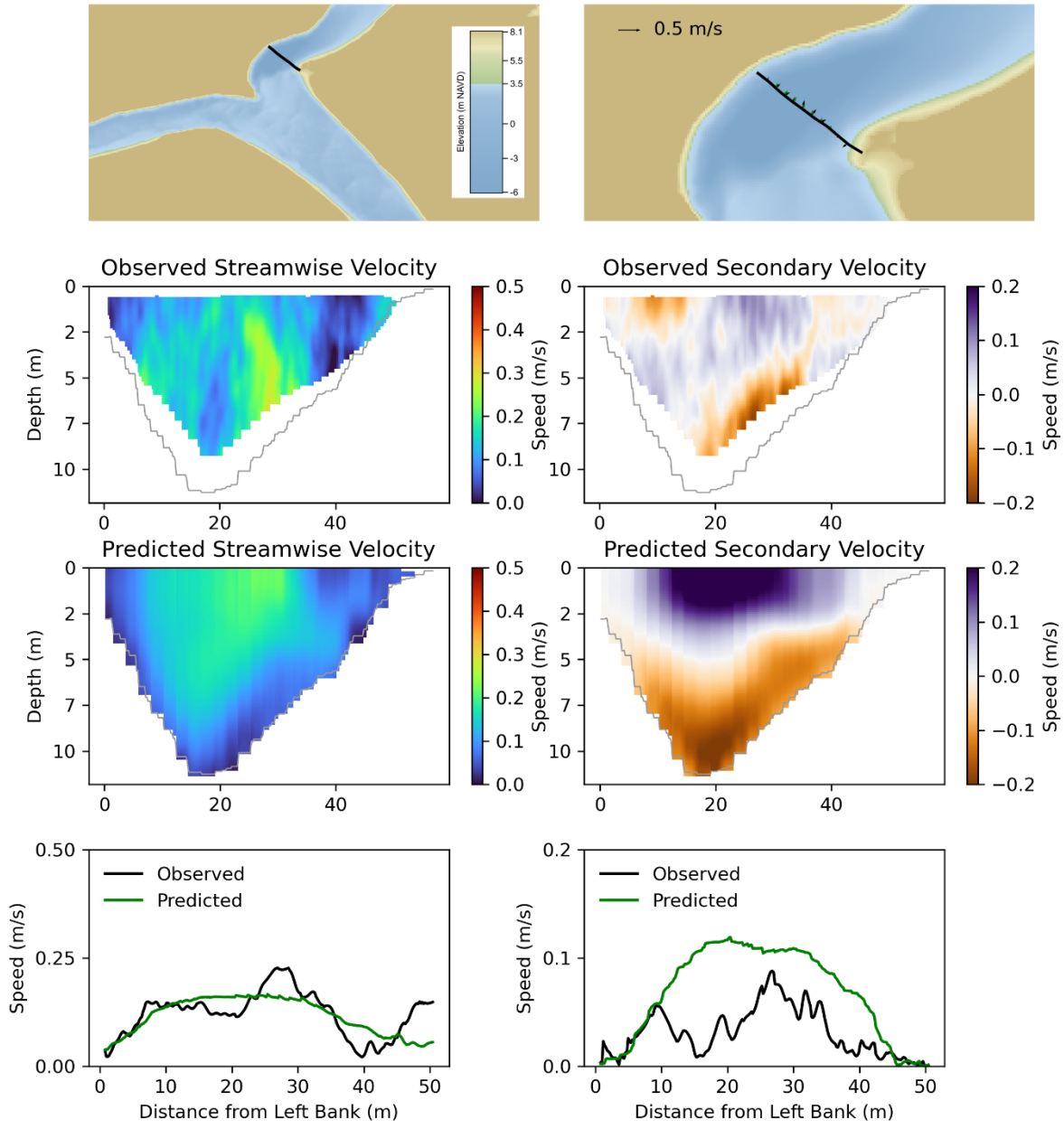

Figure 44 Streamwise and secondary velocity at cross-section SJD2.

Figure 44 depicts three charts. The top row shows the location of the cross section in the study area (left) and the observed and predicted depth-averaged velocity (right). The middle rows compare observed and predicted streamwise velocity distribution (left) and secondary (lateral) velocity information (right). The bottom row shows the magnitude (absolute value) of depth-averaged streamwise velocity (left) and secondary velocity (right).

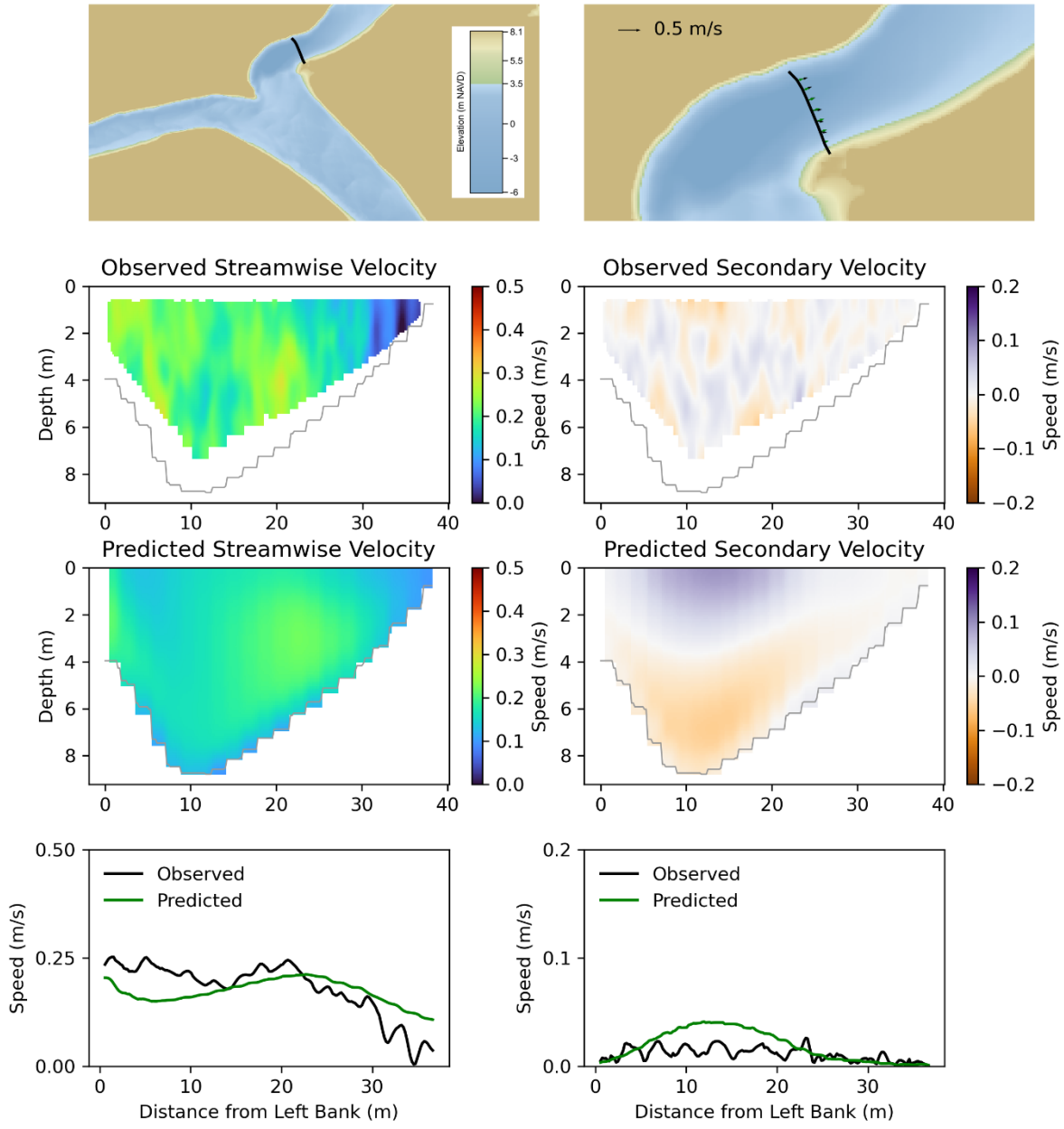

Figure 45 Streamwise and secondary velocity at cross-section SJD3.

Figure 45 depicts three charts. The top row shows the location of the cross section in the study area (left) and the observed and predicted depth-averaged velocity (right). The middle rows compare observed and predicted streamwise velocity distribution (left) and secondary (lateral) velocity information (right). The bottom row shows the magnitude (absolute value) of depth-averaged streamwise velocity (left) and secondary velocity (right).

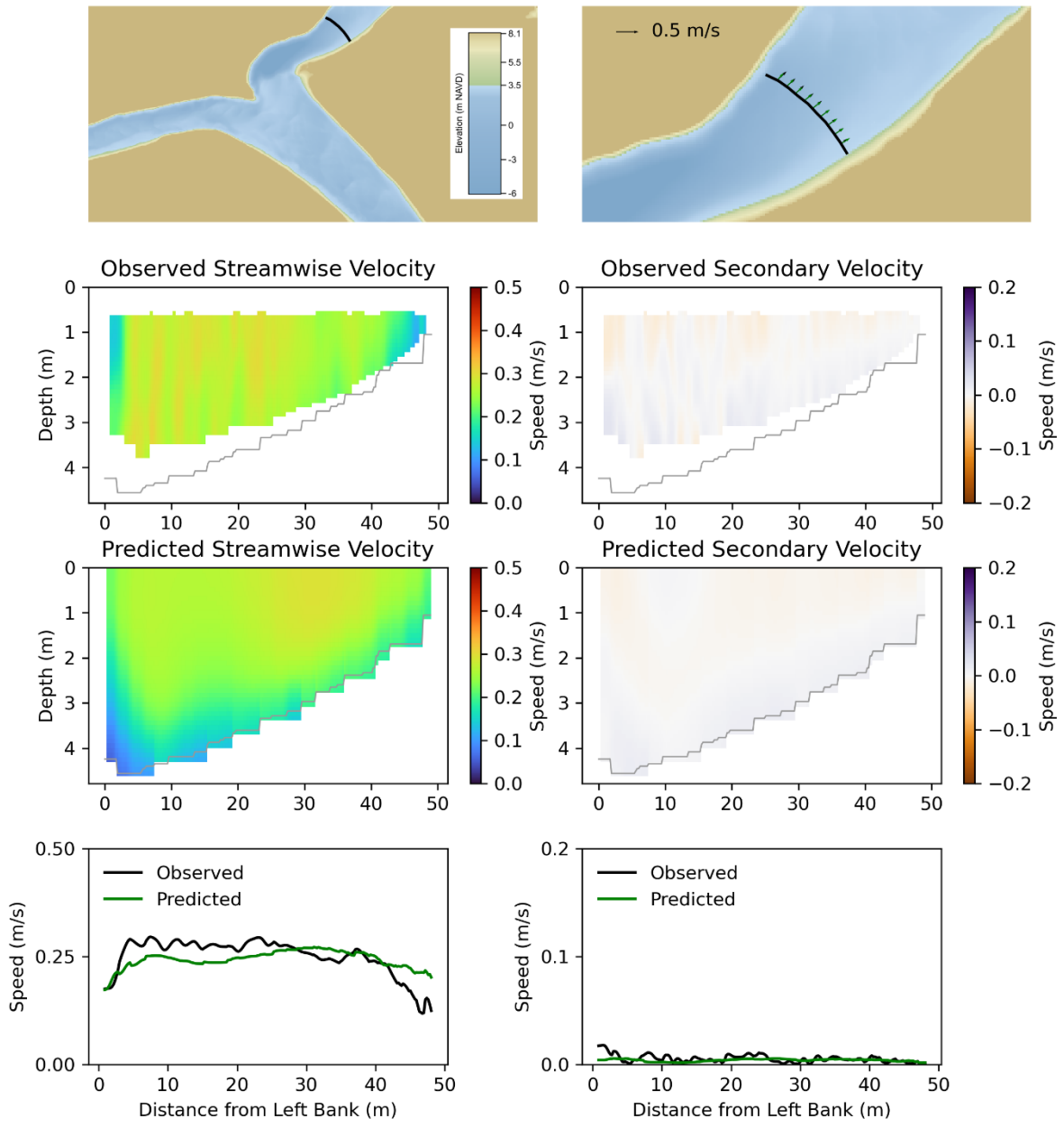

Figure 46 Streamwise and secondary velocity at cross-section SJD4.

Figure 46 depicts three charts. The top row shows the location of the cross section in the study area (left) and the observed and predicted depth-averaged velocity (right). The middle rows compare observed and predicted streamwise velocity distribution (left) and secondary (lateral) velocity information (right). The bottom row shows the magnitude (absolute value) of depth-averaged streamwise velocity (left) and secondary velocity (right).

Table 7 Difference metrics for streamwise velocity for the February 22, 2022 survey.

Transect	Observed (m/s)	Predicted (m/s)	Bias (m/s)	RMSD (m/s)	Skill
HOR0	0.066	0.073	0.007	0.023	0.605
JCT	0.137	0.106	-0.032	0.041	0.603
SJD0	0.182	0.163	-0.019	0.068	0.929
SJD1	0.130	0.153	0.023	0.103	0.735
SJD2	0.133	0.134	0.001	0.068	0.543
SJD3	0.196	0.177	-0.018	0.060	0.498
SJD4	0.259	0.245	-0.014	0.049	0.562
SJU0	0.102	0.074	-0.028	0.070	0.590

Table 8 Difference metrics for secondary velocity for the February 22, 2022 survey.

Transect	Observed (m/s)	Predicted (m/s)	Bias (m/s)	RMSD (m/s)	Skill
HOR0	0.066	0.073	0.007	0.023	0.605
JCT	0.137	0.106	-0.032	0.041	0.603
SJD0	0.182	0.163	-0.019	0.068	0.929
SJD1	0.130	0.153	0.023	0.103	0.735
SJD2	0.133	0.134	0.001	0.068	0.543
SJD3	0.196	0.177	-0.018	0.060	0.498
SJD4	0.259	0.245	-0.014	0.049	0.562
SJU0	0.102	0.074	-0.028	0.070	0.590

In addition to the transect data, a moored ADCP data was deployed in the scour hole (Figure 10) from February 8, 2022 to February 23, 2022. This period generally had low San Joaquin River flows (Figure 7). Several differences were notable between the predicted and observed velocities in Figure 47. The maximum observed streamwise velocity was located lower in the water column than in predicted streamwise velocity, which was more vertically uniform. The predicted secondary circulation was also much stronger than was observed. We note that conditions in the scour hole were challenging for both numerical modeling and ADCP measurements. Unlike the transect data, for which noise can be reduced by averaging across similar but distinct repeated transects, the mooring data is a time series at a single point. In most moored ADCP measurements the assumption of horizontal homogeneity at the scale of the beam spread is well justified. Given the dynamic conditions in the scour hole, including strong vertical velocities with relatively sharp gradients, we cannot rule out the possibility of contamination of the velocity signal. Quality assurance data from the ADCP processing suggests that heterogeneity was substantial (error velocity was often above typical thresholds), though the magnitude of the effects on persistent velocity features is unclear.

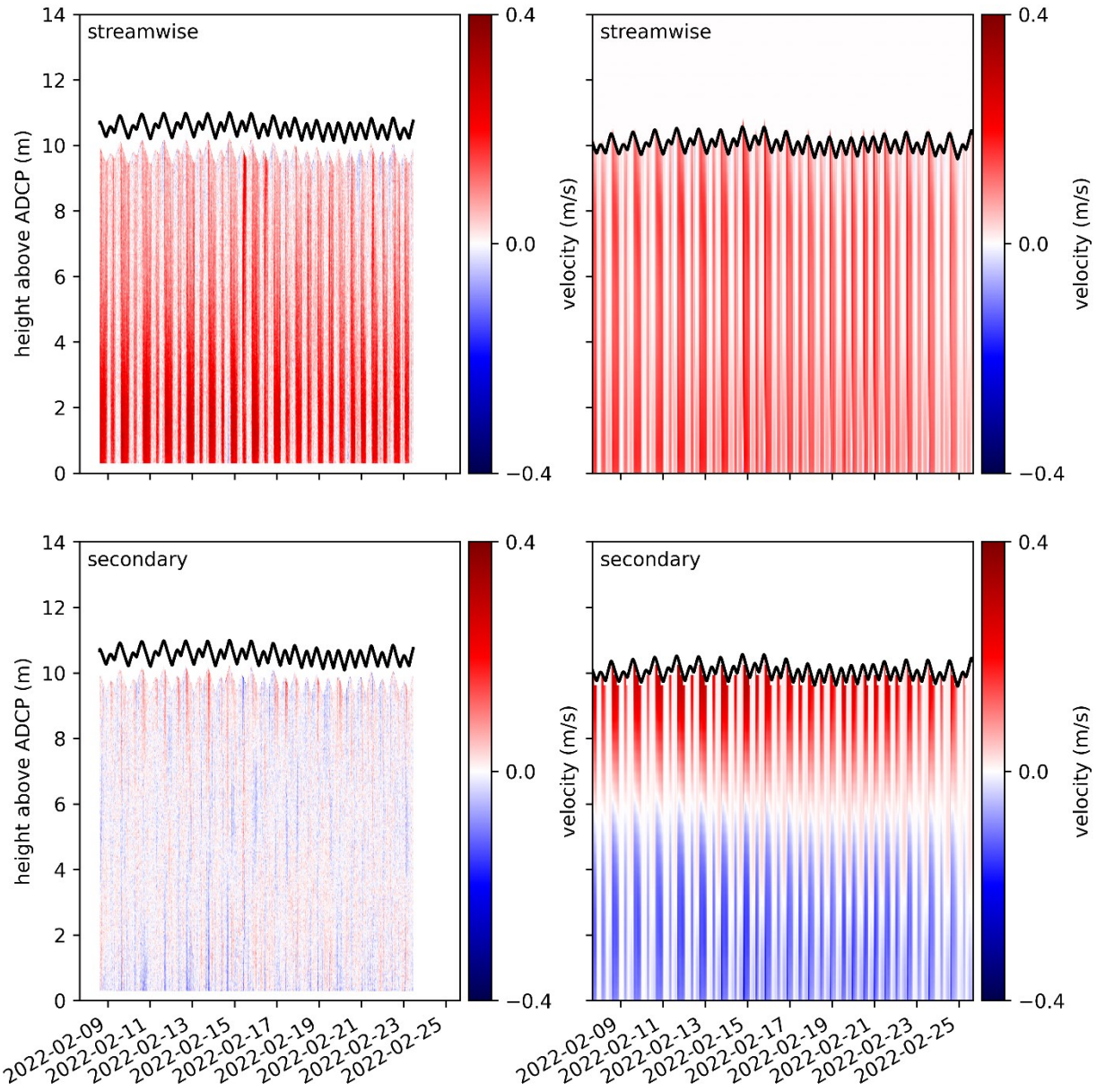

Figure 47 2022 Mooring Streamwise Velocity

Figure 47 shows observed (left) and predicted (right) streamwise velocity (top panels) and secondary velocity (bottom panels) for the 2022 mooring, plotted as velocity versus height above the ADCP over time.

DISCUSSION

The model calibration indicated that the model reproduced several aspects of the observed flow. The depth-averaged velocity distributions were predicted well. The streamwise velocity distribution in cross-sections was generally predicted accurately. Patterns of secondary circulation were generally predicted well but the magnitude of this circulation was overestimated near the scour hole. Patterns of predicted vertical velocity were similar to

observed patterns but generally greater in magnitude in cross-sections with significant vertical velocities. The 2019 calibration period had much higher flows than the 2022 calibration period and performance metrics were generally better in 2019 than 2022. The high flow conditions of 2019 have more relevance to potential scour in the study area.

There are several limitations to the calibration. One is that none of the calibration data extended down to the bed, thus the ability of the model to predict bed shear stress was not directly evaluated. However, generally accurate prediction of velocity distribution over the extent of available data does provide some confidence in predicted bed shear stress. The generally poorer comparison to the moored ADCP data than the ADCP transects is not well understood. This low flow period of 2022 is generally of less relevance to potential scour than the higher flow conditions of 2019. However, it is possible that none of the calibration data was collected during a high enough flow to cause scour. To the extent that comparison to moored ADCP data points to underpredicted velocity near the bed of the scour hole, the predicted bed shear stress would also be underestimated in these regions.

THREE-DIMENSIONAL HYDRODYNAMIC MODEL APPLICATION: OPTION 1

This section summarizes the application of the three-dimensional hydrodynamic model to evaluate effects of filling in the scour hole adjacent to the Head of Old River ("Option 1"). In this phase the 3D modeling was selectively applied to analyze effects on bed stress and 3D circulation. These results complement an analysis of all initial options alternatives in the two-dimensional model.

One potential concern in the design process is whether a particular option will be morphodynamically stable over the long term. Bed stress is the primary predictor of whether a particular substrate will remain in place or be scoured away. Unusually strong vertical velocities can also contribute to sediment mobility, through direct action on bed particles and by compressing the bottom boundary layer. An increase in bed stress due to a compressed bottom boundary layer may occur at scales that are not well-resolved in the 3D model, so we included vertical velocity as a secondary indicator of scour potential.

BASE CONDITIONS AND OPTION 1

Three-dimensional hydrodynamic modeling in this phase was limited to base conditions and the Option 1 alternative. This alternative involved filling in the scour hole with coarse material in order to reduce secondary and vertical circulation, which are hypothesized to exacerbate salmon predation. The 3D hydrodynamic model has been designed to capture these circulation patterns as well as the local distribution of bed stress associated with formation and maintenance of the scour hole. However, the model is computationally intensive and

impractical for large-scale simulations. Assessment of flood risks from this and other alternatives are discussed separately, supported by estuary-scale two-dimensional modeling.

In this initial phase, there were three goals of the 3D hydrodynamic analysis. The first goal this phase was to confirm that Option1, filling in the hole, substantially reduces secondary and vertical circulation. The second goal was to confirm that 3D processes do not substantially alter flood stage predictions, such that 2D results for stage are sufficient for evaluating flood conditions. Lastly, there was the question of the fill itself: what size fill is needed in order to avoid scour, and how sensitive are hydrodynamic results to the size of the fill.

HYDRODYNAMIC MODEL

In this section we describe the specifics of the model configuration as applied to initial analysis of Option 1. A full description of the 3D hydrodynamic model is included in the calibration section.

The model was run with two configurations:

- Base conditions, representing the current state of the scour hole, and
- Option 1, filling in the scour hole.

BASE CONDITIONS

The Base conditions utilized a cbec-produced DEM based on DWR's 2019 multibeam survey of scour hole and 2017 Delta LiDaR DEM. Bed roughness in the model was configured via a spatially variable z_0 as in the model calibration. Selection of z_0 was based on inspection of an earlier multibeam dataset (July 2017), from which roughness length scales were extracted. A substrate map was also created from this dataset, classifying the bed as sand, sand with bedforms, and cobble/riprap. Each substrate classification was assigned a roughness: sand (0.002 m), sand with bedforms (0.003 m), and cobble (0.008 m) (Figure 8). The distribution of roughness was kept constant across simulation periods.

Simulations were forced with an estimated 100-year flood, based on the 2009 FEMA Flood Insurance Study for San Joaquin County. Flood conditions included flow in the San Joaquin River of 43,500 cfs at Mossdale, an even flow split at the Old River-San Joaquin River diffluence, and stage of 24.8 ft at the Head of Old River. Tidal influence, which is minimal at high flows, was not included in the simulations. Simulations were run to steady state.

OPTION 1 CONFIGURATION

The Option 1 configuration was identical to the Base conditions setup except for bathymetry and roughness in the scour hole. Bathymetry in the scour hole was replaced with a surface that approximately matches the upstream and downstream bed elevations (Figure 48). Multiple choices of roughness in the scour hole were tested. A nominal roughness of z_0=0.006 m was

chosen for Base-Option 1 comparisons, approximating fill with D_{90}=180mm (Figure 49). Roughness values less than and greater than this were also tested in order to quantify sensitivity of the results to fill characteristics.

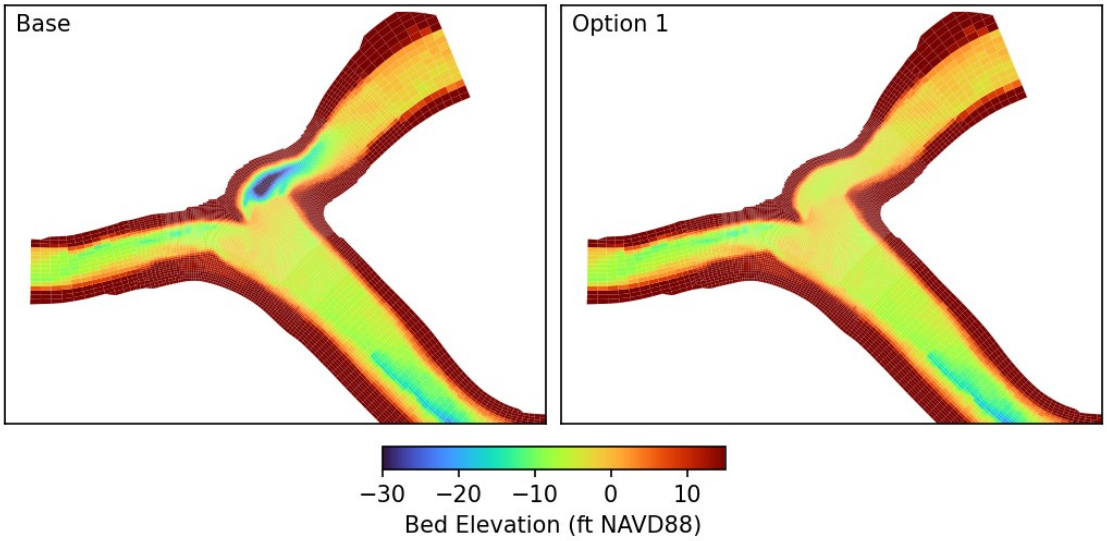

Figure 48 Bathymetry on Model Grid.

Figure 48 shows bathymetry on the model grid for Base (left panel) and Option 1 (right panel) conditions, plotted as bed elevation (ft NAVD88).

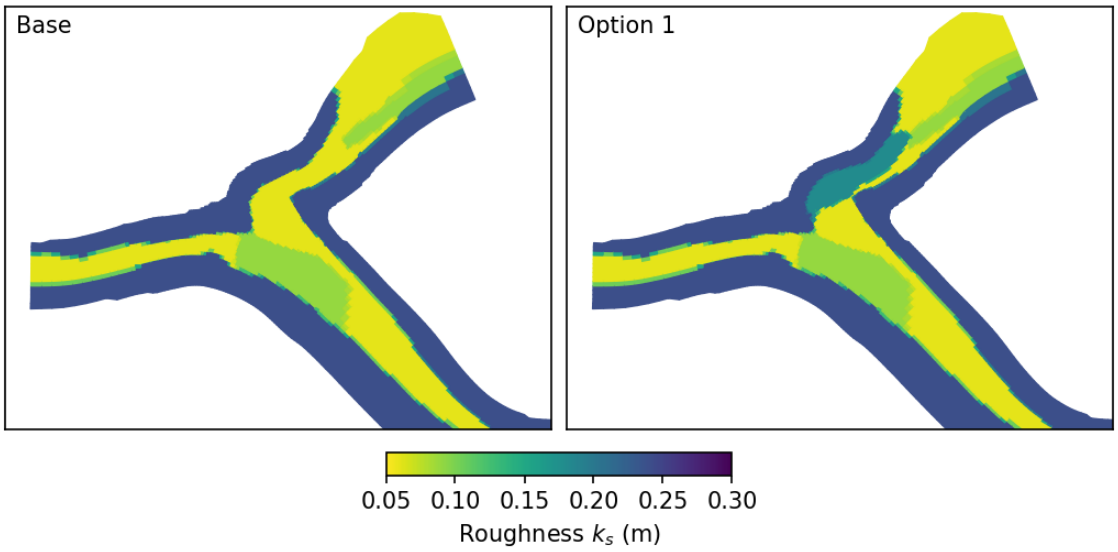

Figure 49 Roughness length scales

Figure 49 shows roughness length scales for (left) Base and (right) Option 1 conditions, scaled as approximate D_90 length scales (30·z_0). Dark regions along the banks correspond to cobble/riprap. Areas classified as sand without bedforms are yellow, with the light green areas classified as sand with bedforms. Nominal roughness for the scour hole fill of 0.180 m is visible as dark green in Option 1.

METRICS

BED STRESS

Bed shear stress is the force, distributed across the bed, exerted on the near-bed flow. Bed stress depends on the local frictional characteristics of the bed (the roughness length scale z_0), and the near-bed velocity. The 3D model incorporates this force both as a drag term when calculating the near bed velocity and as a driver of turbulence which in turn affects the distribution of velocity throughout the water column.

Bed shear stress can also be thought of as the distributed force exerted on the bed by the flow. In this sense, it is also a measure of scour potential. When the force of the flow on a particle in the bed is sufficient the particle will begin to move with the flow, initially tumbling along the bed as bedload. The edge-normal component of bed stress is calculated as

$$\tau_{edge} = C_D u_{norm} \sqrt{u_{norm}^2 + u_{tan}^2}$$

where u_{norm} is the edge-normal velocity in the deepest wet edge and u_{tan} is defined as the average of the edge-tangent component of cell-centered velocity from the two adjacent cells, in the same layer as the edge. Edge-normal stresses are interpolated to cell center stress vectors using the interpolation scheme of Perot (2000). Bathymetric variation introduces some small-scale "noise" into the calculated distribution of bed stress. In order to make interpretation more robust cell-centered bed stress values are further smoothed with a median filter, applied to each cell and its adjacent cells.

DEPTH-AVERAGED VELOCITY

Both horizontal and vertical velocities were reported as depth-averaged quantities. The underlying hydrodynamic model uses z-layers to discretize the vertical coordinate, and, in the present configuration, layer thicknesses were evenly distributed. The bed elevation was quantized to predetermined layer elevations (i.e. stair-stepped), but the free surface cells have a variable thickness that was some fraction of the thickness of underlying layers. When calculating depth-averaged quantities this difference in thickness was accounted for by computing a weighted average of layer values with weights based on the instantaneous layer thicknesses. For vertical velocities, the interface-centered values were first averaged to layer-centered values, and then depth-averaged according to layer thicknesses.

RESULTS

WATER SURFACE ELEVATION

Figure 50 shows the water surface elevation (WSE) around the Head of Old River in the Base Conditions and Option 1 simulations, with the difference shown in the right panel. Due to the proximity and configuration of the boundary conditions, in particular the stage boundary

condition on Old River, the model necessarily predicted minimal change in WSE on Old River and upstream of the junction. Immediately at the junction and extending over the scour hole Option 1 raised the WSE approximately 0.06 ft. This quickly transitioned to a lowering of the WSE downstream of the scour hole. These results were consistent with 2D modeling, and bolster the use of 2D modeling for analysis of flood risk associated with Option 1.

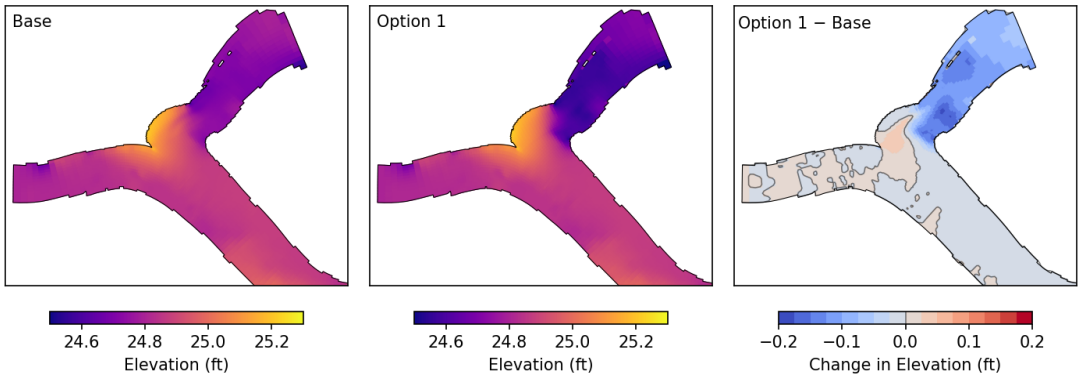

Figure 50 Water surface elevation and relative change for Base and Option 1 conditions. Option 1 results are based on fill with nominal D_{90}=180mm.

Figure 51 shows depth-averaged horizontal velocity for the Base and Option 1 conditions, with the difference plotted in the right panel. Velocities over the scour hole were increased in Option 1, consistent with the flow being distributed over a shallower water column. This effect extended beyond the region of the fill due to advection of high momentum coming out of the scour hole area.

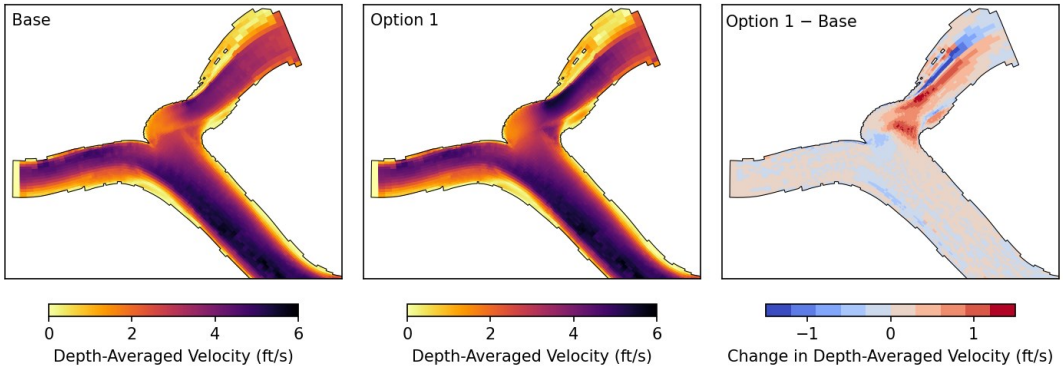

Figure 51 Depth-averaged speed and effect of Option 1. Option 1 results are based on fill with nominal D_{90}=180mm.

Figure 52 shows the distribution of vertical velocity in the Base and Option 1 conditions. Filling the scour hole had the anticipated effect of greatly reducing vertical velocities. Note that while the left and center panels include the sign of the vertical velocity (brown: downwelling, purple: upwelling), the change in vertical velocity (righthand panel) is shown as a change in magnitude (blue: attenuation, red: amplification).

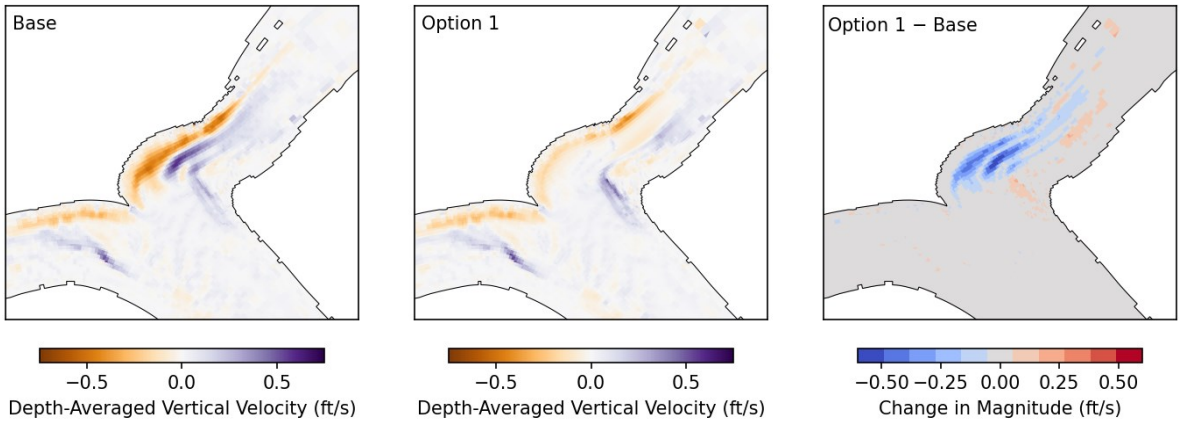

Figure 52 Depth-averaged vertical velocity during simulated 100-year flood conditions. Changes in vertical velocity (right panel) are shown as change in magnitude, with blue indicating attenuation of vertical velocity and red indicating amplification of vertical velocity.

Figure 53 compares distributions of vertical velocity between the Base and Option 1 conditions. Option 1 substantially decreased the occurrence of vertical velocities between 0.1 ft/s and 0.5 ft/s. This further confirmed that vertical velocities are reduced in Option 1 and not simply relocated to other locations around the junction. A slice view of vertical velocity is shown in Figure 54. This view provides additional insights into the drivers of downwelling currents and the effect of filling the scour hole. In the Base conditions simulation, upstream flow crossed over the scour hole and impinged on the NW bank of the scour hole. The sharp bend caused a "pile-up" of water here, and the additional dynamic pressure associated with the fast-moving surface layer driving downwelling circulation. These dynamics were still present to some degree in Option 1, with two significant differences. Firstly, downwelling flows quickly encountered the shallower bed, limiting vertical acceleration. Secondly, flow over the scour hole was more frictional due to proximity to the filled-in bed, leading to less dynamic pressure on the NW bank.

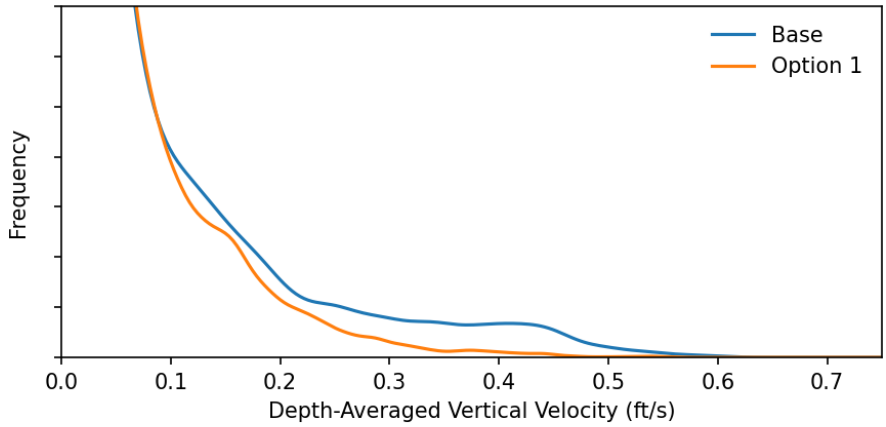

Figure 53 Distribution of absolute value of depth-averaged vertical velocity during 100-year flood conditions. Distributions are extracted over the region shown in Figure 52, and plotted as a kernel density estimate with bandwidth determined by Scott's rule.

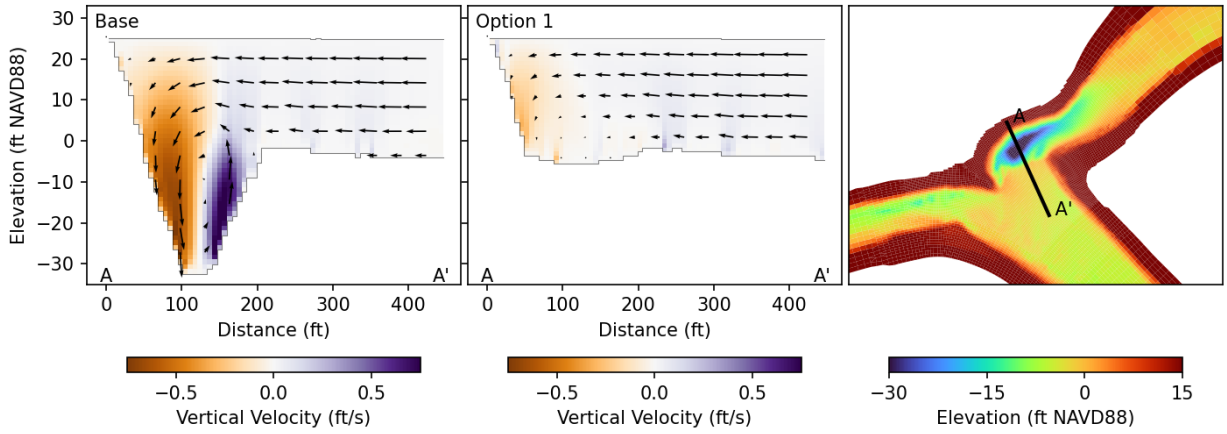

Figure 54 Distribution of vertical velocity across the scour hole.

Figure 55 compares bed shear stress between Base and Option 1 conditions. The filled region had substantial increases in bed stress, exceeding 20 Pa over much of the filled area. Model results showed the greatest increases in bed stress, more than 10 Pa, along the downstream end of the fill. Note that the model calibration showed that subsurface velocity maxima over the scour hole were generally underrepresented. Based on those results, bed stress for the Base conditions was likely underpredicted in the scour hole itself. While subsurface velocity maxima were likely in Option 1, we expect the effect to be substantially weaker than in the Base conditions due to a decrease in downwelling on the NW side of the scour hole.

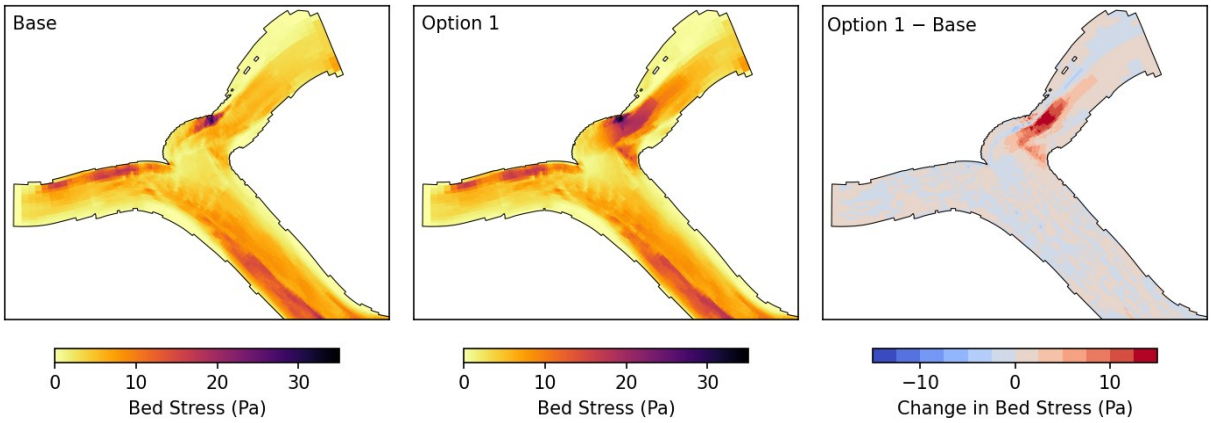

Figure 55 Bed stress at 100-year flood conditions for Base and Option 1 with D_{90}≈180mm fill.

The overall distribution of bed stress for Base and Option 1 conditions are shown in Figure 56. The distributions show that Option 1 had substantially more area with bed stress above 7 Pa than the Base conditions.

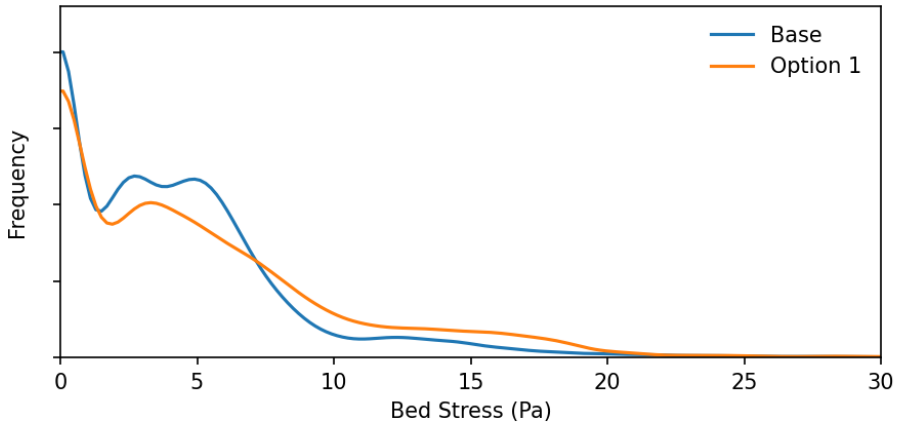

Figure 56 Distribution of bed stress during 100-year flood conditions. Distributions are extracted over the region shown in Figure 52.

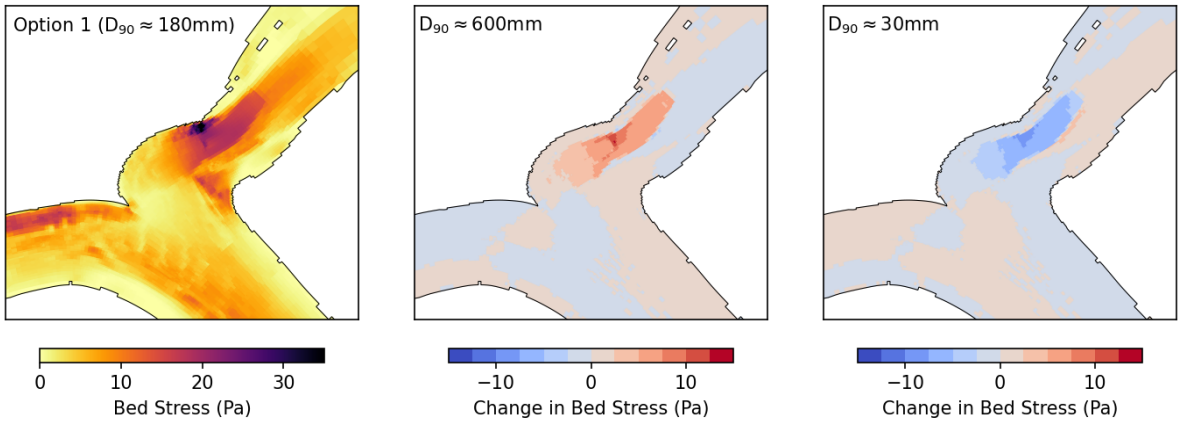

Figure 57 Modeled bed stress for Option 1 and change in bed stress relative to Base conditions for alternative D_{90} scenarios (≈600 mm and ≈30 mm).

Figure 57 shows three charts. Sensitivity of bed stress to roughness parameterization. (left) Bed stress with roughness approximating 180mm fill. (center, right) Change in bed stress with 600mm and 30mm diameter fill, respectively.

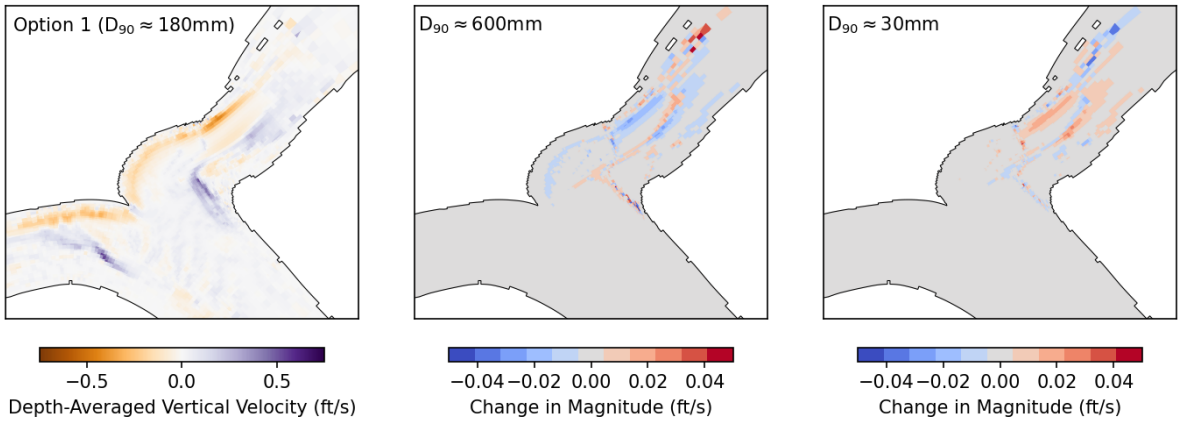

Figure 58 Depth-averaged vertical velocity for Option 1 and change in magnitude relative to Base conditions for alternative D_{90} scenarios (≈600 mm and ≈30 mm).

Figure 58 shows three charts. Sensitivity of depth-averaged vertical velocity to roughness parameterization. (left) Depth-averaged vertical velocity with roughness approximating 180mm fill. (center, right) Change in depth-averaged vertical velocity with 600mm and 30mm diameter fill, respectively.

DISCUSSION

The three-dimensional hydrodynamic model was used to simulate base conditions and the Option 1 alternative. There were three goals of the simulation: (i) test whether three-dimensional processes have a substantial effect on predicted flood stage relative to the two-dimensional model, (ii) demonstrate that filling in the scour hole reduces secondary and vertical circulation, and (iii) estimate the effect of filling in the scour hole on bed stress.

Water level comparisons between base conditions and option 1 at 100-year flood flows were largely consistent with results from the two-dimensional modeling. The two models predicted similar magnitudes of a local increase in water level immediately over the scour hole, and a reduction in water level downstream of the scour hole. The agreement between models supports the use of the two-dimensional model for water-level analysis at both large (Delta) and small (scour hole) scales. The three-dimensional model remains our tool of choice for analysis of secondary circulation, vertical velocity, and bed stress in the vicinity of the scour hole and the footprint of the alternatives.

As expected, the Option 1 simulation showed a strong decrease in both the horizontal component of secondary circulation and in vertical velocities, relative to base conditions. At the same time, bed stress over the scour hole increased substantially, exceeding 20 Pa over the filled region with a nominal roughness of 6mm. A key design parameter for Option 1 is the selection of fill material, which, in turn, will affect the frictional characteristics of the bed. A sensitivity analysis, altering the roughness of the simulated scour hole fill, demonstrated that the secondary and vertical velocities were not strongly affected by roughness while bed stress was highly sensitive to roughness.

REFERENCES

Bever AJ, MacWilliams ML. 2016. Factors influencing the calculation of periodic secondary circulation in a tidal river—Numerical modelling of the lower Sacramento River, USA: Hydrological Processes, v. 30, no. 7, p. 995–1016, https://doi.org/10.1002/hyp.10690.

Canuto VM, Howard A, Cheng Y, Dubovikov MS. 2001. Ocean turbulence i: one-point closure model - momentum and heat vertical diffusivities, Journal of Physical Oceanography, 31:1413.1426.

Federal Emergency Management Agency (FEMA). 2009. Flood Insurance Study, San Joaquin County, California, Volumes 1 & 4. Flood Insurance Study Number 06077CV001A. October 16, 2009.

Fringer OB, Gerritsen M, Street RL. 2006An unstructured-grid, finite-volume, nonhydrostatic, parallel coastal ocean simulator. Ocean Model. 14: 139–173. https://doi.org/10.1016/j.ocemod.2006.03.006

Gross ES, Holleman RC, Thomas MJ, Fangue NA, Rypel AL. 2021. Development and Evaluation of a Chinook Salmon Smolt Swimming Behavior Model, 13: 2904. https://doi.org/10.3390/w13202904

Holleman RC, Gross ES, Thomas MJ, Rypel AL, Fangue NA. 2022. Swimming behavior of emigrating Chinook Salmon smolts. PLoS ONE 17(3): e0263972. https://doi.org/10.1371/journal.pone.0263972

Rodi W. 1987. Examples of calculation methods for flow and mixing in stratified flows. J Geophys Res 92:5305–5328.

Rozovski IL. 1957. Flow of water in bends of open channels: Academy of Sciences of the Ukrainian SSR, 233 p.

Umlauf L, Burchard H. 2003. A generic length-scale equation for geophysical turbulence models. J Mar Res 61:235–265.

Willmott CJ. 1981. On the validation of models. Phys. Geogr. [accessed 2019 Sep 14];2(2):184–194. https://doi.org/10.1080/02723646.1981.10642213